

**Generation of Horizontally Curved Driving Lines for Autonomous  
Vehicles Using Mobile Laser Scanning Data**

by

Lingfei Ma

A thesis

presented to the University of Waterloo

in fulfillment of the

thesis requirement for the degree of

Master of Science

in

Geography

Waterloo, Ontario, Canada, 2017

© Lingfei Ma 2017

## **Author's Declaration**

I hereby declare that I am the sole author of this thesis. This is a true copy of the thesis, including any required final revisions, as accepted by my examiners.

I understand that my thesis may be made electronically available to the public.

## Abstract

The development of autonomous vehicle desiderates tremendous advances in three-dimensional (3D) high-definition roadmaps. These roadmaps are capable of providing 3D positioning information with 10-to-20 cm accuracy. With the assistance of 3D high-definition roadmaps, the intractable autonomous driving problem is transformed into a solvable localization issue. The Mobile Laser Scanning (MLS) systems can collect accurate, high-density 3D point clouds in road environments for generating 3D high-definition roadmaps. However, few studies have been concentrated on the driving line generation from 3D MLS point clouds for highly autonomous driving, particularly for accident-prone horizontal curves with the problems of ambiguous traffic situations and unclear visual clues.

This thesis attempts to develop an effective method for semi-automated generation of horizontally curved driving lines using MLS data. The framework of research methodology proposed in this thesis consists of three steps, including road surface extraction, road marking extraction, and driving line generation. Firstly, the points covering road surface are extracted using curb-based road surface extraction algorithms depending on both the elevation and slope differences. Then, road markings are identified and extracted according to a sequence of algorithms consisting of geo-referenced intensity image generation, multi-threshold road marking extraction, and statistical outlier removal. Finally, the conditional Euclidean clustering algorithm is employed followed by the nonlinear least-squares curve-fitting algorithm for generating horizontally curved driving lines.

A total of six test datasets obtained in Xiamen, China by a RIEGL VMX-450 system were used to evaluate the performance and efficiency of the proposed methodology. The

experimental results demonstrate that the proposed road marking extraction algorithms can achieve 90.89% in recall, 93.04% in precision and 91.95% in F1-score, respectively. Moreover, the unmanned aerial vehicle (UAV) imagery with 4 cm was used for validation of the proposed driving line generation algorithms. The validation results demonstrate that the horizontally curved driving lines can be effectively generated within 15 cm-level localization accuracy using MLS point clouds. Finally, a comparative study was conducted both visually and quantitatively to indicate the accuracy and reliability of the generated driving lines.

## Acknowledgements

First and foremost, I would like to express the most sincere gratitude to my supervisor, Professor Dr. Jonathan Li, who provides me this valuable opportunity to join the Mobile Sensing and Geodata Analytics Lab and offers me not only professional research knowledge but also life guidance during my master's program. Without his positive comments, insightful suggestions, continuous encouragement and patient guidance, it would be impossible for me to complete the program. It has been a great honour to work with him for the past two years.

I would like to express my gratitude and appreciation to my Thesis Examining Committee members, Prof. Dr. Michael Chapman, Prof. Dr. Ellsworth LeDrew, and Prof. Dr. Ruisheng Wang; thank you for reviewing my thesis and providing me the constructive comments and valuable suggestions on my study.

I would like to thank Angelina Zhou, Bella Wang, Haocheng Zhang, Weikai Tan, Zilong Zhong, He Zhao, and Han Jiang, all the members in Mobile Sensing and Geodata Analytics Lab, for their great academic assistances and contributions to my thesis. Special thanks go to the Fujian Key Laboratory of Sensing and Computing for Smart Cities in Xiamen University, for providing me with RIEGLVMX-450 point clouds and the UAV imagery used in this study.

I also would like to express deepest gratitude to my dear parents in China, who provide continuous financial support and emotional encouragement to keep my positive attitude during my studies. Thanks to all my friends here and in China, who accomplish me in the past two years and offer me with their encouragement, help and understanding.

*Lingfei Ma*

August 20, 2017

## Table of Contents

Author’s Declaration.....	ii
Abstract.....	iii
Acknowledgements.....	v
Table of Contents.....	vi
List of Figures.....	ix
List of Tables.....	xi
List of Abbreviations.....	xii
Chapter 1 Introduction.....	1
1.1 Motivation.....	1
1.2 Objectives of the Thesis.....	8
1.3 Structure of the Thesis.....	8
Chapter 2 Background and Related Studies.....	10
2.1 Research Background.....	10
2.1.1 Introduction to Autonomous Vehicles.....	10
2.1.2 3D High-definition Roadmaps.....	12
2.1.3 Horizontal Curve.....	14
2.2 Principles of MLS System Operations.....	16
2.2.1 Introduction of MLS System.....	16
2.2.2 Direct Geo-referencing of MLS Data.....	17
2.3 Road Surface Extraction from MLS data.....	19
2.3.1 Extracting Road Surface by Road Structure.....	19
2.3.2 Extracting Road Surface by MLS Data Characteristics and Road Properties.....	21
2.3.3 Extracting Road Surface Based on 2D or 3D Geometric Features.....	21
2.4 Road Marking Extraction from MLS data.....	27
2.5 Road Horizontal Parameter Estimation from MLS data.....	30
2.6 Chapter Summary.....	32
Chapter 3 Methodology for Generating Driving Lines.....	34
3.1 Data Collection.....	34
3.2 Workflow of the Proposed Methodology.....	38
3.3 Road Surface Extraction.....	40

3.3.1 Trajectory-based Point Clouds Profiling .....	42
3.3.2 Pseudo Scan-line Generation .....	44
3.3.3 Road Curb Detection .....	45
3.3.4 Road Edge Fitting .....	48
3.4 Road Marking Extraction .....	49
3.4.1 Geo-referenced Feature Image Generation.....	51
3.4.2 Determination of Multi-thresholds .....	52
3.4.3 Multi-threshold Extraction .....	54
3.4.4 Noise Removal .....	54
3.5 Generation of Horizontally Curved Driving Lines .....	56
3.5.1 Conditional Euclidean Clustering.....	58
3.5.2 Nonlinear Least-Squares Curve Fitting .....	60
3.5.3 Driving Line Generation.....	65
3.6 Validation .....	66
3.6.1 Accuracy Assessment of Road Marking Extraction.....	66
3.6.2 Orthoimage Generation .....	67
3.6.3 Evaluation.....	69
3.7 Chapter Summary.....	69
Chapter 4 Results and Discussion.....	70
4.1 Test Datasets .....	70
4.1.1 Test MLS Datasets.....	70
4.1.2 Reference Data .....	75
4.2 Experimental Results.....	75
4.2.1 Road Surface Extraction.....	75
4.2.2 Geo-referenced Intensity Image Generation.....	80
4.2.3 Road Marking Extraction .....	82
4.2.4 Noise Removal .....	84
4.2.5 Road Marking Clustering .....	86
4.2.6 Curve Fitting.....	88
4.2.7 Driving Line Generation.....	92
4.2.8 Overall Performance Assessment.....	97

4.3 Validation Results .....	98
4.3.1 Accuracy Assessment of Road Marking Extraction.....	98
4.3.2 Comparative Study of Road Marking Extraction .....	100
4.3.3 Accuracy Assessment of Driving Line Generation .....	104
4.4 Chapter Summary.....	106
Chapter 5 Conclusions and Recommendations.....	107
5.1 Conclusions .....	107
5.2 Contributions .....	109
5.3 Limitations and Recommendations for Further Studies.....	110
References.....	112



## List of Figures

Figure 1.1 Lines in high-definition road maps defined in this thesis.....	6
Figure 2.1 The HD Live Map designed by HERE.....	13
Figure 2.2 Four types of the horizontal curves.....	15
Figure 2.3 Principles of direct geo-referencing.....	18
Figure 3.1 System configuration of a RIEGL VMX-450 system.....	35
Figure 3.2 The surveyed corridors in Xiamen and horizontal curves in MLS data.....	38
Figure 3.3 Workflow of the proposed methodology.....	38
Figure 3.4 Workflow of the proposed road surface extraction method.....	41
Figure 3.5 Illustration of trajectory-based point clouds profiling.....	43
Figure 3.6 Profiling process on the MLS point clouds.....	43
Figure 3.7 The sliced profile images.....	43
Figure 3.8 Curb identification in a profile image.....	44
Figure 3.9 The generated principal points in a profile image.....	45
Figure 3.10 A pseudo scan-line of a profile image.....	46
Figure 3.11 An example of extracted road surface.....	49
Figure 3.12 Workflow of the proposed road marking extraction method.....	50
Figure 3.13 An illustration of the determination of gray values.....	51
Figure 3.14 Determination of multi-thresholds.....	52
Figure 3.15 The principle of the SOR filter.....	55
Figure 3.16 Extracted road markings using the proposed method.....	56
Figure 3.17 Refined road markings after noise removal.....	56
Figure 3.18 Workflow of the proposed driving line generation method.....	57
Figure 3.19 The conditional Euclidean clustering method.....	58

Figure 3.20 Results of the conditional Euclidean clustering.....	59
Figure 3.21 A curve generated using the nonlinear least-squares curve fitting algorithm.....	62
Figure 3.22 The elements of a circular horizontal curve.....	64
Figure 3.23 Directly geo-referenced 3D point clouds in a local mapping frame.....	67
Figure 4.1 Six test datasets used in this thesis.....	72
Figure 4.2 Point density distributions of six test datasets.....	74
Figure 4.3 Reference data used in this study.....	75
Figure 4.4 Road surface extraction results obtained using six test datasets.....	78
Figure 4.5 Point density distributions of the extracted road surfaces.....	80
Figure 4.6 Geo-referenced intensity image generated by IDW interpolation.....	82
Figure 4.7 Four types of road markings and their extraction results.....	83
Figure 4.8 Results of noise-removed road markings.....	86
Figure 4.9 Road marking clustering results.....	88
Figure 4.10 Mean curvature distributions of road marking results.....	90
Figure 4.11 Mean curvature distributions of curve-fitting results.....	92
Figure 4.12 The generated circular curve of a driving line.....	93
Figure 4.13 Driving line generation results.....	95
Figure 4.14 Extracted road marking after noise removal from each of the six test datasets.....	98
Figure 4.15 Extracted road markings and the reference data.....	99
Figure 4.16 Road marking extraction results using Dataset I.....	101
Figure 4.17 Road marking extraction results using Dataset IV.....	102
Figure 4.18 Road marking extraction results using Dataset V.....	103
Figure 4.19 Driving line generation results within reference buffers.....	105

## List of Tables

Table 2.1 Specifications of two commercial laser scanners.....	11
Table 2.2 Parameters used in the direct geo-referencing.....	19
Table 2.3 Several road surface extraction methods.....	25
Table 2.4 Comparison of road marking extraction methods.....	30
Table 2.5 Summary of horizontal parameters extraction methods using MLS data.....	32
Table 3.1 Specifications of the RIEGL VMX-450 system.....	35
Table 3.2 Horizontal circular curve elements.....	64
Table 3.3 Confusion matrix of binary classification.....	66
Table 4.1 Parameters for road surface extraction algorithms.....	76
Table 4.2 The number of MLS points after road surface extraction.....	78
Table 4.3 Table 4.3 Resolution of Geo-referenced intensity image and its data size.....	81
Table 4.4 Table 4.4 Geo-referenced intensity images with different resolutions.....	81
Table 4.5 Parameters for road marking extraction algorithms.....	82
Table 4.6 Road marking types in geo-referenced intensity images.....	83
Table 4.7 Parameters for the conditional Euclidean clustering method. ....	87
Table 4.8 Parameters for the nonlinear least-squares curve-fitting algorithm.....	88
Table 4.9 Parameters used in driving line generation algorithms.....	93
Table 4.10 Elements of a generated driving line.....	96
Table 4.11 Code for Design of Urban Road Engineering, China.....	97
Table 4.12 Computation efficiency of all proposed algorithms.....	97
Table 4.13 Accuracy assessment of road marking extraction.....	99
Table 4.14 Comparison of the three methods in quantitative evaluation.....	101
Table 4.15 Accuracy assessment of driving line generation.....	104

## **List of Abbreviations**

2D	Two-dimensional
3D	Three-dimensional
ALS	Airborne Laser Scanning
DMI	Distance Measurement Indicator
GAMS	GPS Azimuth Measurement System
GCP	Ground Control Point
GIS	Geographic Information System
GNSS	Global Navigation Satellite System
GRF	Geo-referenced Feature
GPS	Global Positioning System
ICT	Information and Communication Technology
IDW	Inverse Distance Weighted
IMU	Inertial Measurement Unit
LiDAR	Light Detection and Ranging
MLS	Mobile Laser Scanning
MTO	Ministry of Transportation Ontario
MSTV	Multi-scale Tensor Voting
NHTSA	National Highway Traffic Safety Administration
PCA	Principal Component Analysis
PCL	Point Cloud Library
POS	Position and Orientation System
RANSAC	RANdom Sample Consensus
SOR	Statistical Outlier Removal
TLS	Terrestrial Laser Scanning
UAV	Unmanned Aerial Vehicles
XMU	Xiamen University

# Chapter 1 Introduction

## 1.1 Motivation

In recent years, the design and development of autonomous vehicles with intelligent and coordinated action capabilities to achieve self-driving without human interactions, has been the object of considerable interest in the artificial intelligence and automotive engineering communities (Lozano-Perez, 2012). An autonomous vehicle has the capability to determine the best navigation routes, drive itself on the most challenging road networks, and avoid collisions with fixed or moving road users (e.g., pedestrians, cyclists and cars) without direct human operations (Fagnan and Kockelman, 2015). Consequently, many worldwide prominent automotive manufacturers (e.g., General Motors, BMW, Mercedes-Benz, Audi, Fiat Chrysler, Toyota, and Ford) and information and communication technology (ICT) companies (e.g., Google, Uber, Apple, Tesla, Baidu and Nvidia), are investing heavily, adjusting their development strategies, and indicating their ambitions to participate in the emerging market of self-driving vehicles (Sisson, 2017).

According to the new policy on automated vehicle development released in May 2013 by the U.S. Department of Transportation's National Highway Traffic Safety Administration (NHTSA), five levels are defined for vehicle automation: no-automation (Level 0), function-specific automation (Level 1), combined function automation (Level 2), limited self-driving automation (Level 3), and full self-driving automation (Level 4) (NHTSA, 2013). These five levels are detailed as follows:

Level 0 - Function-specific automation. Specific control functions are automated, including adaptive cruise control, automated parallel parking and lane keeping. Drivers are

completely responsible for driving safety and overall control (i.e., the drivers are fully engaged for steering and braking).

Level 1 - Combined function automation. Multiple and integrated functions are automated, such as adaptive cruise control with the assistance of lane centering. The driver has responsibility to monitor the roadway and safe operation. However, drivers are disengaged from vehicle's operation under specific conditions.

Level 2 - Limited self-driving automation. Drivers are able to cede all safety-critical functions in certain conditions, and are not expected to constantly monitor the roadway while driving.

Level 3 - Self-driving under specified conditions. Vehicles can achieve highly autonomous driving functions under specified conditions.

Level 4 - Full self-driving automation. Vehicles are capable of performing highly autonomous driving on all road networks, speed ranges and environmental conditions without any direct human operations.

Typically, a fully autonomous vehicle (Level 4) are equipped with several data acquisition devices that work in combination with each other to achieve highly autonomous driving (Guizzo, 2011). Radar sensors mounted on the front and rear bumpers enable the car monitor the positioning information of surrounding vehicles. Video cameras are capable of detecting traffic lights, roadside signs, and keeping track of vehicles nearby, while also detecting pedestrians and other obstacles. Moreover, LiDAR sensors mounted on the roof of the vehicle are able to detect road edges and identify road markings by emitting continuous laser pulses and receiving the reflected signals. Finally, a central computing system analyzes all of the data

obtained from the multiple sensors to manipulate the steering, acceleration and braking. However, these multiple on-board sensors cannot provide effective and safe navigation services for autonomous vehicles under certain traffic conditions, including the limited sight distance of sensors and ambiguous visual clues (Rupp and King, 2010). Additionally, autonomous vehicles cannot achieve highly autonomous driving function in rural road environments without road markings or the curbs of the roadways. Therefore, autonomous vehicles depend on dynamic three-dimensional (3D) high-definition roadmaps to support precise vehicle positioning and route navigating services for all road environments (Dokic et al., 2015).

Compared to the conventional road maps, the 3D high-definition roadmaps are developed for more precise traffic navigation with high accuracy and detailed road network information (e.g., lanes, road edges, centrelines, and restrictions). According to the final report of the Enhanced Digital Mapping Project submitted to the United States Department of Transportation (USDOT) in 2004, the lane-level accuracy performance of 3D high-definition roadmaps can reach 30 cm (USDOT, 2004). Furthermore, 3D high-definition roadmaps can provide autonomous vehicles with an extended monitoring range, allowing cars to anticipate turns and intersections far beyond the reach of onboard sensors. With the assistance of conventional 2D navigation maps, it is very challenging for onboard sensors to identify the traffic sign early if this traffic sign is blocked by obstacles or the car is moving fast on highways, which results in potential traffic risks. Accordingly, a 3D high-definition roadmap is indispensable to not only provide highly precise sub-lane level information of road networks (e.g., accidents, roadside signs, lane marking types, slope, curvature, and road speed limit information), but also solve the problems of detection and reaction early to events happening on the traffic lanes (Bauer et al. 2016). Based on detailed 3D high-definition roadmaps, autonomous vehicles have the capability

to drive in accordance with the restrictions of road specifications and the behaviours of other traffic participants, particularly for complex urban road networks and highway environments (Seif and Hu, 2016).

In order to capture real-time road information and generate 3D high-definition roadmaps for autonomous vehicles, Mobile Laser Scanning (MLS) technique is applied to acquire high-resolution topographic data and construct 3D road models with highly sensitive information about road infrastructures (Marshall and Stutz, 2011). Meanwhile, Airborne Laser Scanning (ALS) and Terrestrial Laser Scanning (TLS) techniques are also capable of collecting high-density and geo-referenced point clouds with highly accurate positioning information. However, ALS cannot penetrate fog, dust, clouds and dense vegetation. The laser beams will not detect the ground below dense conifers and multistory buildings. Terrestrial laser scanners are normally mounted on a tripod, which provides a maximum scanning range of 250–1000 m with a measurement accuracy of 5-10 mm by using time-of-flight scanning pattern (Vosselman and Mass, 2010). Nevertheless, due to its low flexibility and mobility characteristics, TLS technique is not widely used in the application of 3D high-definition roadmaps. Compared to 3D highly dense point-based techniques, aerial and satellite image-based methods are also applied to generate high-definition roadmaps. High-resolution optical imagery has capability to provide rich textural, spectral, and semantic information for different ground features. Since the limitations of passive remote sensing technique, the feature extraction and classification accuracy can be affected by a variety of factors, including inconstant luminance, perspective effects of high-resolution imagery, weather conditions, shadows and operation time of the day. Therefore, high-resolution imagery with high-quality geographic data is normally used as a basic map layer for 3D high-definition roadmaps (HERE, 2016).



Accordingly, a MLS system is the vehicle-based mapping systems that integrate various navigation and data acquisition devices, including laser scanners, optical cameras, a Global Navigation Satellite System (GNSS), an Inertial Measurement Unit (IMU), a Distance Measurement Indicator (DMI), and an integrated computing system (Guan, 2013). It produces 3D MLS point clouds from the surrounding objects by utilizing profiling scanning technique (Haala et al., 2008). Moreover, MLS systems are capable of providing highly accurate, geo-referenced data with higher time-efficiency and better cost-saving in comparison to traditional surveying methods, such as human fieldwork and satellite imagery (Puente et al., 2013). Additionally, considering their prominent mobility and flexibility characteristics, MLS systems are more appropriate for developing 3D high-definition roadmaps, particularly in both urban roadways and highway environments with high-density traffic flows and complicated traffic situations (Toth, 2009). Currently, based on MLS technologies, a consortium of 15 Japanese automakers and manufactures (e.g., Toyota, Honda and Mitsubishi Electric) have cooperated together to develop detailed 3D high-definition roadmaps for obtaining additional road information (e.g., lane divisions, lane curvatures and widths, lane closures and usage rules), which aims to decrease the number of casualties and improve the safety of autonomous driving.

Therefore, depending on 3D high-definition roadmaps established by using MLS data to generate effective and reliable driving lines, autonomous vehicles can identify and leapfrog slow-moving traffic, negotiate interchanges, determine the correct lane to drive through horizontal curves and make predictive decisions in case of emergency (Schwarz, 2010). The driving lines that typically locate at central positions between two line-shaped road markings (e.g., centrelines, edge lines and lane lines), are considered as driving paths or navigation routes for autonomous vehicles in various road environments. Determining safe and reliable driving

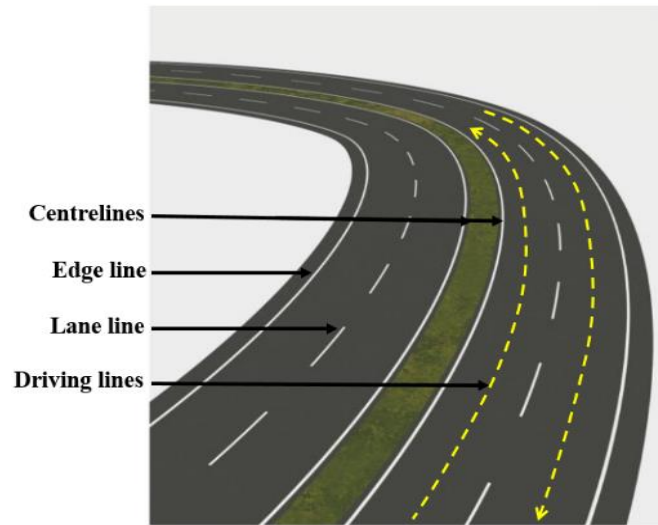


Figure 1.1 Lines in high-definition roadmaps defined in this thesis.

lines in advance can greatly overcome the limitations of the vehicle's on-board sensors, extend the monitoring range for autonomous vehicles, and enables these vehicles to react early in case of traffic emergencies. Figure 1.1 presents several types of line-shaped curved road markings (e.g., white solid lines around the green belt indicate centrelines, white solid lines on the both sides of the road represent edge lines, white dashed lines are lane lines and yellow dashed lines show driving lines in this thesis). Additionally, the probability of traffic accidents would increase greatly for autonomous vehicles in complex traffic conditions including turns, curves, intersections, roundabouts and highways (Peden, 2004; Urmson, 2008). As an important element of roadway design and construction, horizontal curves have a considerable impact on traffic safety and efficiency due to the gradual change in direction of curves and limited sight distance for both drivers and onboard sensors (Khan et al., 2012). In the U.S., the average collision rate at horizontal curves is about three times that of other highway segments (Torbic et al., 2004). Thus, eliminating safety hazards at horizontal curves is an inevitable process in the development of autonomous vehicles. Accordingly, considering the turning speed limitation, driving lane

departure and vehicle-handling capability issues, one of the most challenging tasks for autonomous driving is to enable autonomous vehicles to design the best effective and safest driving lines at horizontal curves without human operations (Choi et al., 2008).

However, processing of a massive amount of 3D point clouds is regarded as a grand challenge. For instance, a RIEGL VMX-450 system is capable of collecting point clouds up to a total of 120 GB within one hour at a normal driving speed (RIEGL, 2017). Consequently, it requires not only a high-performance computation system but also high-efficiency processing algorithms for road information extraction. Therefore, developing an effective and reliable method to generate horizontally curved driving lines from high-density MLS point clouds has become a large market demand in order to support the development of 3D high-definition roadmaps for fully self-driving automation (Level 4).

This thesis will focus on elaborating reasonable rationales and proposing semi-automatic algorithms to generate reliable and effective driving lines using MLS point clouds at horizontally curved road sections. Based on geomatics, computer vision, mobile mapping technologies and road design regulations, the proposed methodology in this thesis is to enable a prospective application of MLS data for the development of 3D high-definition roadmaps and autonomous vehicles. Additionally, the methodology proposed in this thesis is capable to minimize manual intervention for an advanced processing of large-volume MLS point clouds. This thesis research will improve route-planning strategies for autonomous driving, especially for the accident-prone horizontally curved road scenarios. Furthermore, this study demonstrates the huge market potentials and opportunities of MLS data in mobile mapping, surveying, cartography and automotive industries.

## **1.2 Objectives of the Thesis**

The purpose of this thesis is to develop semi-automated algorithms for the detection and extraction of road markings particularly for lane lines, centrelines and edge lines at the horizontally curved road sections. Furthermore, to generate horizontally curved driving lines based on high-density MLS point clouds can support the development of autonomous vehicles.

The specific objectives of this thesis are described as follows:

- 1) Presenting semi-automatic algorithms for the detection and extraction of road markings from large-volume MLS data, particularly for horizontally curved road sections;
- 2) Developing semi-automatic algorithms for the generation of horizontally curved driving lines by taking road design regulations and curve-fitting functions of curved road markings into consideration;
- 3) Conducting an accuracy assessment to quantitatively evaluate the extracted road markings, and implementing a comparative study with existing methods to verify the performance of the proposed road marking extraction algorithms; and
- 4) Performing an accuracy assessment to validate the accuracy and reliability of the generated driving lines both visually and quantitatively.

## **1.3 Structure of the Thesis**

This thesis contains the following five chapters.

Chapter 1 describes the motivation and background of this thesis, followed by presenting the research objectives and the structure of the thesis.

Chapter 2 presents a thorough review of the state-of-the-art literature. At the beginning, the basic information about autonomous vehicles and MLS technique is briefly introduced. Next, the requirements for 3D high-definition roadmaps are afterward described. Moreover, the current advanced methods for the extraction of road surface and road markings using MLS data are systematically and comprehensively reviewed. Finally, this chapter ends with introducing previous related studies concentrating on road parameters extraction at horizontal curves from MLS point clouds.

Chapter 3 details the methodology including the proposed algorithms. Moreover, methods for accuracy assessment using the unmanned aerial vehicle (UAV) imagery and comparative study with previous methods are introduced.

Chapter 4 presents the test datasets and reference data by first. Then, this chapter provides the experimental results obtained by six test datasets using the proposed methods. Furthermore, the performance assessment results and comparison results are also presented.

Chapter 5 draws a conclusion with findings, summarizes the contributions and discusses limitations of this thesis. Moreover, the research challenges and suggestions for future studies are also discussed.

## **Chapter 2 Background and Related Studies**

This chapter contains a systematic and comprehensive literature review of backgrounds and studies related to this thesis topic. Firstly, an introduction to autonomous vehicles and their requirements for 3D high-definition roadmaps are presented in Section 2.1. Secondly, the principles of MLS systems are detailed in Section 2.2. Then, the state-of-the-art methods for road surface detection using MLS data are reviewed in Section 2.3 followed by road marking extraction in Section 2.4, and road horizontal parameters extraction in Section 2.5. Through a review of previous related techniques and methods for extracting road information, this chapter elaborately provides a theoretical background in understanding principles of MLS technology, applications of 3D high-definition roadmaps and methodologies used in this study.

### **2.1 Research Background**

#### **2.1.1 Introduction to Autonomous Vehicles**

An autonomous vehicle is a robotic vehicle, which has the capability to sense its surrounding road environment, determine the best routes, drive itself on the most challenging road networks, navigate numerous types of road environment and avoid collisions with fixed or moving objects (e.g., pedestrians, cyclists and vehicles) without direct human operations (Guizzo, 2011). Recent advances in sensing and navigation devices, computational capabilities, and 3D high-definition roadmaps have the potential to dramatically facilitate the development of autonomous vehicles (Casner et al., 2016). Firstly, radar sensors mounted on the vehicle are capable of monitoring the positions of other surrounding road users, while the Light Detection and Ranging (LiDAR) sensors can be applied to detect the road edges and identify road markings by emitting continuous laser pulses and recording corresponding reflected signals. Video cameras have the ability to collect detailed road information and analyze image data of vehicles,

pedestrians and other obstacles. Additionally, according to the Google’s Driverless Car Report in 2016, the vehicle-mounted LiDAR sensors detect a range of 100 m with rotational ability of 360° around the car and establish a real-time dynamic 3D roadmap of the current road environments. Finally, based on high-performance computation and storage techniques, an integrated computer system is employed to record, manage, and analyze multiple data sources from the various sensors for manipulations of steering, acceleration and braking (Anderson et al., 2014). However, autonomous vehicles not only need onboard sensors to sense their surroundings, but also need precise 3D high-definition roadmaps to better understand the traffic situations far beyond the reach of sensors. Thus, autonomous vehicles are dependent on advanced 3D high-definition roadmaps to support precise localization and navigation services (Seif and Hu, 2016).

Table 2.1 Specifications of two commercial laser scanners.

Company		RIEGL	Velodyne
Laser scanner component	Laser scanner	RIEGL VQ-450	HDL-64E
	Laser wavelength	near infrared	near infrared
	Maximum range	800 m	120 m
	Minimum range	1.5 m	1.5 m
	Measurement precision	5 mm ( $1\sigma$ )	-
	Absolute accuracy	8 mm	2 cm
	Scan frequency	400 lines/sec	-
	Angle measurement resolution	0.001°	0.09°
	Scanner field of view	360°	360°

Table 2.1 describes detailed specifications of two commercial laser scanners, which are RIEGL VQ-450 and Velodyne HDL-64E integrated in RIEGL VMX-450 system and Google’s Driverless cars, respectively (Glennie and Lichti, 2010; RIEGL, 2017). It is identified that the

laser scanners integrated in MLS system are capable of providing higher measurement accuracy and further measurement range than autonomous vehicles' on-board laser scanners. Consequently, 3D high-definition roadmaps established by using laser scanners in MLS system can provide highly effective route navigation services for autonomous vehicles.

### **2.1.2 3D High-definition Roadmaps**

A 3D high-definition roadmap provides a highly accurate and realistic representation of the current road networks, which is capable of updating in real-time and recording traffic changes such as accidents, lane closure, traffic congestion, and updated speed limitation at cm-level accuracy (Miller, 2014). The 3D high-definition roadmap is a significant element of highly autonomous driving technology, assisting autonomous vehicles precisely localize themselves on the road and providing autonomous vehicles with an extended monitoring range to anticipate turns and intersections far beyond the view of sensors (Guizzo, 2011). Therefore, compared to the conventional road navigation maps, 3D high-definition roadmaps are designed for highly precise route navigation services with high accuracy and detailed traffic network information (e.g., lanes, lane markings, roadside objects, and restrictions).

With regard to a great market demand, digital map suppliers such as HERE (a mapping company owned by BMW, Daimler, and the Volkswagen Group) and TomTom are dedicated to the research and development of high-definition roadmaps to provide advanced lane guidance and high-efficiency route navigation services for autonomous driving. As shown in Figure 2.1, the HD Live Map established by HERE consists of dynamic content layers to provide detailed



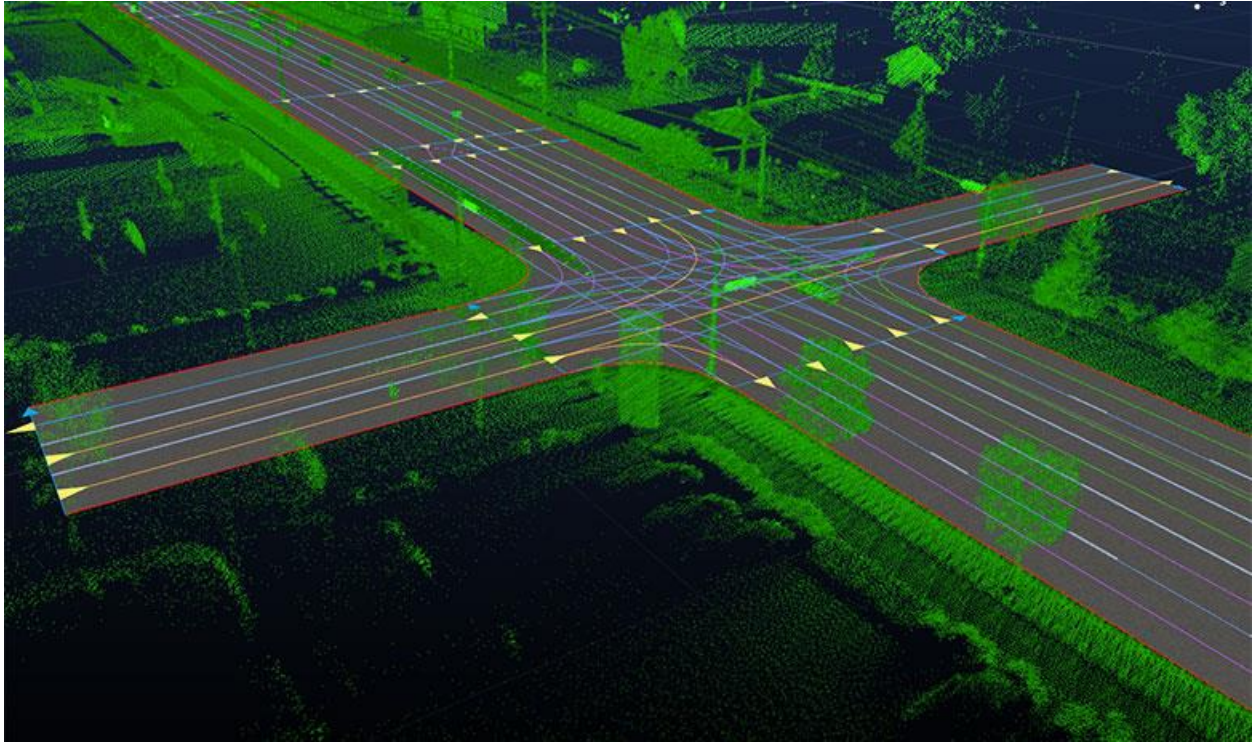


Figure 2.1 The HD Live Map designed by HERE.

and real-time road information, including detailed lane level information (e.g., color lines indicate different line-shaped road markings and generated driving lines, while various arrows represent the driving direction for autonomous vehicles), dynamic road networks and health situation changes, roadside infrastructures (e.g., traffic signs), and speed profile data (HERE 360, 2016). Moreover, the HD Live Map is one of the most advanced layer-based cloud services, in combination with timely accident reports, dynamic traffic flow data, and speed profile data, this HD Live Map is capable of supporting automobile companies in their strategies of developing autonomous driving and mobility. For instance, the map layer assembled in HD Live Map is a precise sub-lane level representation of the road network. Subsequently, the activity layer records dynamic traffic events including traffic conditions and collision warnings beyond the sight distance of onboard sensors. Additionally, the analytics layer collects and analyzes long-term

location-based drivers' behaviour data to navigate a highly automated vehicle and provide customized convenience services for the drivers. Currently, HERE is using satellite and aerial images as a foundation for high-definition roadmaps. Moreover, employing MLS technology to capture complex road environments in 3D world is an effective method to obtain high-resolution information with accurate and precise geo-referenced data (Jakubiec and Mullinix, 2013). Meanwhile, TomTom depends on "Depth Maps" by using LiDAR sensors, and rebuilds a 3D view of the road networks around a moving car in real time particularly for dynamic and uncertain road environments and operating conditions.

### **2.1.3 Horizontal Curve**

Horizontal curves are significant and necessary elements in the geometric design of roadways and highways since these curves provide gradual change in direction and additional centripetal forces on vehicles (Khan et al., 2012). Additionally, horizontal curves can be classified into four fundamental categories: simple circular curves, compound curves, reverse curves, and spiral curves (McCormac et al., 2012). As shown in Figure 2.2 (a), a simple circular curve is a segment of a circle that is bounded by two tangents. The radius determines the sharpness and flatness of the circular curve. The compound curve consists of multiple consecutive simple curves and inner tangent segments (see Figure 2.2 (b)). The third category of horizontal curve is the reverse curve, which is composed of two simple circular curves curving in opposite direction (see Figure 2.2 (c)). As illustrated in Figure 2.4(d), the spiral curve is a horizontal curve that has a changing radius. It is identified that majority of curved road sections are designed as simple circular curves in order to ensure traffic efficiency and reduce road hazards, this thesis mainly focuses on developing effective driving lines for autonomous vehicles at horizontally circular curved road segments.

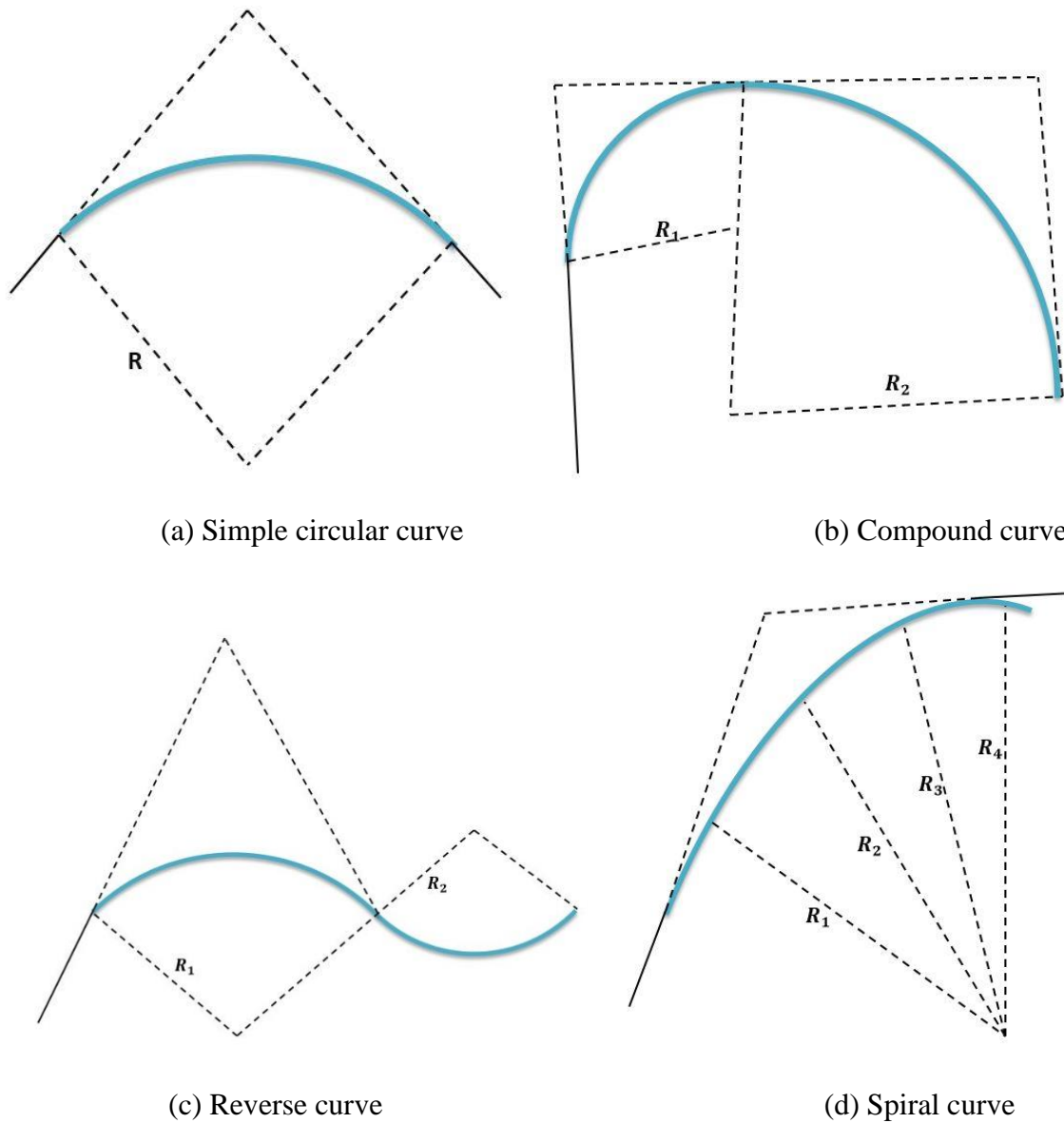


Figure 2.2 Four types of the horizontal curves.

Horizontally curved road segments are highly related to traffic accidents for all road users. Traffic collisions can be caused due to failures of driver attention and misperception of speed and curvature associated with horizontal curves (Charlton, 2007). Accordingly, McDonald (2004) indicated that the accident frequency could increase by 34% for per sharp curve per km. According to the report of A Guide for Reducing Collisions on Horizontal Curves, it indicates

that over 25% of traffic fatalities are killed in the road accidents at horizontal curves annually in the U.S. (Torbic et al., 2004). Additionally, based on the Preliminary 2016 ORSAR Selected Statistics submitted to the MTO, it reports that about 11.9% fatal and injury collisions occurred in Ontario are related to horizontal curves (ORSAR, 2016). Thus, in order to reduce the rate of traffic accidents, autonomous vehicles should have the capability to design the most efficient and reliable driving lines at horizontally curved road sections. Accordingly, 3D high-definition roadmaps that established by using highly dense MLS point clouds can provide autonomous vehicles with an extended sensing range to help such vehicles solve the problems of detection and reaction early (Dokic et al., 2015; Boudette, 2017). Therefore, in order to develop highly accurate 3D high-definition roadmaps especially for horizontally circular curved road sections, the following sections systematically and comprehensively review relevant methods including road surface extraction, road marking extraction and road horizontal parameters extraction using MLS data.

## **2.2 Principles of MLS System Operations**

### **2.2.1 Introduction of MLS System**

In general terms an MLS system is based upon laser scanning sensors, which collect 3D point clouds using profiling scanning technique and then detect laser pulses reflected from the target surfaces. According to the velocity of light, the travel time of laser pulses can be used to determine the precise range. Thus, highly accurate 3D coordinates for each laser point can be calculated based on range measurement, angular measurement, position and orientation information. Additionally, MLS data collection rate can be determined by the laser beam repetition rate and scanning mirror-deflecting pattern. Typically, most commercial MLS systems

can reach 50,000 – 550,000 measurements per second, which are capable to produce high-density point clouds data with time-saving measurements (Kukko, 2013).

For navigation solutions, the GNSS receivers can constantly obtain real-time and geo-referenced geodetic coordinates using a GNSS antenna phase unit. Then, an advanced POS system is employed to correct position and orientation information and improve the overall navigation solution especially for survey areas with poor GNSS signals. For instance, an Applanix POS/LV 420 POS system consists of a GNSS antenna, an IMU, and a DMI, while GNSS antennas are used to receive satellite signals and the DMI can be accessed to update precise vehicle velocity (Ussyshkin, 2009). Meanwhile, high-resolution digital cameras (e.g., CCD cameras or panoramic cameras) can be applied to acquire texture information from surrounding objects. Furthermore, by combining laser pulse frequency and field-of-view (FOV) of LiDAR sensors with scan angles and range values between laser scanners and the targets, XYZ-coordinates of point clouds are calculated. Finally, according to the integrated POS system, real-time and highly accurate 3D information of scanned targets can be obtained.

### 2.2.2 Direct Geo-referencing of MLS Data

The principle of direct geo-referencing is elucidated in the Figure 2.3. According to the scanning angle  $\alpha$  and the scanning range  $d$  of a specified point P, the location of point P can be determined in its coordinate system. In addition, the location of point P in the coordinate system of mapping frame can be transformed from the laser scanner system.

Table 2.2 indicates parameters used in the direct geo-referencing transformation, and the coordinate of target point P can be calculated by (Guan, 2013):

$$\begin{bmatrix} X_P \\ Y_P \\ Z_P \end{bmatrix} = R_M^{IMU}(\omega, \varphi, \kappa) \cdot \left( R_{IMU}^S(\Delta\omega, \Delta\varphi, \Delta\kappa) \cdot r_P^S(\alpha d) + \begin{bmatrix} l_X \\ l_Y \\ l_Z \end{bmatrix} + \begin{bmatrix} L_X \\ L_Y \\ L_Z \end{bmatrix} \right) + \begin{bmatrix} X_{GPS} \\ Y_{GPS} \\ Z_{GPS} \end{bmatrix} \quad (2.1)$$

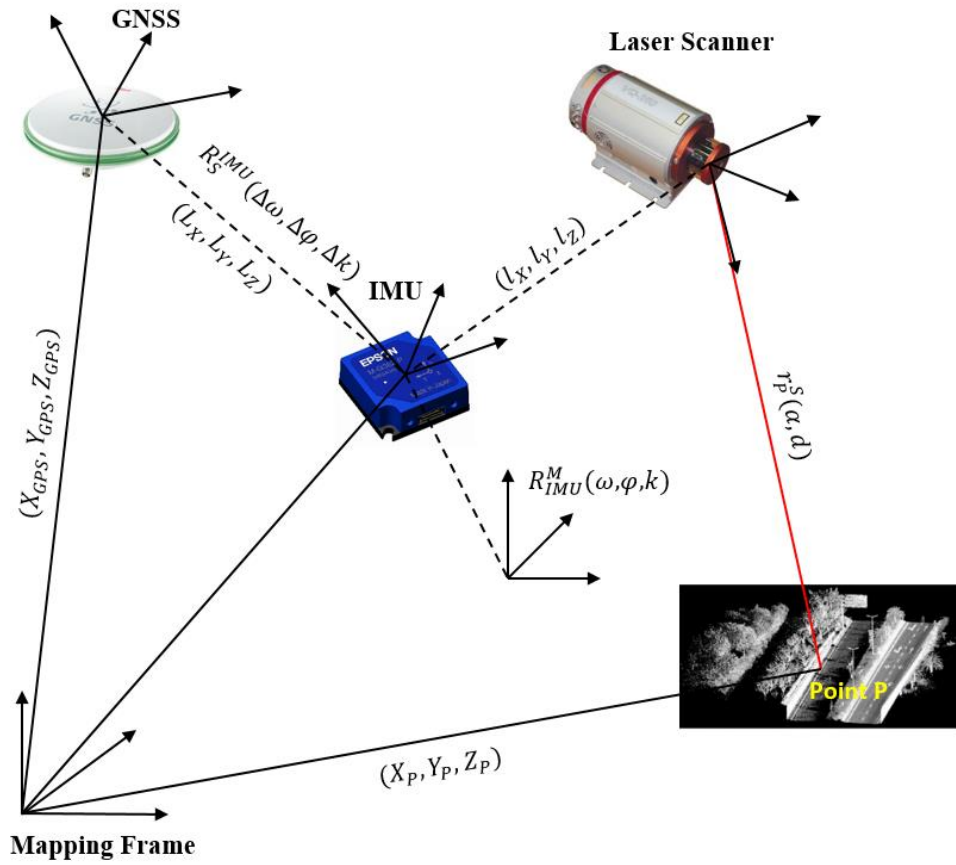


Figure 2.3 Principle of direct geo-referencing.

As shown in Table 2.2,  $[X_P, Y_P, Z_P]^T$  represents the positioning information vector of point P in the given mapping frame;  $[X_{GPS}, Y_{GPS}, Z_{GPS}]^T$  indicates the positioning information vector of the GNSS antenna in the same mapping frame;  $\omega, \varphi, \kappa$  are roll, pitch and yaw details of IMU in the mapping coordinate system;  $\Delta\omega, \Delta\varphi, \Delta\kappa$  are bore sight angles that align the scanners with the IMU;  $\alpha$  and  $d$  refers to the scan angle and scan range of the laser beam; and other parameters are identified through system calibration and measurement.

Table 2.2 Parameters used in the direct geo-referencing.

Parameters	Description	Source
$X_P, Y_P, Z_P$	Coordinate of target P in the mapping frame	-
$R_M^{IMU}(\omega, \varphi, \kappa)$	Rotation matrix from IMU coordinate system to mapping frame	IMU
$R_{IMU}^S(\Delta\omega, \Delta\varphi, \Delta\kappa)$	Rotation matrix between the laser scanner and IMU coordinate system	System calibration & measurement
$r_P^S(\alpha d)$	Relative position of point P in the laser scanner coordinate system	Laser scanners
$l_X, l_Y, l_Z$	The offsets from the origin of IMU to the laser scanner origin	System calibration & measurement
$L_X, L_Y, L_Z$	The offsets from the GNSS origin to the IMU origin	System calibration & measurement
$X_{GPS}, Y_{GPS}, Z_{GPS}$	Coordinate of GNSS antenna in mapping frame	GNSS antenna

### 2.3 Road Surface Extraction from MLS data

In order to generate driving lines correctly and effectively for autonomous vehicles, the first procedure is to extract road surface from raw large-volume point clouds data. A variety of methods and algorithms were developed to detect and extract road surface from MLS data. Typically, these methods are mainly classified into three categories based on: 1) road geometric shape; 2) MLS data characteristics and road properties; and 3) 2D or 3D geometric feature filtering. The following subsections provide a comprehensively review of related studies.

#### 2.3.1 Extracting Road Surface by Road Structure

Some methods detected road surface directly, while others extracted road surface by first detecting and fitting road boundaries. Typically, several model fitting methods, such as RANdom SAMple Consensus (RANSAC), Hough Transform and weighted least-squares linear fitting were employed for direct extraction of planar road surfaces (Smadja et al., 2010, Yuan et al., 2010). For instance, according to Hough Transform approach, Ogawa and Takagi (2006)

directly extracted pavement lanes with curvature, yaw angles and offsets from raw point clouds. Nevertheless, utilizing Hough Transform for large-volume MLS data is inefficient and time-consuming. Moreover, based on maximum entropy theory, Yuan et al., (2010) applied a fuzzy clustering method to segment MLS point clouds, and then employed a weighted least-squares linear fitting algorithm to make a distinction between linear and nonlinear distributed point segments. Similarly, these methods, which require intensive computations to identify road surfaces from large-volume raw point clouds, are time-consuming. Additionally, according to road geometric shape, Smadja et al., (2010) performed a two-step algorithm for road surface detection and extraction. Firstly, each scan line was processed individually using a RANSAC algorithm to determine rough road boundaries. Then, a multi-frame accumulated map was generated to select the curb candidates for further road surface extraction.

In order to improve completeness and computational efficiency, many studies have been conducted to extract road surface by first detecting road sides (Brenner 2009; Yoon et al., 2009; Yang et al., 2013; Kumar et al., 2014; Guan et al., 2014). For example, Yoon et al., (2009) proposed a two-criterion strategy: using slope and standard deviation calculated from raw MLS data for road boundaries detection. Yang et al. (2013) suggested that detecting and tracking road curbs using both road properties (e.g., smoothness and topology) and local shape features extracted from MLS data. Then, using a moving window operator to model different kinds of road edges. In addition, Kumar et al. (2014) applied an automated road edge extraction algorithm by creating a set of lines from raw MLS point clouds and detecting road edges based on intensity, slope and pulse width information. Furthermore, Guan et al. (2014) extracted road curbs by first partitioning the raw MLS data into blocks and profiles according to the vehicle trajectory data, then small height jumps were used to differentiate road surface points and ground points.



### **2.3.2 Extracting Road Surface by MLS Data Characteristics and Road Properties**

In the second category, many methods were developed for pavement detection and extraction by taking MLS data characteristics (e.g., intensity and point density), road properties (e.g., road width and edge elevation) and their combinations into consideration. According to the working principles of a MLS system, point density is negatively correlated with the increase of scanning range from the vehicle trajectory. Therefore, Manaddahar and Shibasaki (2002) suggested that conducting road surface extraction from MLS data with small variation in elevation, slope and high point density. Ibrahim and Lichti (2012) detected ground points based on the variety of point densities. Additionally, other MLS data characteristics, including local point patterns, intensity, pulse width, height and height-generated information (e.g., slope and height jump), were widely applied to road surface extraction. Typically, extracting road surface points requires the combination of several MLS data characteristics (Jaakkola et al. 2008; Yoon et al., 2009; Pu et al., 2011; Kumar et al., 2014). For instance, Pu et al. (2011) presented a rough classification of elements into three categories of point clouds (road surface, ground objects, and off-ground objects) by using data characteristics including size, shape, and road width information. In addition, road properties (e.g., curb height, road elevation and road curvature information) can be applied to separate pavement points from entire MLS data (Guo et al., 2015). Moreover, road curb plays a significant role in the process of road surface extraction owing to the boundaries representation of the road environment. Accordingly, many related studies have been conducted to identify road curb points and then extract road surfaces (Guan et al., 2014; Wang et al., 2015).

### **2.3.3 Extracting Road Surface Based on 2D or 3D Geometric Features**

Road surface detection and extraction can be implemented on 3D point clouds or 2D feature images derived from 3D points. Road segmentation of range scan lines was performed in

2D, Zhao et al. (2003) proposed a method to differentiate geometric features (e.g., buildings, trees and road surfaces) by analyzing height deviation. Accordingly, with the assistance of the scan line segment between vehicle's trajectory points, Wang et al. (2012) implemented a method to detect road edges and extract road surfaces by taking height difference values, altitude mean values and altitude variances into consideration. Subsequently, Yang et al. (2012) extracted road surfaces by generating geo-referenced feature (GRF) images to separate road surface points from the entire MLS point clouds. Riveiro et al. (2015) performed a road segmentation method using a curvature analysis directly interpreted from MLS data. Additionally, Yu et al. (2015) proposed a voxel-based upward growing algorithm to filter out ground points from raw MLS data directly. By calculating normal vector of each point, Hervieu and Soheilian (2013) extracted road curbs efficiently based on angular distances. In order to enhance computational efficiency, trajectory data were widely applied (Pu et al., 2011; Guan et al., 2014; Wang et al., 2015). As mentioned before, the spatial configuration of the scan line relies on related parameters of a specified MLS system (e.g., driving speed, sensor trajectory and scanner orientation). Thus, the high-density pavement points increase the computational efficiency in road segmentation by processing scan lines (Zhao et al., 2003; Yang et al., 2013; Guan et al., 2014). Moreover, based on information derived from scan lines, Manandhar and Shibasaki (2002) classified the MLS point clouds into two separated groups: road points and building points.

Several road surface extraction methods were performed by first segmenting raw MLS point clouds into line sections, then data characteristics and road properties can be further extracted (Cabo et al., 2015; Riveiro et al., 2015). For example, Smadja et al. (2010) suggested that a RANSAC algorithm was performed to determine road edges in each scan line.

Additionally, it is an effective way to decrease time cost and achieve computational improvement at the stage of road surface extraction if generating 2D feature images from massive MLS data. With the assistance of the existing image processing approaches, road boundaries and road surfaces can be identified effectively. In the study conducted by McElhinney et al. (2010), high elevation points were filtered out from the profiles and then determined the rapid slope changes in the spline. In addition, Yang et al. (2013) used a moving window on successive road cross sections interpreted from 3D MLS data to detect corner points of roads.

Table 2.3 is a summary about several kinds of road surface detection and extraction methods. The applications of the elevation, intensity and point density are straightforward and time-saving. However, both completeness and correctness of the corresponding extracted road surfaces are relatively low. Additionally, extracting road surfaces by taking MLS data characteristics and road properties into consideration is flexible and valid to implement but difficult to process large-volume point clouds with large elevation variance. Moreover, the road surface segmentation using scan line focused on road edges detection by analyzing height deviation in urban road environments (Zhao et al., 2013). Furthermore, rapid changes in slope between two adjacent points in 3D point clouds can be applied to identify points belonging to the road edges (Guan et al., 2014; Wang et al., 2015). Meanwhile, some studies concentrated on extracting road surfaces directly from MLS data based on the smoothness of road surface (Zhang, 2016). Compared with 2D features-based road surface extraction, 3D geometric features filtering can segment road surfaces in the global scale. Besides, converting 3D laser point clouds into geo-referenced 2D feature images can extract road surfaces effectively using the existing image processing algorithms and achieve computational improvement (Yang et al., 2013), but it is

challenging to handle steep terrain environment. Therefore, with the assistance of other data sources (e.g., ALS and TLS), the accuracy of extraction results can be improved according to additional high-resolution road information.

Table 2.3 Several road surface extraction methods.

Categories	Methods	Information	Strengths	Limitation	Instances
Road geometric shape	RANSAC	<ul style="list-style-type: none"> <li>Smoothness</li> </ul>	<ul style="list-style-type: none"> <li>No need for trajectory data</li> <li>Computationally efficient</li> </ul>	<ul style="list-style-type: none"> <li>Cannot deal with large MLS data</li> <li>Accuracy requires the model fit the data</li> </ul>	Using RANSAC to fit a plane for ground, and determining the road points within the given distance to the plane (Zhou et al., 2012).
	Hough Transform	<ul style="list-style-type: none"> <li>Line curvature</li> <li>Yaw angles</li> <li>Offsets</li> </ul>	<ul style="list-style-type: none"> <li>No need for trajectory data</li> </ul>	<ul style="list-style-type: none"> <li>Time consuming and computation inefficiency for large volume MLS data</li> </ul>	Road lanes with curvature, yaw angles and offsets can be extracted from MLS data (Ogawa and Takagi, 2006).
	Weighted least-squares linear fitting	<ul style="list-style-type: none"> <li>Linear features</li> </ul>	<ul style="list-style-type: none"> <li>No need for trajectory data</li> </ul>	<ul style="list-style-type: none"> <li>Intensive computation</li> <li>Time consuming</li> </ul>	Performing weighted least-squares linear fitting approach to differentiate linear and nonlinear distributed point segments (Yuan et al., 2010).
MLS data characteristics and road properties	MLS data characteristics driven	<ul style="list-style-type: none"> <li>Slope</li> <li>Intensity</li> <li>Point density</li> <li>Elevation</li> <li>Pulse width</li> </ul>	<ul style="list-style-type: none"> <li>Straightforward</li> <li>No need for trajectory data</li> <li>Could handle steep terrain</li> </ul>	<ul style="list-style-type: none"> <li>Accuracy depends on how the model fit the data</li> <li>Cannot deal with large volume MLS data</li> <li>Need combine with other road surface extraction criteria</li> </ul>	<p>Detecting ground points based on a variety of point densities (Ibrahim and Lichti, 2012).</p> <p>Classifying the point clouds into ground surface, objects on ground, and objects off ground parts by analyzing data characteristics including size, shape, and road width information (Pu et al., 2011)</p>
	Road properties driven	<ul style="list-style-type: none"> <li>Road width</li> <li>Edge height</li> <li>Road curvature</li> </ul>	<ul style="list-style-type: none"> <li>Straightforward</li> <li>Could handle road curves</li> </ul>	<ul style="list-style-type: none"> <li>Cannot deal with large volume MLS data</li> <li>Need combine with other road surface extraction criteria</li> </ul>	Identifying road curbs based on curb height information to further extract road surfaces (Guan et al., 2014, Wang et al., 2015)

2D geometric features	2D features filtering	<ul style="list-style-type: none"> <li>○ Elevation</li> <li>○ Point density</li> <li>○ 2D geo-referenced imagery</li> </ul>	<ul style="list-style-type: none"> <li>○ Straightforward</li> <li>○ High computation efficiency</li> </ul>	<ul style="list-style-type: none"> <li>○ Hard to deal with steep terrain</li> <li>○ Cannot detect the boundary lines</li> </ul>	<p>Using a geo-referenced 2D feature image to segment road surface from MLS data (Yang et al., 2012).</p> <p>Removing high elevation points from the profiles and determining the rapid slope changes in the spline for road surface segmentation (McElhinney et al., 2010)</p>
	Scan line segmentation	<ul style="list-style-type: none"> <li>○ Height deviation</li> <li>○ Scan range</li> </ul>	<ul style="list-style-type: none"> <li>○ Based on the smoothness of the road</li> <li>○ Fit urban road environment with road curbs</li> </ul>	<ul style="list-style-type: none"> <li>○ Need trajectory data for profiling</li> <li>○ The curb-based road segmentation fail in rural area</li> </ul>	<p>Partitioning MLS points into road cross sections to detect border points of ground (Yang et al., 2013).</p> <p>The histogram analysis was implemented along scan line to detect the height deviation and extract road surface (Manandhar and Shibasaki, 2002).</p> <p>Analyzing the height deviation and then performing segmentation of range scan lines to differentiate buildings, trees and road surfaces from MLS data (Zhao et al., 2013).</p>
3D geometric features	3D features filtering	<ul style="list-style-type: none"> <li>○ Height difference</li> <li>○ Normal vector</li> <li>○ Curvature</li> </ul>	<ul style="list-style-type: none"> <li>○ Implement in global scale</li> </ul>	<ul style="list-style-type: none"> <li>○ The complexness of method is determined by calculation of 3D features</li> <li>○ Time consuming</li> </ul>	<p>Road segmentation was implemented using a curvature analysis directly derived from 3D point clouds (Riveiro <i>et al.</i>, 2015).</p> <p>Detecting road sides using angular distance to ground normal (Hervieu and Soheilian, 2013).</p>
	Voxel-based algorithm	<ul style="list-style-type: none"> <li>○ Connectivity in vertical direction</li> </ul>	<ul style="list-style-type: none"> <li>○ No need of trajectory data</li> <li>○ High computation efficiency</li> </ul>	<ul style="list-style-type: none"> <li>○ Cannot deal with point clouds with high elevation variation</li> </ul>	<p>Removing ground points from MLS data by using a voxel-based upward growing algorithm (Yu et al., 2015).</p>

## 2.4 Road Marking Extraction from MLS data

Road markings, as significant elements in traffic management systems, play an inevitable role to provide guidance, warning and bans for all road users (e.g., drivers and pedestrians). Identifying and extracting road markings correctly is crucial for autonomous driving systems to design reliable driving lines and prevent accidents especially in highways and populated urban road environments (Zhang, 2016). Typically, road markings are highly retro-reflective paintings on pavements. Therefore, the relatively high intensity can be regarded as a unique characteristic to identify and extract road markings from MLS data (Jaakkola et al., 2008; Yang et al., 2012; Kumar et al., 2014; Guan et al., 2014; Riveiro et al., 2015).

Based on segmented road surfaces from MLS data, road markings are then identified and extracted by analyzing high reflectance with the assistance of laser intensity values. According to semantic knowledge (e.g., shape and size) and laser intensity characteristics, road marking extraction process is mainly classified into two types: 1) 2D GRF image-based extraction; and 2) 3D point-based extraction.

Most studies extracted road markings from 2D geo-referenced feature images interpreted from 3D point clouds. Therefore, the existing image processing algorithms, including multiscale threshold segmentation, Hough Transform, morphology and Multi-scale Tensor Voting (MSTV) were applied with regard to semantic information of road markings (Toth, 2009; Vosselman et al., 2009; Smadja et al., 2010; Yang et al., 2012; Guan et al., 2015; Riveiro et al., 2015). For instance, based on the generated 2D feature images from raw MLS data, Smadja et al. (2010) performed a global intensity filtering method to roughly detect road markings. Accordingly, with the assistance of intensity distribution in a searching window, Toth (2008) implemented intensity threshold segmentation for the extraction. In addition, Yang et al. (2012) generated a geo-

referenced reflectance intensity image by first and used a Hough Transform approach in four-connected regions of the image to extract broken lane line markings and continuous road edge lines. However, Hough Transform method has a limitation in processing complex types of road markings (e.g., words) while specifying the number of road markings to be extracted. In contrast, the MSTV algorithm has the capability of noise suppression and road marking preservation. Accordingly, Guan et al. (2015) implemented a dynamic multiple thresholding method by determining their relationships between scanning range and intensity values, followed by a morphological nearest operation with a linear road structures. Then, further improvement was achieved by using the MSTV algorithm. Moreover, multiscale thresholding segmentation methods are efficient to overcome intensity inconsistency caused by scanning pattern. In order to reduce the influence of intensity inconsistency, Vosselman (2009) performed a distance-dependence thresholding method, which was expressed as a function of the distance, to detect and extract road markings. Kumar et al. (2014) employed a range-dependence thresholding algorithm to identify and extract road markings from intensity and range images. Additionally, intensity variance has a great impact on the extraction results due to non-uniformity of point clouds distribution. Jaakkola et al. (2008) projected the raw 3D point clouds into the raster images, and then applied image processing algorithms for road marking extraction.

Meanwhile, many studies focused on extracting road markings from 3D point clouds directly rather than from 2D geo-referenced feature images. Typically, extracting road markings from large-volume MLS point clouds with various point densities is a very challenging task. Accordingly, Yu et al. (2015) implemented the road marking extraction directly from 3D point clouds and classified road markings into edge lines, stop lines, zebra crossing lines, arrow markings, rectangular markings and centerlines. Based on road curbs and trajectory data, large



size road markings through spatial density filtering and multi-segment thresholding methods were extracted by first, while Otsu's thresholding algorithm was adopted to determine optimal thresholds (Otsu, 1979). Subsequently, small size road markings were extracted according to the principal component analysis (PCA) and machine learning methods. Additionally, Chen et al. (2009) introduced profile-based intensity analysis algorithms to extract painted markings directly from raw point clouds. Firstly, raw 3D points were segmented into point cloud slices with the assistance of trajectory data. Next, road surfaces were identified based on the geometric properties of road edges, barriers and boundary lines. Finally, linear road markings were successfully extracted by analyzing the peak value of intensity within each scan line.

Table 2.4 is a summary about road marking extraction methods in terms of 2D GRF image-driven extraction and MLS point-driven extraction. Extracting road markings by generating 2D GRF images from MLS data is effective to overcome intensity inconsistency and intensity variance issues caused by scanning patterns. However, extracting complex types of road markings (e.g., words and hatchings) is a very difficult task using 2D feature image processing algorithms. Thus, compared with 2D image-based extraction, MLS point-based extraction methods aiming to directly detect and extract road markings using raw MLS data, is capable to improve completeness and correctness in extraction results within a short computational time. Additionally, their geospatial information of road markings is preserved after extraction, which can be utilized in further applications. Nevertheless, automated extraction of road markings from a mass of 3D laser points especially with huge concavo-convex features and unevenly distributed point clouds is still a very challenging task (Yu et al., 2015).

Table 2.4 Comparison of road marking extraction methods.

Categories	Method	Information	Advantages	Limitations
2D GRF image-based extraction	Multiple thresholding extraction (Toth et al. 2008, Riveiro et al. 2015)	<ul style="list-style-type: none"> <li>○ Intensity</li> <li>○ Scan distance</li> <li>○ Semantic knowledge</li> </ul>	<ul style="list-style-type: none"> <li>○ Efficient to overcome intensity inconsistency and intensity variance problems of MLS data.</li> <li>○ Straightforward</li> </ul>	<ul style="list-style-type: none"> <li>○ Difficult to handle complex road scenes.</li> </ul>
	Hough Transform (Yang et al., 2012)	<ul style="list-style-type: none"> <li>○ Intensity</li> </ul>	<ul style="list-style-type: none"> <li>○ Computation efficiency</li> </ul>	<ul style="list-style-type: none"> <li>○ Difficult to handle complex types of road markings (e.g., words).</li> </ul>
	Multi-scale Tensor Voting (Guan et al., 2015)	<ul style="list-style-type: none"> <li>○ Intensity values</li> <li>○ Scan range</li> </ul>	<ul style="list-style-type: none"> <li>○ Achieve extraction improvement</li> <li>○ Suppress noises</li> <li>○ Preserve road markings</li> </ul>	<ul style="list-style-type: none"> <li>○ Need prior knowledge to select stop iteration criteria.</li> <li>○ Difficult to remove small noisy fragments.</li> </ul>
3D MLS point-based extraction	Deep learning and PCA (Yu et al., 2015)	<ul style="list-style-type: none"> <li>○ Small road marking types</li> </ul>	<ul style="list-style-type: none"> <li>○ Efficient for small size road marking extraction.</li> <li>○ Geospatial information of road markings is preserved.</li> </ul>	<ul style="list-style-type: none"> <li>○ Need massive labeled training samples.</li> </ul>
	Profile-based intensity analysis (Chen et al., 2009)	<ul style="list-style-type: none"> <li>○ Intensity</li> <li>○ Trajectory data</li> </ul>	<ul style="list-style-type: none"> <li>○ Do not require lane models.</li> <li>○ Computation efficiency.</li> </ul>	<ul style="list-style-type: none"> <li>○ Difficult to handle complex types of road markings.</li> <li>○ The curb-based road segmentation fail in rural area.</li> </ul>

## 2.5 Road Horizontal Parameter Estimation from MLS data

Horizontal curves have been regarded as an important element in the process of urban road network design and construction. McDonald (2004) indicated that the accident frequency could increase by 34% for per sharp curve per km. Moreover, drivers' behaviours including misperceptions of speed and poor visibility at horizontal curves, can lead to the increase of

potential risks of traffic accidents. Thus, detecting traffic health condition especially at horizontally curved road sections and determining road horizontal parameters (e.g., curvature) are significant for autonomous vehicles to determine reliable driving lines and prevent collisions (Charlton, 2007). Typically, MLS systems provide precise positioning information, high-density point clouds and thermal information, which can be applied to monitor and analyze road conditions (Gräfe, 2008).

Many studies have been performed to extract geometric parameters at horizontally curved road sections by using MLS systems (Gräfe 2008; Karamanou et al., 2009; Gikas and Stratakos, 2012; Holgado-Barco et al., 2015). For instance, Karamanou et al. (2009) developed a software for precise estimations of road horizontal geometric features using a suitably equipped vehicle moving along the road in a two-way trip. Road centrelines were extracted by first with the assistance of trajectory data. Subsequently, the parameters of horizontal features were determined according to a least-squares optimization of the characteristic curves. Moreover, based on dynamic measurements of GNSS, Di Mascio et al. (2012) implemented a procedure to define the road geometry of horizontal elements. Firstly, the centrelines were regarded as the middle points between trajectories in two directions. Then, a least-squares adjustment was applied to estimate the horizontal elements (e.g., straight lines, circle arcs, and clothoids). Additionally, Gikas and Stratakos (2012) performed an automated solution to estimate curvature diagrams and analyze the horizontal geometric features by considering trajectory data. Meanwhile, Lakakis et al. (2013) developed a cost-effective system based on data acquisition from GNSS sensors to calculate the vertical alignment of a road. Holgado-Barco et al. (2015) suggested that semi-automatically extract the road geometry of horizontal alignment from MLS data. The proposed algorithm mainly includes two steps: 1) extracting the related features to

model road axis from MLS data; 2) calculating the geometric design features of the horizontal alignments according to azimuth and curvature information. Table 2.5 is a summary about MLS data-driven methods for the extraction of road horizontal geometric features.

Table 2.5 Summary of horizontal parameter extraction methods using MLS data.

Categories	Data sources	Advantages	Limitations	Examples
MLS point-based or mobile mapping system based techniques	<ul style="list-style-type: none"> <li>○ Mobile laser scanners</li> <li>○ GNSS/IMU</li> <li>○ Trajectory data</li> </ul>	<ul style="list-style-type: none"> <li>○ High data quality provides precise positioning information</li> <li>○ Efficient for small-size road network</li> </ul>	<ul style="list-style-type: none"> <li>○ Some results validation are usually non-quantitative due to the lack of a comparative ground-truth.</li> <li>○ Heavily depends on data quality of trajectory.</li> </ul>	<p>Based on trajectory data, Di Mascio et al., (2012) performed a solution for road geometry extraction of horizontal alignment.</p> <p>A least-squares optimization was employed to extract horizontal curves from MLS data (Karamanou et al., 2009).</p>

## 2.6 Chapter Summary

This chapter introduced backgrounds about autonomous vehicles and 3D high-definition roadmaps by first, including basic information of autonomous vehicles and their requirements for 3D high-definition roadmaps. Accordingly, the significance and necessity of developing reliable driving lines for autonomous driving at horizontally curved road sections were presented. Then, the principles of a MLS system were described followed by direct geo-referencing of MLS data.

In addition, a variety of state-of-the-art road surface detection and extraction algorithms by using MLS data were reviewed. It can be summarized that MLS point clouds are capable of providing highly accurate and geo-referenced data for road surface extraction. However, large-volume point clouds, unevenly distributed point density and complex road structures of MLS

data account for huge challenges in road surface extraction. Moreover, extracting road surface particularly for complex road environments based on trajectory data is still the most state-of-the-art methods. Therefore, according to Guan (2014), an improved algorithm will be performed to segment road surface especially focusing on horizontal curves in Chapter 3.

Furthermore, many studies concentrating on road marking extraction were reviewed. Extracting road markings from 2D GRF images generated from MLS data is straightforward to implement based on semantic knowledge. Meanwhile, detecting road markings directly from 3D point clouds can achieve accuracy improvement with detailed geospatial information of road markings, but resulting in great difficulties for computational efficiency enhancement. Thus, in allusion to the problems in previous studies, a revised multiscale thresholding extraction algorithm will be proposed in Chapter 3.

Additionally, the existing studies for road horizontal parameters extraction were also discussed. It is identified that the MLS data is more appropriate than satellite imagery to detect and extract horizontal curves information. Based on a prior knowledge of road design regulations, a novel algorithm will be proposed to generate driving lines for autonomous vehicles by using MLS data in Chapter 3.

## Chapter 3 Methodology for Generating Driving Lines

This chapter details the proposed methodology of semi-automated generation of horizontally curved driving lines. Firstly, Section 3.1 introduces the specifications of a RIEGL VMX-450 system. Then, the study area and data collection are detailed. Section 3.2 presents a step-wise methodology, including curb-based road surface extraction in Section 3.3, multiscale thresholds-based road marking extraction in Section 3.4, and best-fitting curve-based driving line generation at horizontal curves in Section 3.5. Finally, methods for accuracy assessment of road marking extraction and driving line generation are presented in Section 3.6.

### 3.1 Data Collection

The MLS point cloud datasets used in this study were collected by a research team at Xiamen University (XMU) using a RIEGL VMX-450 system mounted on a Buick GL8 Van (see Figure 3.1). The VMX-450 system comprises: two fully calibrated RIEGL VQ-450 laser scanners, four RIGEL VMX-450-CS6 digital cameras with pixel array of 2452H by 2056V, and one integrated Applanix POS LV 520 processing system with one GNSS antenna, one IMU, one DMI and one POS computing system (PCS). Based on a point-of-sale synthetic computer system, main components are assembled within a case and mounted on the roof of a motorized vehicle. Table 3.1 indicates the detailed specifications for main components integrated in a RIEGL VMX-450 system. The overall performance is mainly determined by the accuracy of the resultant positions and orientations.

Two dual-frequency GNSS antennas (regarded as a primary receiver and a secondary receiver) are used in the RIEGL VMX-450 system for navigation solution. Both receivers can record raw GNSS satellite observation data and process in a Applanix POS LV 520 navigation

system. In addition, the secondary receiver is employed by a GPS Azimuth Measurement System (GAMS) to calculate additional orientation information.



Figure 3.1 System configuration of a RIEGL VMX-450 system.

Table 3.1 Specifications of the RIEGL VMX-450 system.

Components	Specifications	
Laser scanner component	Laser scanner	RIEGL VQ-450(2)
	Laser wavelength	near infrared
	Measurement range	1.5 - 800 m
	Measurement precision	5 mm ( $1\sigma$ )
	Absolute accuracy	8 mm
	Scan frequency	400 lines/sec
	Angle measurement resolution	0.001°
	Scanner field of view	360°
POS component	GNSS types	POS LV-520
	Roll & Pitch	0.005°
	Heading	0.015°
Imagery component	Camera types	500 MP (6)
	Lens size	2/3" CCD
	Field of view	80°× 65°
	Exposure	8

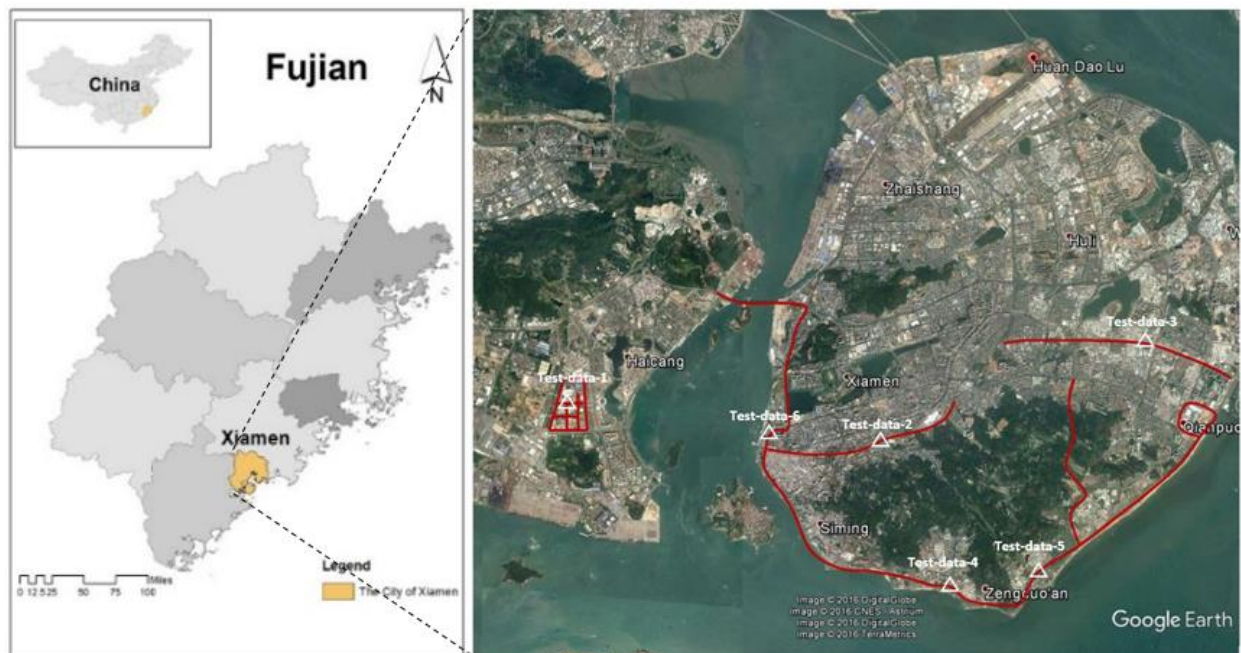
In Figure 3.1, two laser scanners are symmetrically configured on the left and right sides with the tilted angle of these scanners approximately  $135^\circ$ , this configuration is named “X” or “Butterfly” pattern. Each of two RIEGL VQ-450 laser scanners is capable to emit de-noised and gapless  $360^\circ$  profiles with a measurement rate of 550,000 measurements/sec and a scanning rate of 200 profiles/sec. Three kinds of pulse repetition are applied to different scenarios, for instance, 1.1 MHz is designed for short-range and high-resolution MLS applications in urban regions, 600 KHz for medium-range applications, and 300 KHz for long-range applications. Moreover, the maximal measurement range for each RIEGL VQ-450 laser scanner can reach approximately 200 m, and the precision of a RIEGL VMX-450 system can achieve 5 mm ( $1\sigma$ ) (RIEGL, 2017). Additionally, precisely time-stamped images can be complemented using the RIEGL VMX-450-CS6 camera system. According to the RIEGL Datasheet Introduction, RIEGL provides three kinds of software (i.e., RiACQUIRE, RiPROCESS and RiWORLD) for data process and data transformation. For instance, RiACQUIRE is employed to project-oriented acquisition for MLS data, and RiWORLD is applied to transformation of raw scanning data into geo-referenced point clouds.

The XMU team collected 3D MLS point clouds at multiple road corridors around the City of Xiamen, Fujian, China (see Figure 3.2 (a)). The total length of whole surveyed road corridors was over 40 km, including road sections on the Huandao Road, Xiahe Road, Haijing Road and G15 Highway (highlighted in red in Figure 3.2 (a)). The majority of roads are two-side and two-lane roads with fences on both sides. Numerous tall buildings, big trees (e.g., palms and sago cypas) and shafts (e.g., traffic lights and light poles) are along the sides of these roads. In addition, six samples of the surveyed data were selected at horizontally curved road sections as test datasets in order to evaluate the proposed algorithms. Figure 3.2 (b) presents two

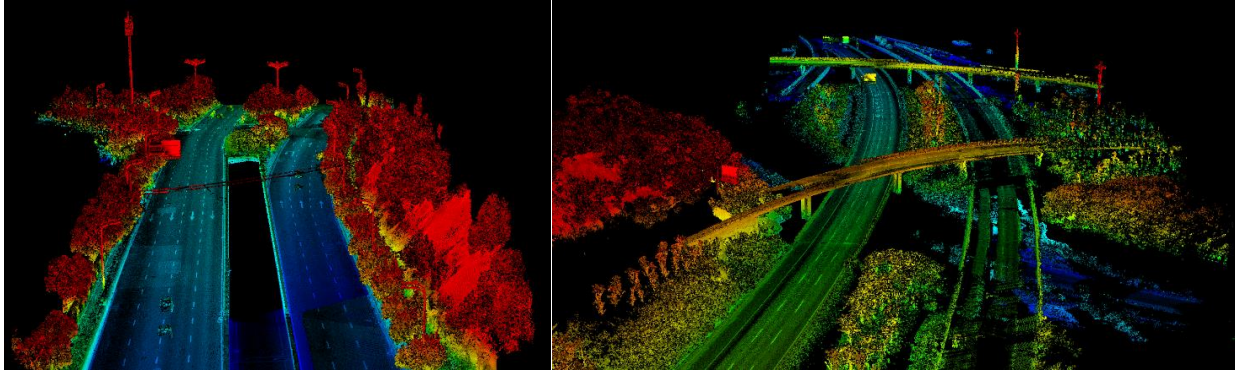


horizontally curved road sections in the study area using MLS data. The UAV imagery obtained by a DJI Inspire 2 can provide 4 cm high-resolution images, which is used to evaluate the accuracy of the generated driving lines. Moreover, the vehicle trajectory data stored in TXT format is more than half million points.

The point densities of the datasets range from 4000 to 5000 points/m<sup>2</sup>. Meanwhile, a large number of digital images were acquired via high-resolution digital cameras with one-second interval at an average driving speed of 40-50 km/h. Additionally, the vehicle trajectory data was obtained based on a navigation solution provided by a POS LV-520 GNSS subsystem. The test datasets were afterward converted into the file format of LAS, which is the standard file format of MLS point clouds. The LAS specification was standardized and developed by the American Society of Photogrammetry and Remote Sensing (ASPRS). As the most recent approved versions, LAS 1.4 specification was released on November 2011.



(a) Location of the City of Xiamen and surveyed corridors.



(b) Horizontal curves in MLS point clouds.

Figure 3.2 The surveyed corridors in Xiamen and horizontal curves in MLS data.

### 3.2 Workflow of the Proposed Methodology

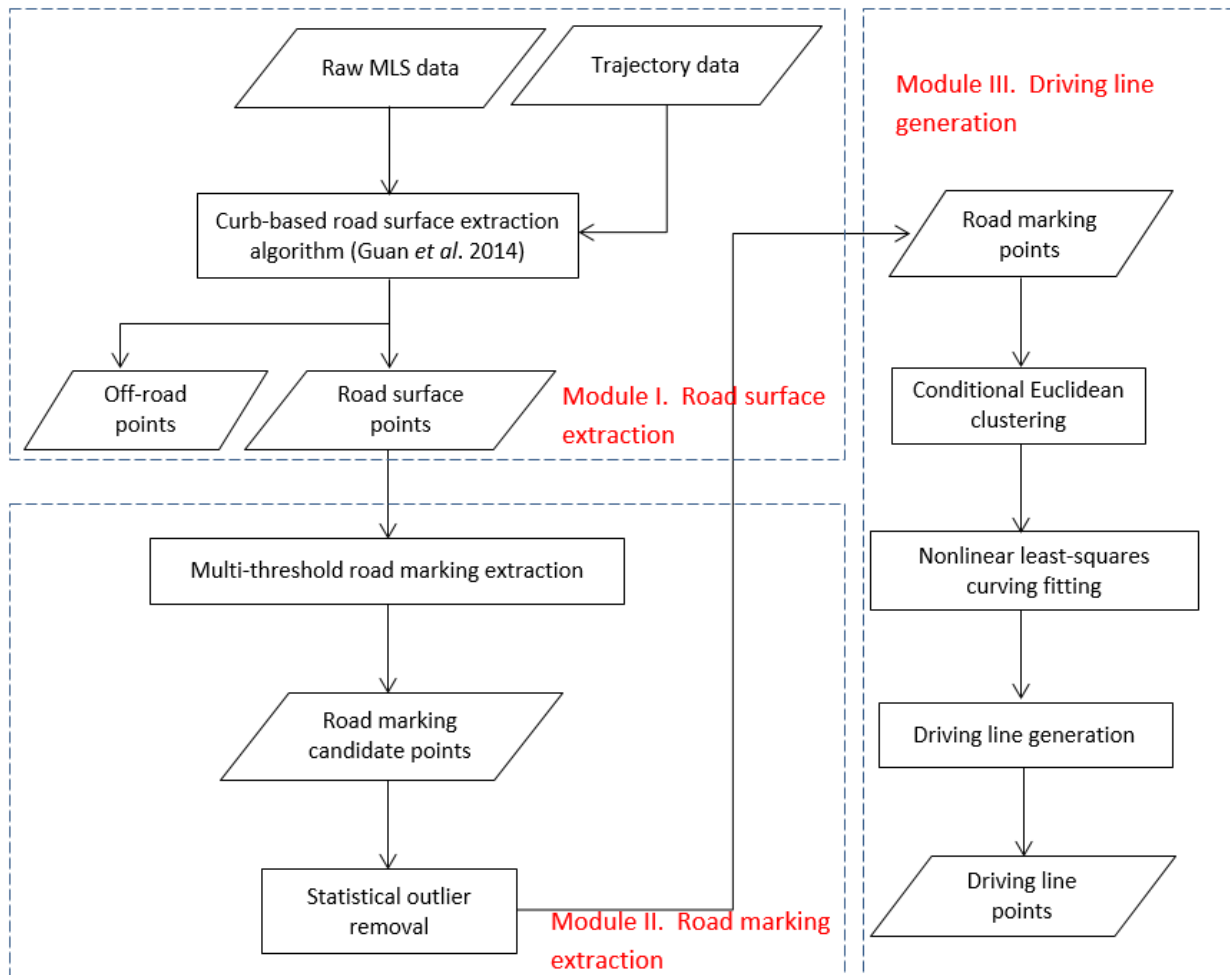


Figure 3.3 Workflow of the proposed methodology.

To guarantee solid and precise navigation solutions for autonomous vehicles in complex urban road environments, this semi-automatic methodology endeavors to generate driving line especially at horizontal curves by using MLS data. This methodology consists of three modules: 1) road surface extraction, 2) road marking extraction, and 3) driving line generation (see Figure 3.3).

The trajectory data that represents the real-time localization information of the moving vehicle facilitates road surface detection and extraction from MLS data. With respect to the assumption that road curbs separate sidewalks or green insulated belts from asphalt pavement surfaces, a curb-based road surface extraction method is carried out to detect height jumps with the assistance of vehicle trajectory data. Firstly, the raw test MLS data is partitioned into a series of data blocks, in each of which a corresponding profile is sliced with a pre-defined width. Next, each profile is gridded to generate a pseudo scan-line, and a principal point is then selected within each grid cell. Consequently, road curb points are identified and extracted depending on both elevation and slope differences. Accordingly, a cubic B-spline interpolation algorithm is carried out to obtain smooth road edges. Moreover, in order to detect and extract road markings, an inverse distance weighted (IDW) interpolation approach is first performed to generate geo-referenced intensity feature imagery. Subsequently, a multi-threshold segmentation algorithm is employed to identify road markings, followed by a statistical outlier removal (SOR) filter in the PCL package to remove noises. After extracting road markings from the generated intensity imagery, a conditional Euclidean clustering method is employed to classify the discrete road marking points into a series of organized clusters based on the distances between a certain point and its nearest neighbours. Furthermore, to identify the best-fitting mathematical functions and implement curve fitting, a nonlinear least-squares curve fitting algorithm is conducted using the

clustered curved road markings. In combination with road design and construction standards, the mathematical functions of desired driving lines are then determined according to the mathematical functions of lane lines, centrelines and edge lines. Therefore, the driving lines at horizontally curved road sections can be generated.

The programming platform of Microsoft Visual Studio 2010 and a third-party programming library Point Cloud Library (PCL) were employed to implement the proposed algorithms, including curb-based road surface extraction, road marking extraction, SOR filter, conditional Euclidean clustering and driving line generation. Meanwhile, CloudCompare V2.6.2 and Quick Terrain Reader V8.0.3 were applied to display and analyze the test datasets and experimental results. In addition, ArcGIS Desktop 10.2.2 was utilized to generate orthoimagery that obtained by an UAV borne imaging system in the same study area.

### **3.3 Road Surface Extraction**

The MLS point clouds captured by the VMX-450 system contain a large number of highly dense and unevenly distributed point clouds, including buildings, trees, traffic infrastructures, pedestrians and other ground points. In order to eliminate the disturbance of non-ground laser point clouds and improve computational efficiency for road marking extraction, the curb-based road surface extraction algorithms is firstly implemented by using the vehicle's trajectory data (Guan, 2013). As illustrated in Figure 3.4, the proposed road surface extraction method mainly consists of four steps:

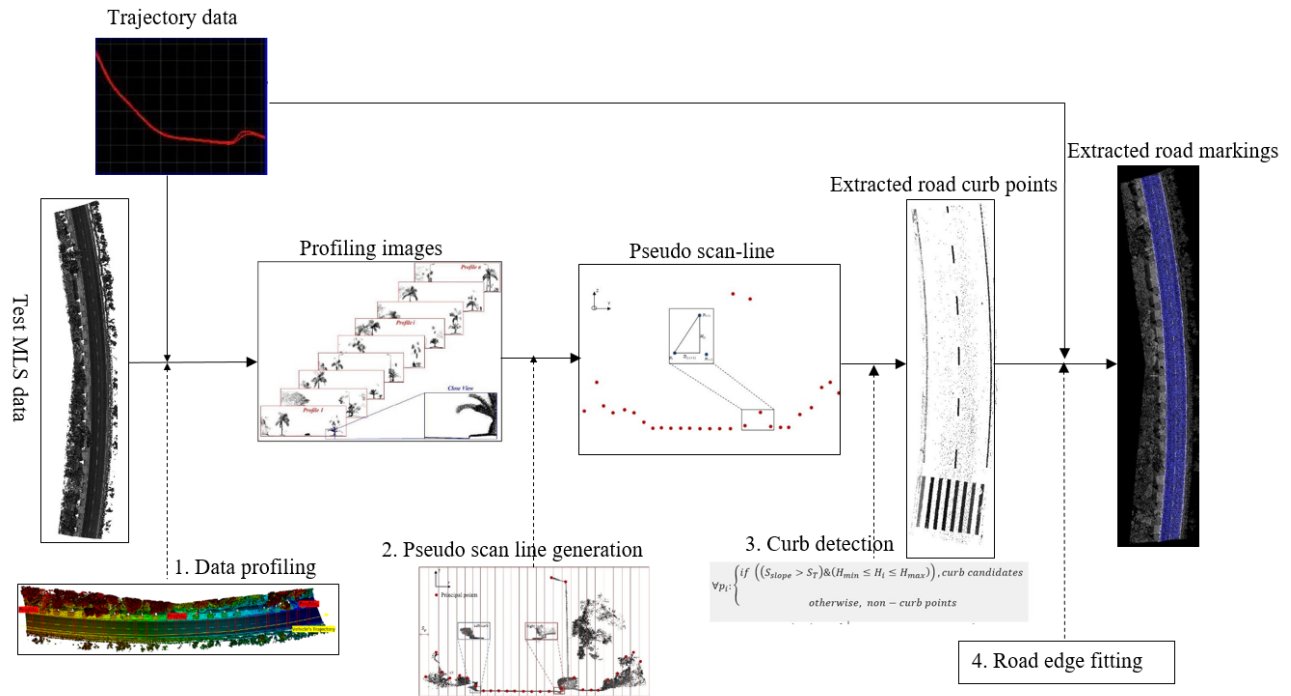


Figure 3.4 Workflow of the proposed road surface extraction method.

Step 1, point clouds profiling. Depending on the vehicle trajectory data, the raw test datasets are partitioned into a sequence of point cloud data blocks, in each of which a corresponding profile is sectioned with a certain width accordingly.

Step 2, pseudo scan-line generation. The point clouds contained in the profile are projected onto the plane perpendicular to the direction in which the vehicle is forward. Each profile is then gridded to generate a pseudo scan-line and a principal point is determined within a grid cell accordingly.

Step 3, road curb detection. Based on both elevation and slope differences, road curbs are detected and extracted from each pseudo scan-line. Based on the final report of the Code for Design of Urban Road Engineering submitted to PRC Minister of Construction in 2012, majority of curb heights within the study area are ranging from 8 cm to 30 cm.

Step 4, road edge fitting. Finally, a cubic B-Spline interpolation algorithm is employed to fit the curb points derived from all pseudo scan-lines into two smooth road edges. All point clouds located between two smooth edge lines are regarded as road surface points. Thus, the point clouds pertaining to pavements are extracted from the raw MLS data.

### 3.3.1 Trajectory-based Point Clouds Profiling

The trajectory data regarded as a driving route that a moving vehicle follows along the road as a function of time, is captured by the integrated navigation solution while laser scanners carry out time-of-flight measurements. In combination with GNSS base station records, the raw GNSS data, and IMU data are processed in the Applanix POSac™ MMS software. The vehicle trajectory data and the preprocessing calibration parameters are then employed to generate geo-referenced point clouds.

Furthermore, according to the vehicle trajectory, the raw MLS data are partitioned into a number of point cloud blocks at a specified width ( $B_g$ ) by first. Accordingly, within each data block, a corresponding profile is sectioned using a given width ( $P_g$ ). Thus, each profile contains point clouds belonging to pavement surfaces and other point clouds pertaining to non-ground objects including buildings, trees, traffic lights, vehicles and curbs. As illustration in Figure 3.5, the blue lines with the width of 25 cm represent sliced profiles. Two parameters (the block width and the profile width) will be discussed in Section 4.2.1. Figure 3.6 indicates a test sample of the raw MLS point clouds, the red rectangles represents the sliced profiles and yellow line indicates the vehicle's trajectory data. As for the VMX-450 system used in this study, the right-handed orthogonal coordinate system is defined as the vehicle frame while its origin is a user-specified point. In addition, the sliced profile images are shown in Figure 3.7, laser points within each

profile are projected onto the planes that perpendicular to the vehicle trajectory. As can be perceived, the road curbs are distinctly identified through a zoom-in view on each profile slice.

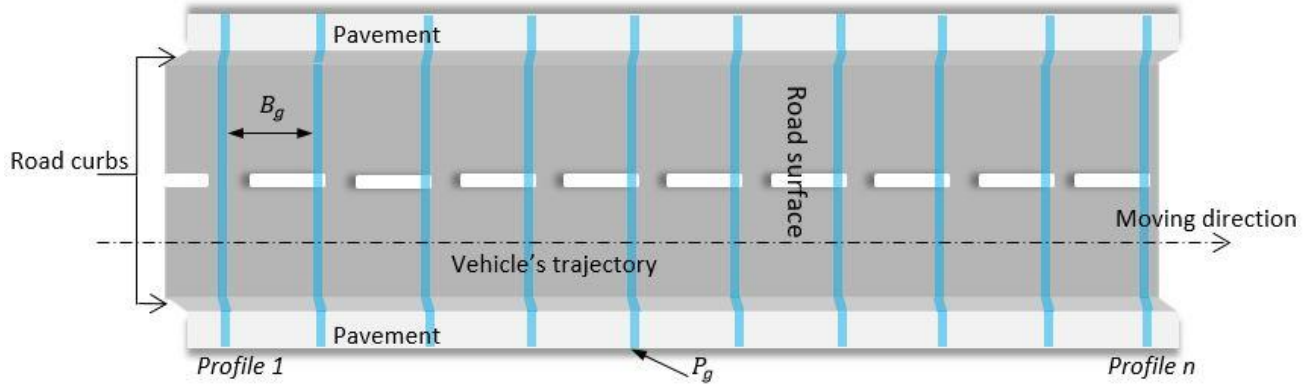


Figure 3.5 Illustration of trajectory-based point clouds profiling.

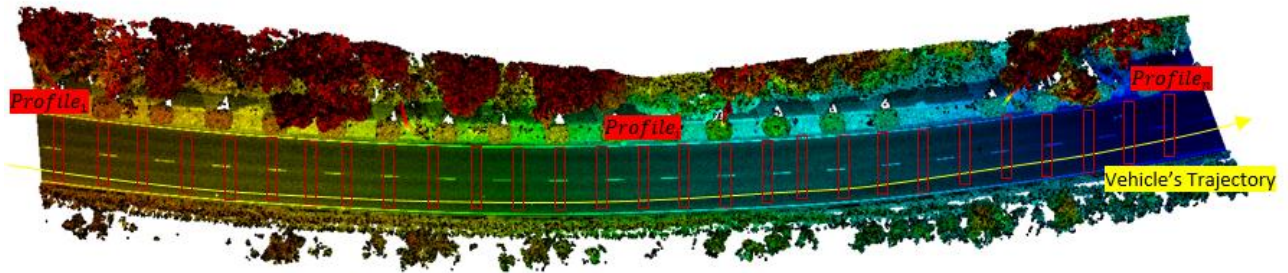


Figure 3.6 Profiling process on the MLS point clouds.

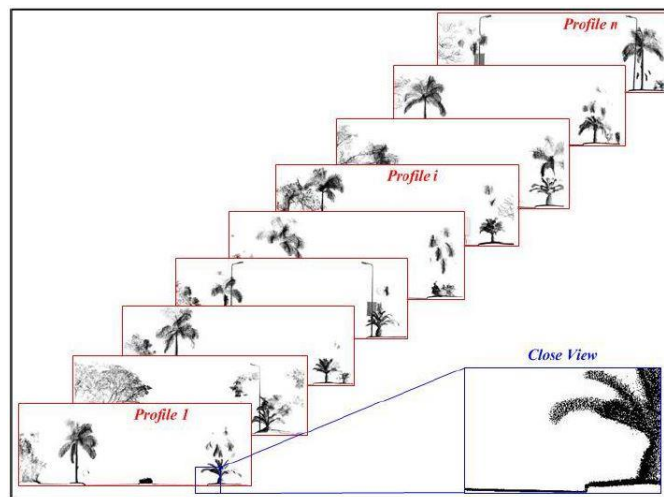


Figure 3.7 The sliced profile images (Source: Guan et al., 2014).



### 3.3.2 Pseudo Scan-line Generation

As for the VMX-450 system used in this study, the orientation of the vehicle frame is defined as a left-handed Cartesian coordinate system so that the positive X, Y, and Z axes towards the vehicle's moving direction, the right of the vehicle, and the top of the vehicle, respectively. As shown in Figure 3.8, all laser points in a profile image are projected onto the YOZ-plane in the vehicle frame. According to two magnifier views, it is demonstrated that the road curbs are sharp height jumps and vertical to the road surfaces. Thus, curb points can be identified by analyzing both elevation and slope-difference thresholds, and road surfaces are then extracted from raw MLS data.

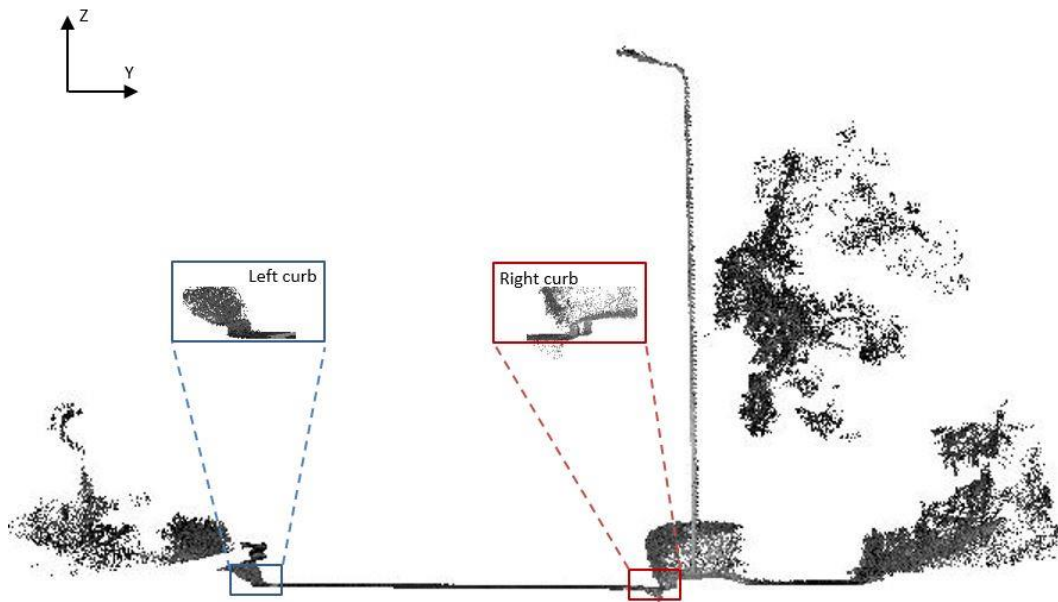


Figure 3.8 Curb identification in a profile image.

Additionally, as shown in Figure 3.9, the principal points can be determined by performing a resampling manipulation by first. In order to select the principal point in each grid cell, a Quick Sort algorithm is carried out to sort and arrange the entire point clouds in this grid cell by considering their elevation attributes. Starting from the point with lowest elevation, the



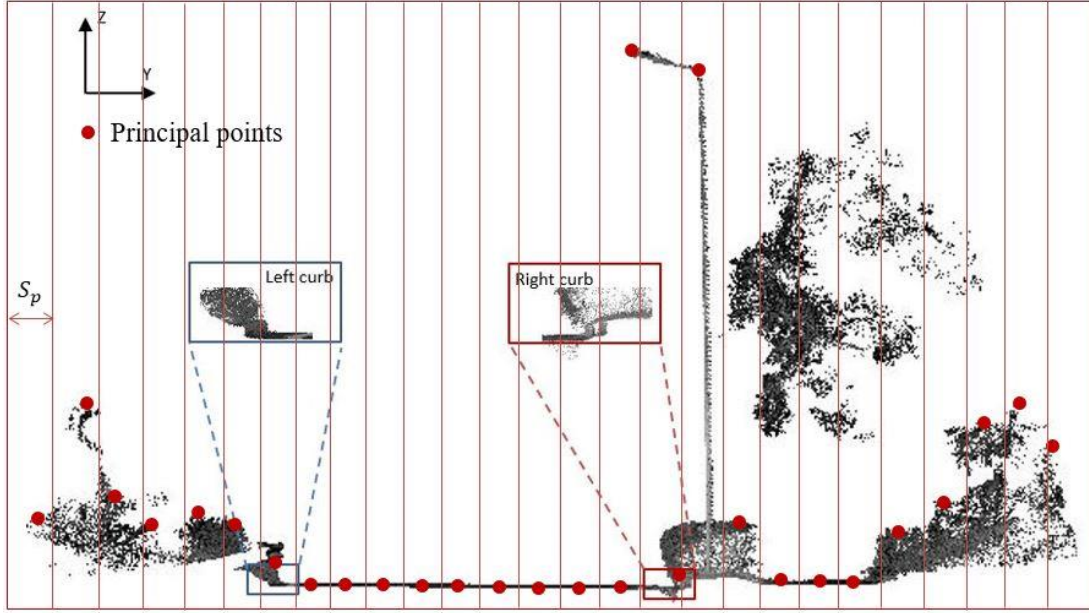


Figure 3.9. The generated principal points in a profile image.

elevation jumps  $\Delta E_i$  ( $i = 1, 2, 3, \dots, N$ ) of two adjacent points are calculated to divide these points into different layers, where  $N$  is the quantity of points in each grid cell. Then, two consecutive points are grouped into a same layer if the elevation difference between these two points is no more than a pre-defined threshold  $E_T$ , namely,  $\Delta E_i \leq E_T$ . Conversely, a new layer is established to partition these two points if the elevation difference is higher than  $E_T$  (namely  $\Delta E_i > E_T$ ). Suppose that 3D laser points pertaining to the road surfaces are located in the lowest layer, a principal point in each grid is then selected by identifying the point with highest elevation within the lowest layer. Thus, majority of outliers (e.g., tree and utility pole point clouds) covering the road surface can be filtered out.

### 3.3.3 Road Curb Detection

In this study, the proposed road surface extraction algorithms for curb detection are performed at the scanning centre according to both slope and elevation evaluation. Indeed, these algorithms mathematically define the slope between two adjacent principal points (highlighted in

red dots) within a generated pseudo scan-line (see Figure 3.10) and the elevation difference of a certain point to its nearest points in the pseudo scan-line.

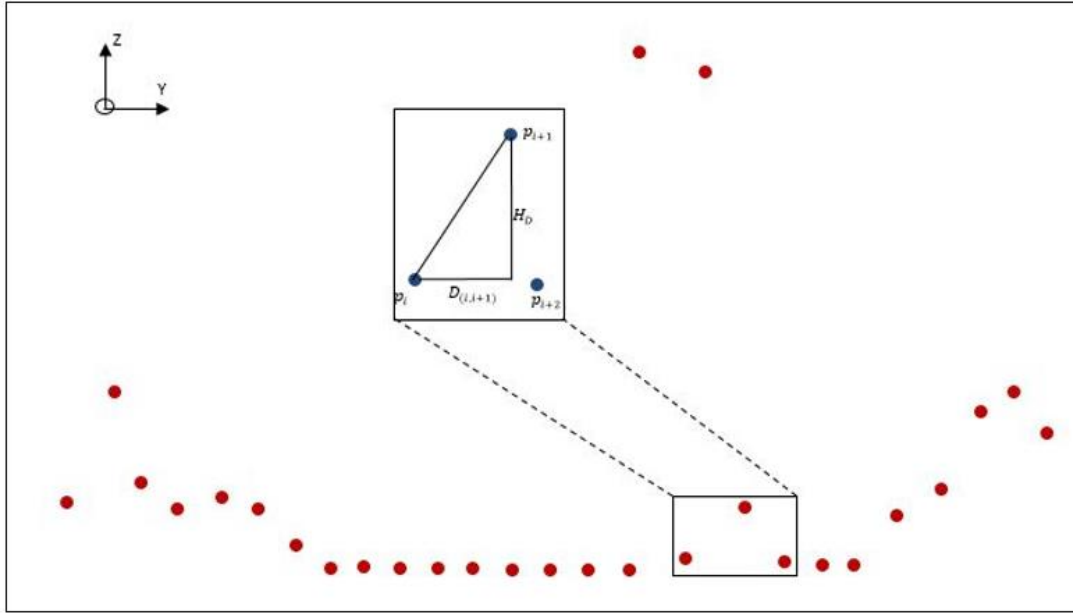


Figure 3.10 A pseudo scan-line of a profile image.

Typically, the MLS points on road edges provide 5-to-30 cm higher elevation than points belonging to pavement surfaces in different countries. Moreover, the slopes at the shoulders of pavements or road curbs are typically larger than the slopes of points belonging to the roadway. Therefore, based on these two criteria, a point can be identified whether it is a curb point or not. Firstly, non-road points such as vehicles and curbs can be detected according to the slope. Then, the curb corners are extracted from the non-road points with the assistance of the elevation difference. Based on the final report of the Code for Design of Urban Road Engineering submitted to PRC Minister of Construction in 2012, most of curb heights are ranging from 8 cm to 30 cm. These two observations are therefore defined by:

$$\forall p_i: \begin{cases} \text{if } ((S_{slope} > S_T) \& (H_{min} \leq H_i \leq H_{max})), \text{ curb candidates} \\ \text{otherwise, non - curb points} \end{cases} \quad (3.1)$$

where  $S_{slope}$  represents the slope of two consecutive neighbour points.  $S_T$  denotes a pre-defined slope threshold.  $H_i$  is the elevation difference of a specified point to its adjacent point.  $H_{min}$  and  $H_{max}$  indicate the minimal and maximal curb height thresholds (e.g.,  $H_{min}=5$  cm and  $H_{max} = 30$  cm in this thesis). Furthermore,  $S_{slope}$  can be calculated by:

$$S_{slope} = \arctan\left(\frac{Z_{i+1}-Z_i}{(X_{i+1}-X_i)^2+(Y_{i+1}-Y_i)^2}\right) \quad S_{slope} \in \left[-\frac{\pi}{2}, +\frac{\pi}{2}\right] \quad (3.2)$$

where  $(X_i, Y_i, Z_i)$  and  $(X_{i+1}, Y_{i+1}, Z_{i+1})$  denote the coordinates of two adjacent MLS points within a pseudo scan-line while X and Y coordinates locating on the YOZ-plane and Z coordinate heading to the elevation direction. Therefore, according to Figure 3.10, Eq. (3.2) can be simplified as:

$$S_{slope} = \arctan\left(\frac{H_D}{D_{(i,i+1)}}\right) \quad S_{slope} \in \left[-\frac{\pi}{2}, +\frac{\pi}{2}\right] \quad (3.3)$$

where  $H_D$  is the height difference between two consecutive points and  $D_{(i,i+1)}$  indicates the distance between two consecutive points on the YOZ-plane. Aware that there are both positive and negative values in Eq. (3.3). A positive slope represents that point queue adding an off-road point from road at the curb edge, and a negative slope value means point queue switching an off-road point to road at the curb edge.

The proposed curb-based extraction algorithms begin the labelling processing by using the vehicle's position, which means the initial labelling is able to enter from the road into curb. Thus, a point will be regarded as a curb candidate if the slope of this point is equal or larger than the pre-defined slope threshold  $S_T$  (i.e.,  $S_{slope} \geq S_T$ ). Moreover, the elevations of these curb candidates are calculated from all the curb candidates to remove non-curb points (e.g., cars and traffic poles) and identify real curb points. If the elevation difference of a road curb candidate

point is within the range of  $[H_{min}, H_{max}]$ , this candidate point can be labelled as a real curb point. Otherwise, it will be grouped into the non-curb points. Based on a prior knowledge of the road design and construction standards, these curb candidate points nearest to the vehicle's moving trajectory are determined as the road curbs.

### 3.3.4 Road Edge Fitting

Since the raw MLS data are sectioned into a sequence of data blocks along the vehicle trajectory at a certain interval, all curb points extracted from the profiles are sparse and discrete. Therefore, an interpolation approach is employed to generate two smooth road edges for each road from the extracted road curb points and eventually separate the road surfaces from the non-road point clouds. The proposed algorithms use the cubic splines to build smooth curves according to a great number of curb points.

The cubic spline interpolation contains weights attached to a flat surface at the points to be connected. Based on these weights, a smooth curve is thus created. It is more stable and reliable for road edge fitting by using splines rather than a polynomial with higher possibility of oscillations between the points.

Theoretically, the proposed interpolation method is defined as a piecewise function as follows:

$$G(x) = \begin{cases} g_1(x) & \text{when } x_1 \leq x < x_2 \\ g_2(x) & \text{when } x_2 \leq x < x_3 \\ \vdots & \\ g_{n-1}(x) & \text{when } x_{n-1} \leq x < x_n \end{cases} \quad (3.4)$$

where  $x_i$  ( $i = 1, 2, \dots, n$ ) indicates X coordinate of the point clouds,  $g_i$  denotes a three-degree polynomial expressed by:

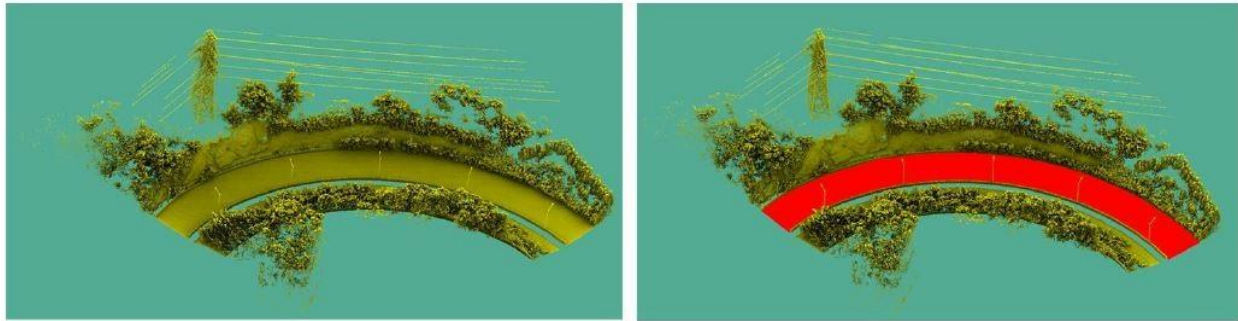
$$g_i(x) = a_i(x - x_i)^3 + b_i(x - x_i)^2 + c_i(x - x_i) + d_i, \quad (i = 1, 2, \dots, n - 1) \quad (3.5)$$

Then, the first and second derivatives of these functions are indispensable to carry out this fitting process, which are described as:

$$g'_i(x) = 3a_i(x - x_i)^2 + 2b_i(x - x_i) + c_i \quad (3.6)$$

$$g''_i(x) = 6a_i(x - x_i) + 2b_i \quad (3.7)$$

Finally, all road points located between two fitted smooth road edges are considered as road surface points. Figure 3.11 shows that a horizontal curve can be effectively extracted from raw MLS data by using the proposed curb-based road surface extraction algorithms.



(a) raw point clouds

(b) extracted road surface (highlighted in red)

Figure 3.11 An Example of extracted road surface (Source: Guan et al. 2014).

### 3.4 Road Marking Extraction

The proposed curb-based algorithms have been described in Section 3.3 for road surface detection and extraction using MLS data. In order to segment road markings completely and effectively, the labelled road surface points are firstly interpolated to generate a 2D GRF image (e.g., intensity imagery). Then, to eliminate the influence of noisy points and improve road marking completeness, a multi-threshold segmentation approach is performed on the produced GRF image to identify and extract road markings using a morphological operation. Moreover, experimental results and discussion are detailed in Section 4.2.3. As shown in Figure 3.12, this road marking extraction method can be described as a step-wise procedure. It mainly consists of the following three parts:

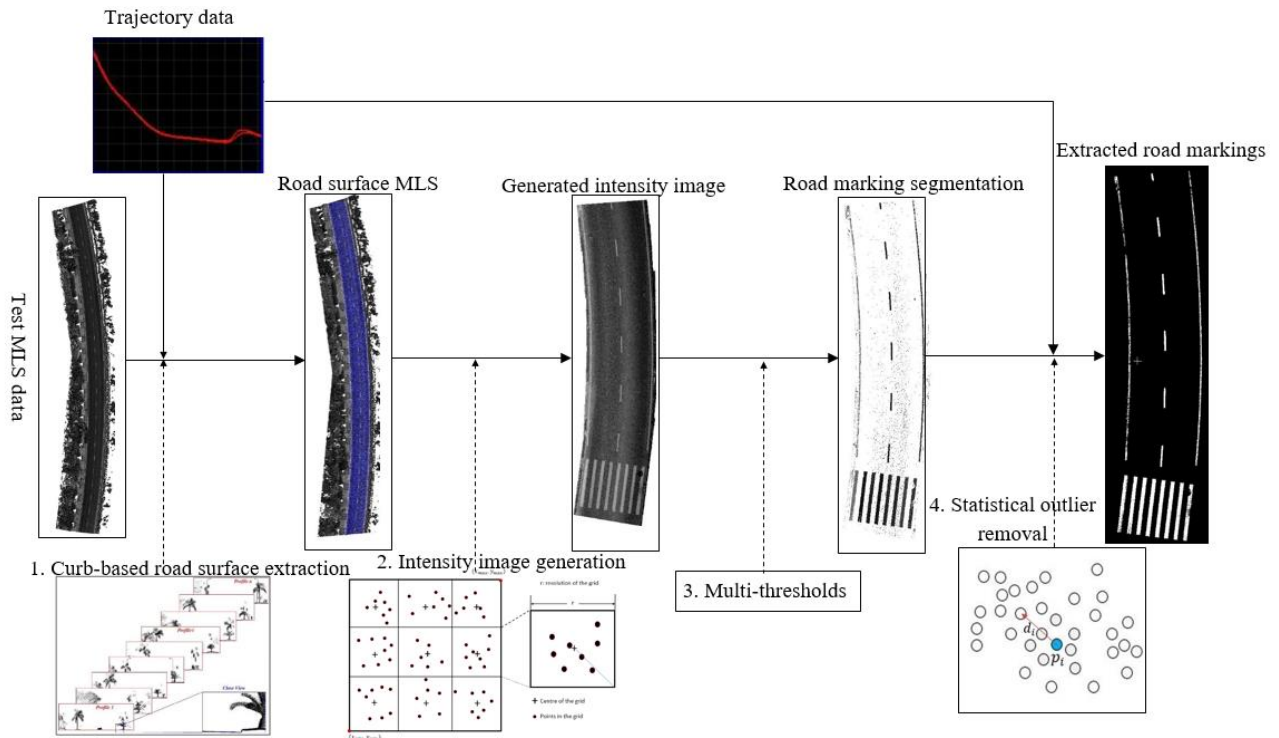


Figure 3.12 Workflow of the proposed road marking extraction method.

Step 1, generation of geo-referenced intensity imagery. Road surface points are first extracted from raw MLS data by utilizing the proposed curb-based extraction algorithms, these road points are then interpolated into geo-referenced intensity imagery based on the IDW method in combination with intensity information and local-global elevation data.

Step 2, multi-threshold extraction. Then, based on the generated intensity imagery, the multi-threshold extraction algorithms are employed to extract road markings (Otsu, 1979).

Step 3, noise removal. Finally, a statistical outlier removal filter is carried out in order to eliminate noises and enhance road marking completeness.

### 3.4.1 Geo-referenced Feature Image Generation

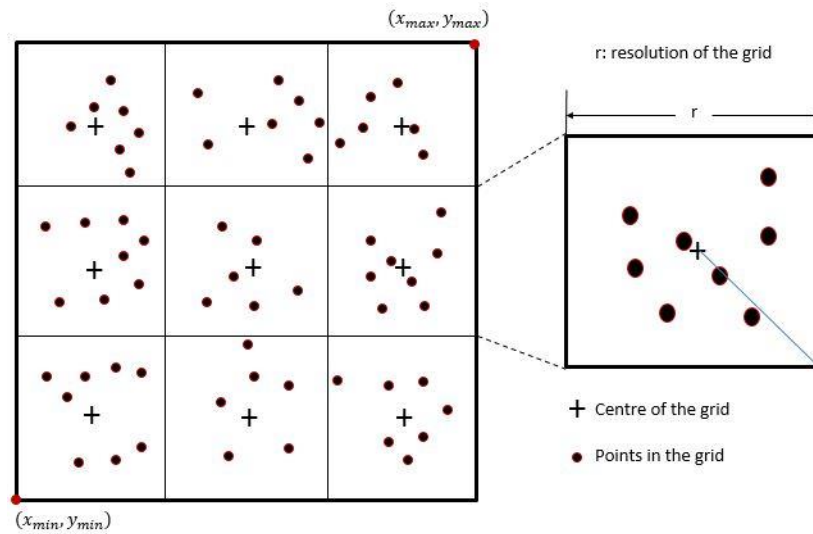


Figure 3.13 An illustration of the determination of gray values.

Road surface points are first extracted from raw MLS data. Subsequently, these extracted road points are afterward utilized to generate intensity imagery, in which the gray value of a pixel can be interpolated from its closest neighbours by utilizing the IDW interpolation method. Although the interpolation process might reduce accuracy, the computational efficiency can be improved greatly particularly for large-volume of MLS data by using the existing 2D image processing algorithms. Guan et al., (2014) proposed an algorithm for the GRF image generation by extending the IDW interpolation. Moreover, the grid resolution determined by point density is a critical parameter to store the results of the IDW interpolation, as shown in Figure 3.13. There are two crucial rules for a geo-referenced intensity imagery generation: (1) the greater intensity value of a certain point, the greater weight should be assigned; and (2) the closer from a certain point to the centre of the grid, the greater weight should be assigned. The detailed mathematic description of two rules can be founded in Guan's (2014) study. Determining a fine grid resolution can improve the accuracy and the computational efficiency for road marking extraction. The smaller grid cell size contributes to higher spatial resolution and more distinct

details with large data volume. Thus, in order to enhance the computational efficiency and generate accurate road marking extraction results, the analysis about the grid resolution used in the IDW interpolation process will be undertaken in Section 4.2.2.

### 3.4.2 Determination of Multi-thresholds

On the generated GRF intensity imagery, a multi-threshold extraction is performed for road marking extraction. However, although the proposed equalization method lessens the influence of intensity imbalance, the intensity values of road markings are gradually reduced rather than being consistent from the vehicle trajectory to its both sides (the red line indicates the vehicle's trajectory and red dots represent the trajectory points), as illustrated in Figure 3.14 (a). This variation is because the intensity values rely on: (1) the incident angle of active laser pulses, (2) the distances from laser scanners to the scanning target, and (3) surface material properties of the scanning targets. Therefore, dynamic multi-threshold extraction algorithms are carried out depending on the range of scanning distances. The local multi-threshold extraction parameters are determined and optimized within various ranges of scanning distances.

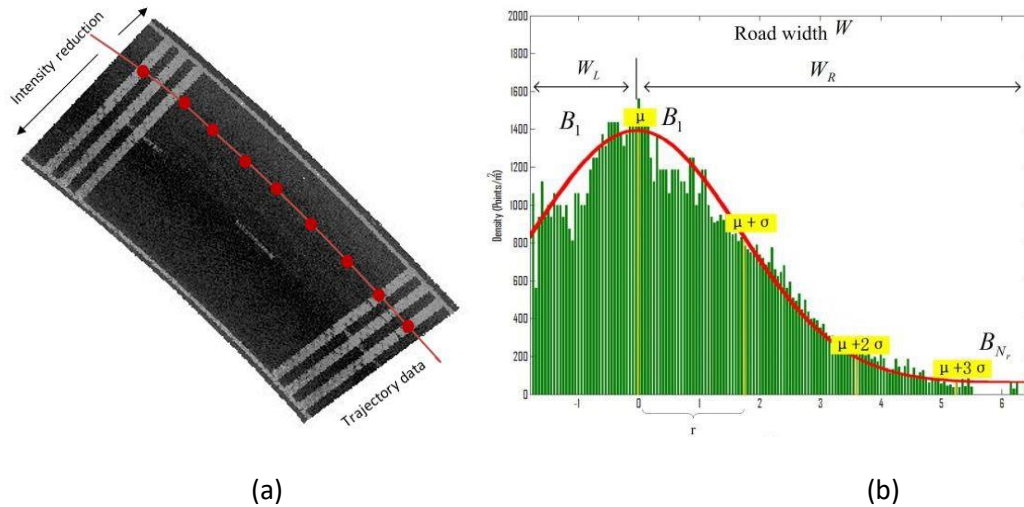


Figure 3.14 Determination of multi-thresholds: (a) the MLS test data, (b) statistical analysis of the test data.



In order to overcome the variation of vehicle trajectory data, road surface points extracted by using the curb-based extraction algorithms are processed block by block. As described in Section 3.3.1, each data block has a corresponding profile. Subsequently, the point density of each profile is statistically analyzed, as shown in Figure 3.14 (b). It is identified that the distribution of point density approximates the Gaussian distribution. Therefore, a Gaussian distribution is adapted to acquire two significant parameters: mean value  $\mu_1$  and standard deviation  $\sigma_1$ . Moreover, intensity variations of the generated intensity imagery follow the “68-95-99.7” rule of a Gaussian distribution (Pukelsheim, 1994). The “68-95-99.7” rule defines about 68% of values within one standard deviation away from the mean, about 95% of values within two standard deviations, and almost 99.7% within three standard deviations. Consequently, the corresponding range is analyzed based on the “ $3\sigma$ ” rule to vertically divide point clouds into a set of bins, for each of which an estimated threshold is determined for road marking extraction.

Then, based on the vehicle trajectory and the estimated road width ( $W$ ) from the generated road surface data, the distances from the vehicle trajectory to the road left side ( $W_L$ ) and the road right side ( $W_R$ ) can be calculated. Subsequently, with the assistance of the estimated mean  $\mu_1$  and standard deviation  $\sigma_1$ , the range ( $r$ ) of one sigma ( $1\sigma$ ) of the Gaussian distribution function is determined. Thus, the number of bins can be calculated as follows:

$$N_L = INT\left(\frac{W_L}{r}\right) + 1 \quad (3.8)$$

$$N_R = INT\left(\frac{W_R}{r}\right) + 1 \quad (3.9)$$

where  $N_L$  and  $N_R$  indicates the number of bins from the scanning centre to its both sides, respectively. Typically, the vehicle trajectory has an impact on the number of bins. For instance, there are five bins in the data block while the vehicle was moving along the right lane of the road

curve (see Figure 3.14 (b)). With the assistance of vehicle trajectory, the fitted Gaussian distribution of the point density can be applied to calculate the number of bins to be sectioned.

### **3.4.3 Multi-threshold Extraction**

The Otsu's thresholding approach (Otsu, 1979), which is widely performed for threshold-based image processing, is then employed to segment road markings based on the discriminant analysis. This method is straightforward to implement and capable of obtaining high-efficiency segmentation results while only two types of classes exist within the imagery. The Otsu's thresholding approach supposes that an image is bimodal and its illumination is consistent, the bimodal brightness is thus calculated by analyzing the different properties of surface materials. Furthermore, the generated intensity imagery can be divided into two classes: road markings as foreground, and others (e.g., road surfaces) as background. Then, their cumulative probabilities and mean levels are determined, accordingly. Consequently, the intensity imagery is segmented automatically by selecting optimum thresholds to minimize the within-class variance.

### **3.4.4 Noise Removal**

Although the proposed multi-threshold extraction can extract road markings effectively, noises (e.g., isolated points, outliers) inevitably exist that reduce the accuracy of extraction results and affect the completeness of the road markings. Therefore, to minimize the effect of noises, a SOR filter in the PCL package (PCL, 2016) was performed to remove noises from the extracted road marking point clouds. The SOR filter is defined by point cloud processing library in the PCL package. Additionally, PCL is a large-scale and open-source library, which consists of a large number of algorithms using C++ programming language for point cloud processing. Moreover, these algorithms and data structures defined in PCL have been widely applied in point cloud applications including point cloud acquisition, registration, filtering, identification,

segmentation, surface reconstruction, feature extraction and visualization. Furthermore, the proposed algorithms in this thesis aiming to generate the driving lines at horizontal curves for autonomous driving are developed to be applied in commercial applications. Thus, the open-source PCL package that provides a high-efficiency and free-of-charge commercial library is appropriate to be directly used in this study.

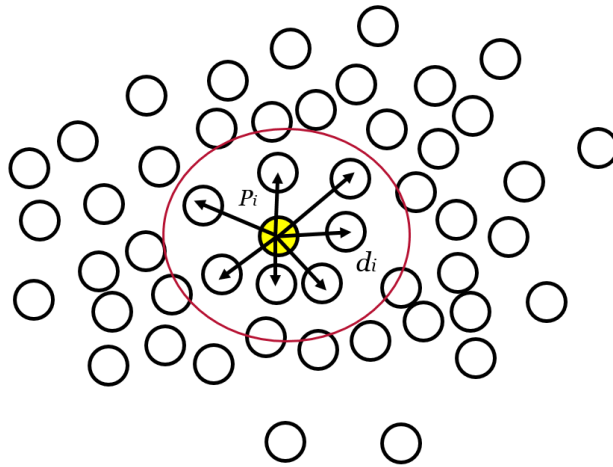


Figure 3.15 The principle of the SOR filter.

According to statistical analysis, image denoising algorithms have been widely developed in a number of research projects (Rusu et al., 2011; PCL, 2016). Firstly, this algorithm defines the number of nearest searching points  $k$  (determined by average point density) from a specified point and calculates their corresponding distances from this point to its neighbours. Then, the mean distance  $d_i$  ( $i = 1, 2, \dots, N_m$ ) of each point  $p_i$  ( $i = 1, 2, \dots, N_m$ ) to its neighbours is computed, where  $N_m$  is the total amount of points in the specified road marking point clouds. Moreover, assumed that the distribution of computed mean distances for all points should be fitted to a Gaussian distribution with the mean  $\mu_2$  and standard deviation  $\sigma_2$ , points that locating outside a thresholding interval are described as noise points and then removed from the road marking points. In addition, the thresholding interval can be determined according to the mean

$\mu_2$  and standard deviation  $\sigma_2$  in the Gaussian distribution. As illustrated in Figure 3.15, it indicates the principle of the SOR filter using the PCL package, which the distances from a certain point  $p_i$  to its neighbour points can be calculated.

In order to reduce the time and space complexity, the proposed image denoising algorithms are applied after extracting road markings from the generated intensity imagery. Figure 3.16 shows road markings extracted by using the multi-threshold extraction algorithms, the tiny white dots around the zebra crossing, edge lines and centreline are regarded as noises. Accordingly, Figure 3.17 shows the refined road markings after noise removal. It is worth noting that most noises are effectively removed by using SOR filter.

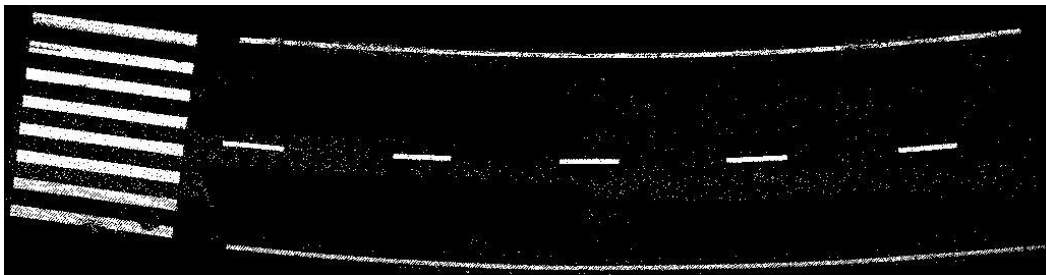


Figure 3.16 Extracted road markings using the proposed method.

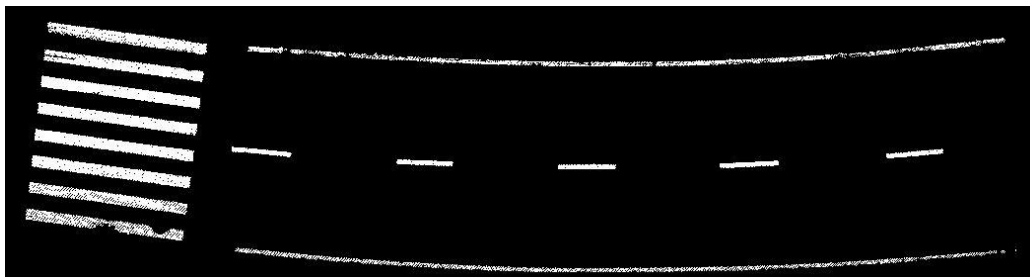


Figure 3.17 Refined road markings after noise removal.

### 3.5 Generation of Horizontally Curved Driving Lines

Although outliers and noises have been removed from the extracted road markings, points pertaining to the same semantic object are still unorganized and isolated. The topological

relationships among the extracted road marking points are ambiguous. In order to generate driving lines at horizontal curves successfully, the sparse and unorganized road marking points are first clustered into topological and semantic objects using the conditional Euclidean clustering method. Then, to determine the best matching functions and perform curve-fitting for curved road markings, a least-squares curve-fitting method is applied on the generated clustered points by minimizing the sum of the squares of the residuals. Furthermore, based on the final report of Code for Design of Urban Road Engineering submitted to PRC Minister of Construction in 2012, the driving lines at horizontal curves are determined for the application of autonomous driving. Thus, as illustrated in Figure 3.18, the driving line generation method consists of three steps:

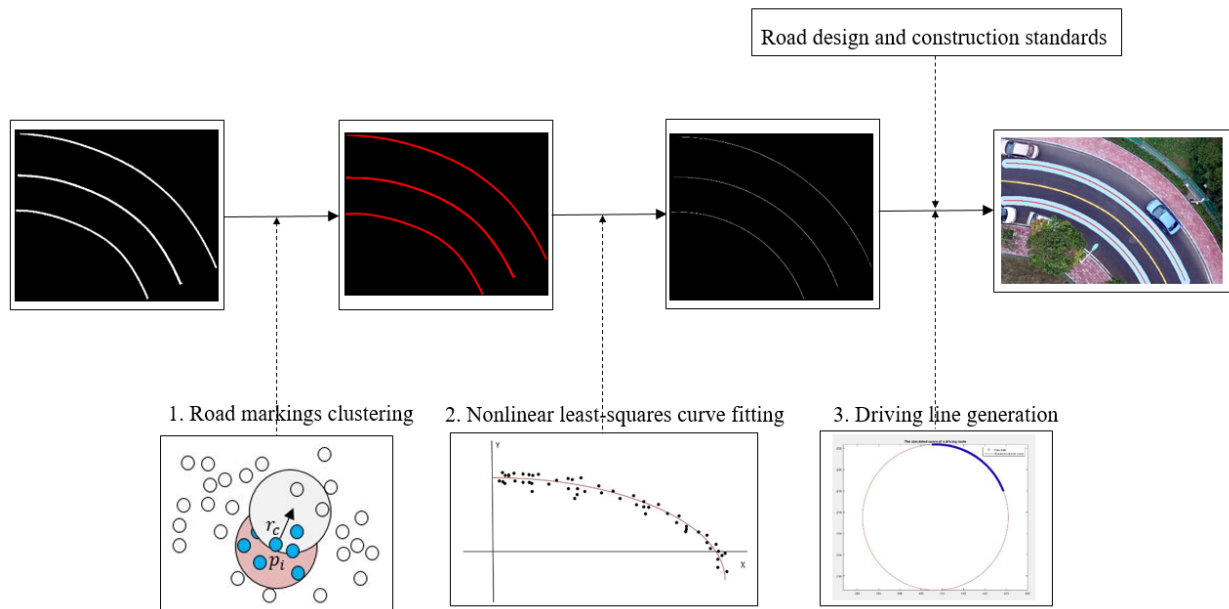


Figure 3.18 Workflow of the proposed driving line generation method.

Step 1, road marking clustering. According to the distances between a certain point and its nearest points, a conditional Euclidean clustering method is employed to segment the 3D discrete road marking points into a series of organized clusters.

Step 2, nonlinear least-squares curve fitting. A nonlinear least-squares curve fitting algorithm is carried out to determine the best-fitting horizontal curves.

Step 3, driving line generation. The driving lines are determined based on the mathematical functions of the generated best-fitting curves and the road design and construction standards.

### 3.5.1 Conditional Euclidean Clustering

There are no definite topological relationships among points in the noise-removed 3D road marking point clouds. In order to identify and distinguish different types of road markings (e.g., centrelines, zebra crossing, lane lines and edge lines), the conditional Euclidean clustering algorithm is then applied to organize these discrete road marking points into topological and semantic point clusters. Moreover, by determining the Euclidean distances between a certain point and its nearest neighbours, this method is capable to group all unorganized points into a set of clusters. Firstly, a pre-defined Euclidean distance threshold  $d_e$  is given by taking point density and resolution of the generated road marking point clouds into consideration. Subsequently, two adjacent points will be assigned into the same cluster if the Euclidean distance  $d_i$  is less than or equal to  $d_e$ . Otherwise, these two points will be grouped into different clusters. The principle of a conditional Euclidean clustering method is presented as follows:

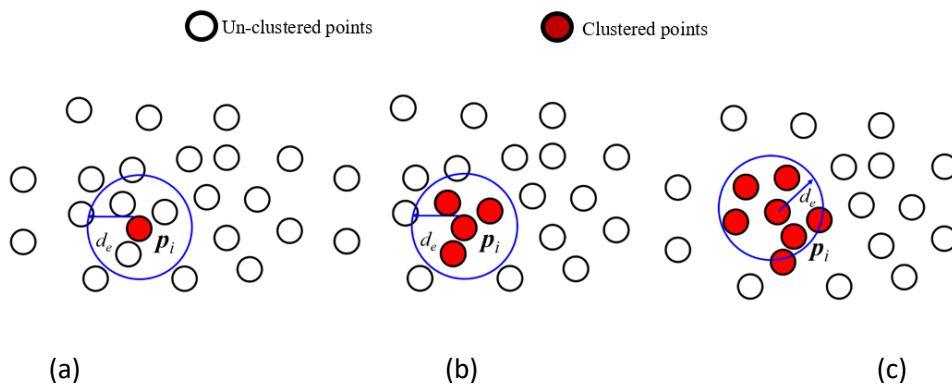


Figure 3.19 The conditional Euclidean clustering method.

As shown in Figure 3.19 (a), all road-marking points are labelled as non-clustered points  $p_i$  ( $i = 1, 2, \dots, N$ ) at first, where  $N$  indicates the total number of non-clustered points. Then, this method randomly selects a point  $p_i$  as the starting point and assigns  $p_i$  with a cluster identifier  $pLabel$ . Subsequently,  $p_i$  is defined as the centre of a sphere, in which  $r_c$  is the radius of this sphere. Next, as shown in Figure 3.19 (b), all non-clustered points that located within the spherical periphery are marked as clustered points (e.g., red points in the figure) and assigned to the same cluster identifier  $pLabel$  as the point  $p_i$  accordingly. Additionally, as illustrated in Figure 3.19 (c), these clustered points are selected as the starting points respectively to perform the conditional Euclidean clustering method, and then the same clustering pattern is carried out repeatedly. Thus, this algorithm consistently labels non-clustered points as clustered points and assigns them with the same cluster identifier  $pLabel$ , while these non-clustered points are within the certain spherical periphery. This repetitive process stops if no more non-clustered points can be detected within the spherical periphery of clustered points. Furthermore, a new starting point is selected from the rest of non-clustered points, then the same clustering pattern is executed until all non-clustered points are marked as clustered points. As a result, points labeled with the same class identifier are grouped into the same cluster. Figure 3.20 indicates two clustering results using the conditional Euclidean clustering algorithm. Figure 3.20 (a) shows power line MLS points and Figure 3.20 (b) presents the guardrail MLS points can be distinguished and clustered effectively after implementing the conditional Euclidean clustering method.

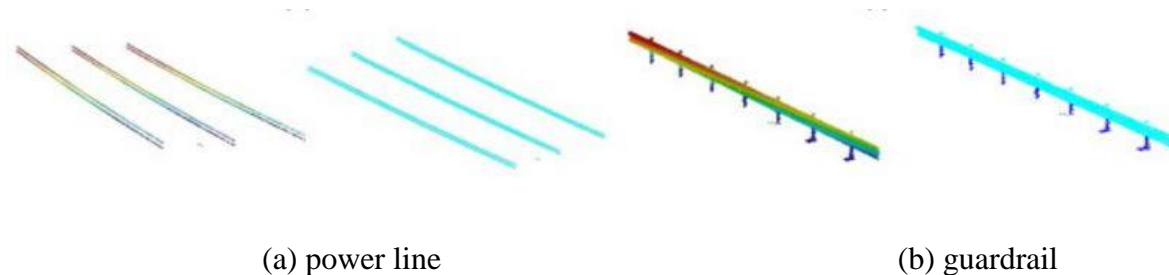


Figure 3.20 Results of conditional Euclidean clustering (Source: Yang et al., 2017).

As shown in Figure 3.20, the conditional Euclidean clustering algorithm has the capability to effectively segment unorganized road marking points into a series of independent semantic point clusters. Based on this method, the segmentation process can be conducted with a high computation-efficiency and low time-complexity. Since the clustering targets in this study are road markings particularly for lane lines, centrelines and edge lines at horizontal curves, a prior knowledge (e.g., shape, width and scanning distance) and related urban street design regulations of the curved road markings can be utilized for complete filtering. For example, several useless clusters (e.g., including road diamond, road words and arrows) for further driving line generation at horizontal curves, are removed to improve the computational efficiency at the stage of clustering. Additionally, the final road marking clusters at horizontal curves are optimized using the following criteria:

$$\begin{cases} \text{reversed clusters, if } d_r \leq d_c \ \& \ w_r \geq w_c \\ \text{removed clusters, if } d_r > d_c \ \text{OR } w_r < w_c \end{cases} \quad (3.10)$$

where  $d_c$  denotes a scanning distance threshold,  $w_c$  indicates a clustered road marking width threshold and  $d_r$ , is the scanning distance. The scanning distance indicates the distance from the vehicle trajectory to the clustered points in the XOY-plane, and the width of a cluster can be determined depending on corresponding coordinates. Accordingly, the clusters will be removed if their scanning distance  $d_r$  is less than the given  $d_c$  or their width  $w_r$  is larger than the given  $w_c$ .

### 3.5.2 Nonlinear Least-Squares Curve Fitting

The flexible mobility and powerful ability of collecting high-density point clouds make MLS data to be applied not only in large-scale road features detection, but also in detailed road parameters extraction and modelling. Moreover, MLS point clouds directly indicate precious 3D coordinates from real horizontally curved scenes, which facilitates the generation of driving lines



in 3D high-definition roadmaps for autonomous vehicles. Thus, in order to determine the best-fitting mathematical functions and further implement curve-fitting, a nonlinear least-squares curve fitting algorithm is employed using clustered curved road markings. Typically, the nonlinear least squares is one of the least squares analysis used to fit a series of  $p$  observations by using a linear model with  $q$  unknown parameters ( $p > q$ ) (Marquardt, 1963). The advantage of nonlinear least squares method is the multiple range of functions with unknown parameters can be fit. Based on the road design and construction standards, majority of horizontally curved road segments are designed as compound curves and spiral curves, a nonlinear least squares curve fitting algorithm is thus used to determine the best-matching mathematical functions of these horizontal curves. By minimizing the sum of the squares of the residuals (i.e., the offsets), this algorithm is capable of fitting a huge number of MLS points from the clustered road markings, and then approximating the nonlinear models to construct the planar B-spline curves for the horizontal curves by iterative optimization. Furthermore, according to the road design regulations, the horizontal curves are normally designed and constructed with small curvatures to meet the requirement of minimum turning radius, provide the broad sight for road users, and decrease the risks of traffic accidents at horizontally curved road sections. The principle of the nonlinear least-squares curve fitting algorithm is described as follows:

The residuals  $\delta_i$  ( $i = 1, 2, \dots, m$ ) defined in the least-squares fitting method indicate the offsets between all clustered road marking points to the desired fitting curves in this study. Subsequently, for a certain point  $p_i(x_i, y_i)$  that is projected on the XOY-plane and given the function as:

$$y_i = f(x_i) \tag{3.11}$$

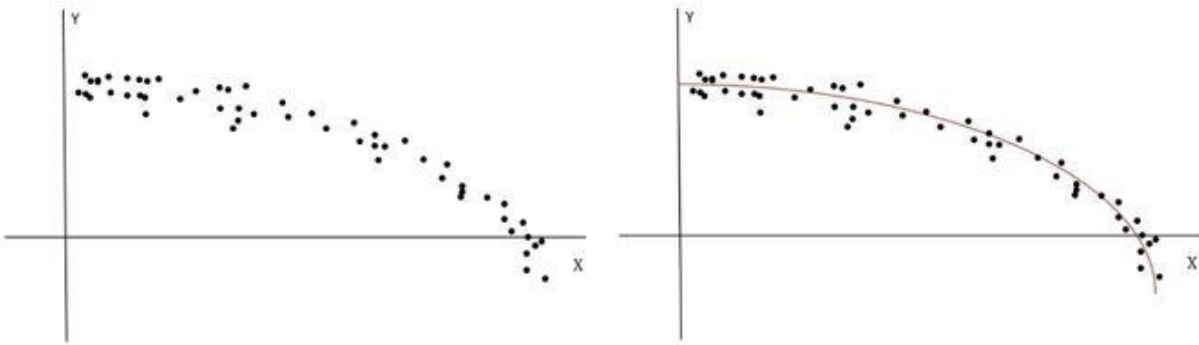
where  $i = 1, 2, \dots, m$ , and  $m$  is the total number of clustered road marking points to be fitted, this algorithm is performed to determine the best-fitting mathematical function as:

$$y_i = g(x_i) \quad (3.12)$$

then, Eq. (3.12) is regarded as the best-fitting function for all points if both the deviation between the approximated curve (e.g., defined by Eq. (3.12)) and the primitive curve (e.g., defined by Eq. (3.11)) and the sum of the squares of the residuals are minimized, which is presented as:

$$\min \sum_{i=1}^m \delta_i^2 = \sum_{i=1}^m (g(x_i) - y_i)^2 \quad (3.13)$$

Figure 3.21 shows a curve fitting result obtained using the nonlinear least-squares fitting algorithm. Figure 3.21(a) presents the independent and discrete points  $p_i(x_i, y_i)$  ( $i = 1, 2, \dots, m$ ) that projected onto the XOY-plane, where  $m$  indicates the total number of the clustered



(a) A scatterplot

(b) A curve generated

Figure 3.21 A curve generated using the nonlinear least-squares curve fitting algorithm road-marking points. Next, assumed that a fitting polynomial is presented to fit all data points using the following equation:

$$y = a_0 + a_1x + \dots + a_kx^k \quad (3.14)$$

where  $k$  represents the degree of the polynomial and  $a_k$  denotes the coefficient of the  $k$ -degree polynomial. Then, the sum of distances between each point  $p_i(x_i, y_i)$  to the proposed polynomial curve, namely the sum of the squares of the residuals, is calculated by:

$$\sum_{i=1}^m \delta_i^2 = \sum_{i=1}^m (y_i - (a_0 + a_1 x + \dots + a_k x^k))^2 \quad (3.15)$$

$$a_0 \sum_{i=1}^n x_i^k + a_1 \sum_{i=1}^n x_i^{k+1} + a_2 \sum_{i=1}^n x_i^2 + \dots + a_k \sum_{i=1}^n x_i^{2k} = 0 \quad (3.16)$$

furthermore, the partial derivative of the residuals is indispensable to obtain the values of these coefficients  $a_k$ , which is described using a simplified matrix as follows:

$$\begin{bmatrix} 1 & x_1 & \dots & x_1^k \\ 1 & x_2 & \dots & x_2^k \\ \vdots & \vdots & \ddots & \vdots \\ 1 & x_m & \dots & x_m^k \end{bmatrix} \begin{bmatrix} a_0 \\ a_1 \\ \vdots \\ a_k \end{bmatrix} = \begin{bmatrix} y_1 \\ y_2 \\ \vdots \\ y_m \end{bmatrix} \quad (3.17)$$

therefore, the coefficient matrix  $A = [a_0 \ a_1 \ \dots \ a_k]^T$  can be obtained and the corresponding fitting curve for the clustered road-marking points is afterward determined, as shown in Figure 3.21 (b).

As illustrated in Figure 3.21, the nonlinear least-squares curve fitting algorithm is capable of determining the best-fitting curve for a large number of discrete points. Since all data points used in this method are derived from the clustered road markings (e.g., centrelines and edge lines), the related road design and construction standards are conducive to provide useful road information (e.g., horizontal curvature) for calculating the coefficients of curve-fitting polynomial. Moreover, in order to overcome the challenges of ambiguous traffic situations and unclear visual clues, such as poor visibility at horizontal curves, the horizontal curvatures of urban streets are regulated less than a pre-defined threshold based on the surrounding terrain, road features and other related control conditions (PRC Minister of Construction, 2012). Thus,

the majority of urban horizontal curves are designed in the form of circular curve and elliptic curve. As mentioned in Section 2.1.3, all horizontal curves used in this study are belong to circular horizontal curves. Based on this basis, the curve-fitting process can be time-saving and conducive efficiently. Figure 3.22 presents a typical circular curve of radius  $R$ , and Table 3.2 summarizes all elements of a horizontal circular curve.

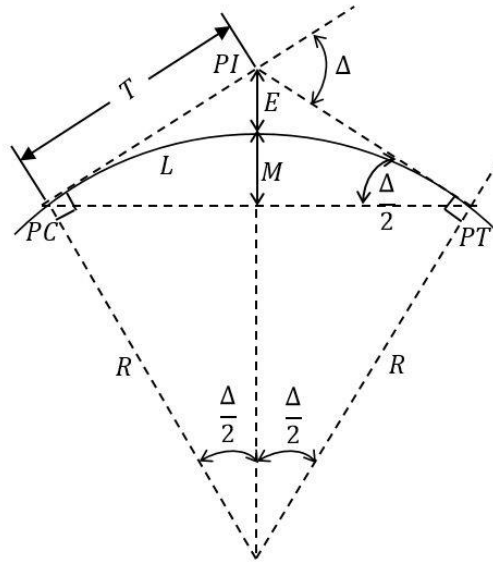


Figure 3.22 The elements of a circular horizontal curve.

Table 3.2 Horizontal circular curve elements.

Symbols	Descriptions	Units
D	Degree of curvature	degrees per 100 ft of centreline
R	Radius of curve (measured to centreline)	ft
L	Length of curve (measured along centreline)	ft
PC	Point of curvature, start of the horizontal curve	-
PT	Point of tangency, end of the horizontal curve	-
PI	Point of tangent intersection	-
$\Delta$	Subtended angle of curve (PC to PT)	degree
T	Tangent length	ft
M	Middle ordinate	ft
LC	Length of long chord (from PC to PT)	ft
E	External distance	ft

### 3.5.3 Driving Line Generation

The driving line generation at horizontally curved road sections from MLS data completely depends on the curve-fitting results of the extracted road centrelines, lane lines and edge lines. As mentioned before, based on the road design and construction standards, these curved road markings approximate to horizontal circular curves or elliptic curves. Therefore, the generated best-fitting mathematical functions for these road markings are in the form of circular function and elliptic function after implementing the nonlinear least-squares curve fitting algorithm. Subsequently, according to a prior knowledge, the generated driving lines should be parallel to the road centrelines and edge lines to guarantee the traffic safety. Additionally, assumed that the curvature of the generated driving line is equal to curvatures of road centerlines or edge lines, and then the centres of these horizontal curves should be the same. Consequently, based on this assumption, the best-fitting mathematical functions of driving lines can be efficiently determined by the adjusting related coefficients of the function (e.g., radius and central position of the horizontal curve). Therefore, the related horizontal circular curve elements defined in this thesis (see Table 3.2) can be determined using the following equations (McCormac et al., 2012):

$$D = \frac{360}{2\pi R} * 100 = \frac{5729.6}{R} \quad (3.18)$$

$$L = \frac{100\Delta}{D} \quad (3.19)$$

$$T = R \tan \frac{1}{2} \Delta \quad (3.20)$$

$$M = R(1 - \cos \frac{1}{2} \Delta) \quad (3.21)$$

$$LC = 2R \sin \frac{1}{2} \Delta \quad (3.22)$$

$$E = R \left( \frac{1}{\cos \frac{1}{2} \Delta} - 1 \right) \quad (3.23)$$

As a result, each element (e.g., degree of curvature and the length of curve) of the generated best-fitting horizontal curve function can be obtained.

### 3.6 Validation

#### 3.6.1 Accuracy Assessment of Road Marking Extraction

To validate the performance and reliability of the proposed road marking extraction algorithms, an accuracy assessment is thus performed based on the manually created reference data.

Table 3.3 presents a confusion matrix for the binary classification, where  $t_p$  and  $t_n$  represent a true positive and negative classification while  $f_p$  and  $f_n$  indicate a false positive and negative classification, respectively. In this thesis, the target class (positive class) is the extracted road marking class, and the road surface class is regarded as the negative class.

Table 3.3 Confusion matrix of binary classification

Class \ Classified	Positive	Negative
	Positive	$t_p$
Negative	$f_p$	$t_n$

In this study, the accuracy assessment mechanism of road marking extraction is based on Recall, Precision and *F1-score* (Powers, 2011). As shown in Eqs. (3.24) to (3.26), recall indicates how complete the extracted road markings are, while precision describes what percentage of the extracted road markings are valid. In addition, *F1-score* represents an overall score with the integration between recall and precision.

$$Recall = \frac{t_p}{t_p + f_n} \quad (3.24)$$

$$Precision = \frac{t_p}{t_p + f_n} \quad (3.25)$$

$$F1-score = \frac{2 * c_{pt} * c_{rt}}{c_{pt} + c_{rt}} = \frac{2t_p}{f_p + f_n} + 1 \quad (3.26)$$

### 3.6.2 Orthoimage Generation

UAV imagery was used as the reference data for validation at the stage of driving line generation. Digital images captured by an UAV with high-resolution optical cameras are capable of capturing rich information about urban road networks. Although the UAV imagery has distortions, the 3D MLS point clouds provide absolute coordinates and geometric information. Thus, optical distortions should be calibrated in order that these UAV images can be regarded as reference data. In this section, the UAV orthoimagery is generated by first to validate the performance of the driving line generation algorithms, and an accuracy assessment is afterward conducted.

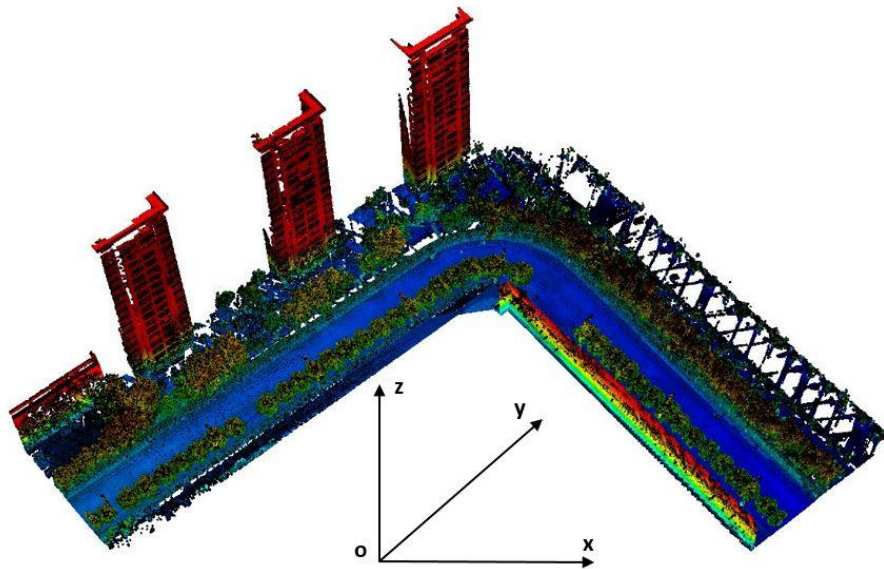


Figure 3.23 Directly geo-referenced 3D point clouds in a local mapping frame.

Figure 3.23 presents directly geo-referenced 3D point cloud within a local mapping frame. The orientation of the mapping frame is specified as the left-handed Cartesian coordinate system so that the positive X, Y, and Z axes towards the vehicle's moving direction, the right of the vehicle, and the top of the vehicle, respectively. These 3D point clouds are projected onto a horizontal XOY-plane and the result contains detailed 2D information. Thus, the generated driving lines from the MLS point clouds can be evaluated by analyzing their projections on the horizontal XOY-plane. Consequently, these driving lines are overlapped on the UAV orthoimagery for both visual inspection and quantitative assessment.

Furthermore, in order to produce orthoimagery of the projected MLS data in the XOY-plane, a set number of ground control points (GCPs) were selected in raw MLS data. Subsequently, (X, Y) coordinates of these GCPs were utilized to generate the base map. The UAV orthoimagery was created using the Georeferencing module packaged in ArcGIS Desktop 10.2.2. Firstly, the UAV images are rasterized into raster layers into ArcMap 10.2.2. Then, in order to determine the spatial information of these raster layers, the relationship is established by connecting locations on the raster layer with their corresponding locations on the base map. As a result, these locations of pixels in the raster layer are calibrated according to the coordinate information of the selected GCPs.

Moreover, determining the number of GCPs has influenced on the accuracy of the generated orthoimagery. Several modules for raster generation have been defined in ArcGIS. Specifically, one GCP is designed for the zero-order transformation, three GCPs for the first-order polynomial transformation, six GCPs for the second-order polynomial transformation, and ten GCPs for the third-order polynomial transformation. The more GCPs, the more distortions in the UAV imagery can be adjusted.



### 3.6.3 Evaluation

In this study, the generated driving lines were overlapped on the corresponding UAV orthoimagery in ArcGIS to conduct visual inspection and quantitative evaluation. The accuracy of the generated driving lines was assessed based on recall and miscoding. Moreover, as indicated in Eq. (3.27), the miscoding represents what percentage of the generated driving lines are located outside of the reference buffer (the reference buffers were created with a given width around the generated driving lines). The following equation was used to calculate the miscoding:

$$Miscoding = \frac{L_r}{L} * 100 \quad (3.27)$$

where  $L_r$  denotes the length of a generated driving line located outside of the reference buffer, and  $L$  indicates the total length of the generated driving line.

## 3.7 Chapter Summary

This chapter presents a detailed workflow for the driving line generation at horizontally curved road sections using MLS data. The rationales of the curb-based road surface extraction, generation of geo-referenced intensity imagery, multi-threshold road marking extraction, SOR filter, conditional Euclidean clustering and nonlinear least-squares curve fitting are presented in details. The performance of road marking extraction is evaluated with three measurements in term of recall, precision and  $F1$ -score. Meanwhile, the generated driving lines can be evaluated by both visual inspection and quantitative assessment with the assistance of the generated UAV orthoimagery. Additionally, several experimental datasets will be employed to evaluate the efficiency and reliability of the proposed algorithms in Chapter 4.

## Chapter 4 Results and Discussion

This chapter presents and discusses the experimental results of driving line generation using MLS point clouds at horizontally curved road sections. Section 4.1 describes the MLS test datasets and reference data used in this study. The experimental results obtained using the proposed step-wise methods are demonstrated and discussed in Section 4.2. Finally, the results of accuracy assessment and comparative study are presented in Section 4.3 in order to evaluate the performance of the proposed methods in reliability and efficiency.

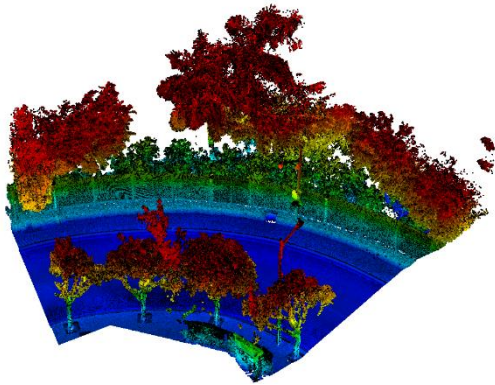
### 4.1 Test Datasets

#### 4.1.1 Test MLS Datasets

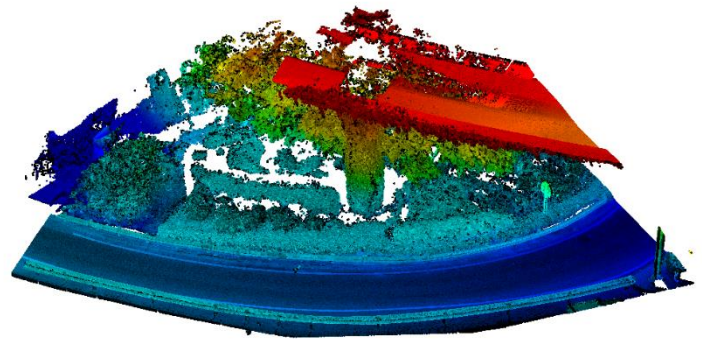
As shown in Figure 4.1, six test datasets were selected from the point clouds obtained by the VMX-450 system. Dataset 1 is an MLS point cloud dataset of a typical two-side and two-lane horizontally curved road section with 6,568,656 MLS points, where contains road-side trees, light poles and fences (see Figure 4.1(a)). Dataset 2 is a test dataset of a one-way horizontal curve with 3,928,845 MLS points, where includes a part of a viaduct (see Figure 4.1(b)). Dataset 3 presents a two-side and two-lane horizontal curve with 5,693,607 MLS points, and the total length is over 126 m (see Figure 4.1(c)). Dataset 4 indicates a two-side and two-lane horizontal curve with 2,063,626 MLS points, where contains several types of road markings including lane lines, centrelines, and zebra crossing (see Figure 4.1(d)). Figure 4.1(e) shows the Dataset 5, a two-side and two-lane horizontal curve with 3,661,745 MLS points in approximately 80 m. Dataset 6 is a point cloud dataset of a one-way horizontal curve with 18,561,253 MLS points, and its length is approximately 200 m (see Figure 4.1(f)).

Experimentally, Datasets 1 and 3 were selected because they contain typical types of horizontal curves (e.g., no sharp turnings) in the study area. Additionally, Dataset 2 was selected

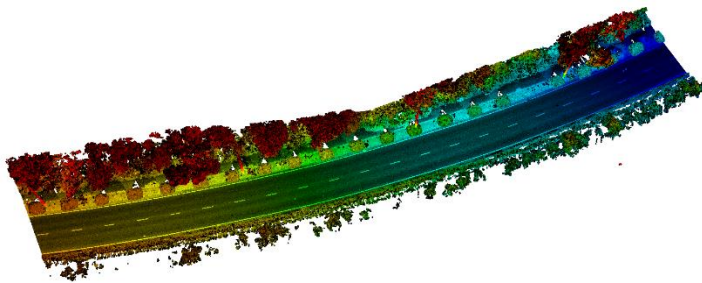
to test if the proposed algorithms will be influenced by occlusions of trees and viaducts. Dataset 4 and 5 were used to evaluate the validity and reliability of the proposed method in the process of road marking extraction. Since autonomous vehicles are capable of dealing with complex road environments, Dataset 6 was therefore used to validate the flexibility and computational efficiency of the proposed algorithms in complex horizontally curved road scenes containing road-side trees, light poles, traffic signs and many types of road markings. Additionally, Datasets 1, 4 and 6 are selected as test datasets used in the comparative study of road marking extraction.



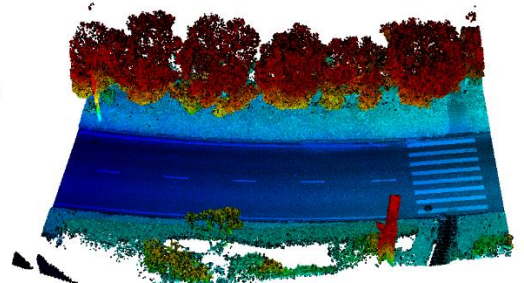
(a) Dataset 1



(b) Dataset 2



(c) Dataset 3



(d) Dataset 4

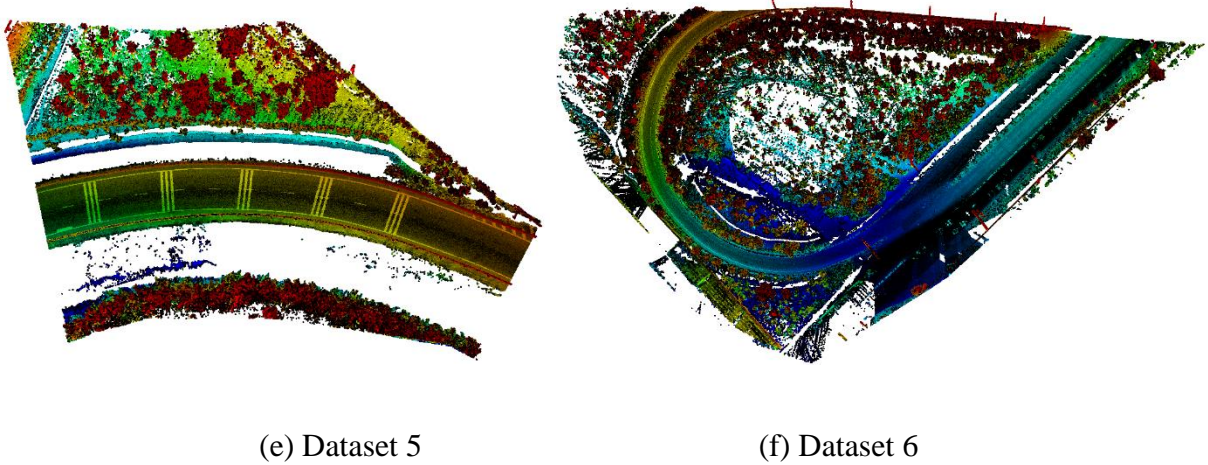
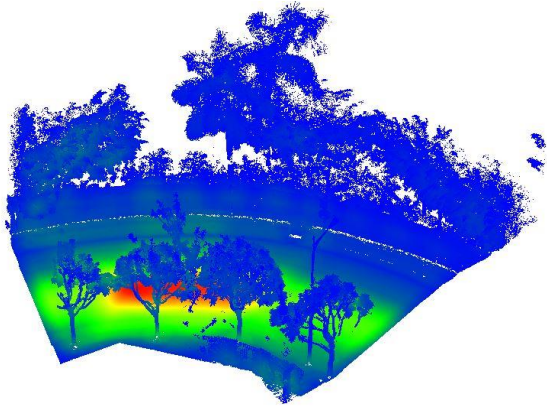


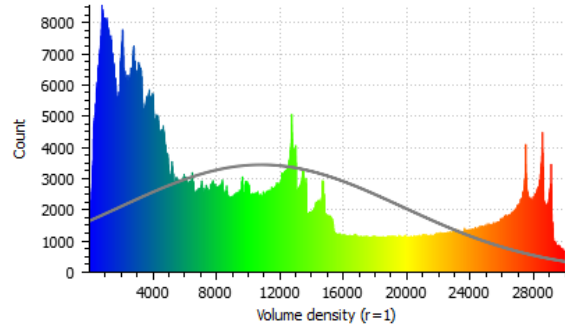
Figure 4.1 Six test datasets used in this thesis.

Figure 4.2 presents point density distributions of the selected six test datasets. As mentioned in Chapter 2, several factors including incident angle, measurement ranges between laser scanners and the scanning targets, and frequency of emitted laser beams, can make impacts on the value of point density. The average point density of each point cloud is various. In this thesis, the point density analysis was carried out by using volume density analysis module packaged in CloudCompare V2.6.2. The test datasets were gridded into  $1 \times 1 \times 1 \text{ m}^3$  volumes by first, the number of each point cloud in these volumes was then determined. Moreover, different colours indicates different point densities of each study area (see Figures 4.2 (a) – (f)). Subsequently, Figures 4.2 (a-1) – (f-1) present the corresponding point density distribution of each test dataset, respectively. As discussed in Section 3.1, the scanning features that near to the vehicle trajectory have higher point densities than those of roadside features and ground objects have higher point densities than off-ground objects. Additionally, Figures 4.2 (a-1) – (f-1) show the average point densities of Datasets 1 to 6 are 10835.45, 3890.21, 2107.64, 2253.02, 2196.74, and 2071.73 points/m<sup>3</sup>, respectively.

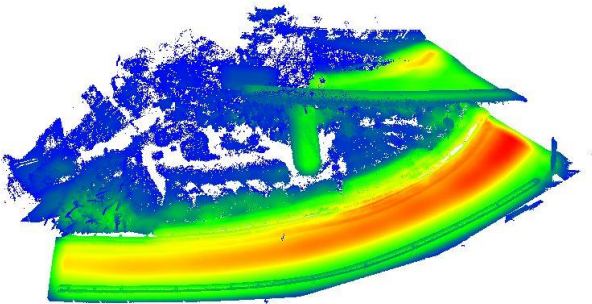


(a) Dataset 1

Gauss: mean = 10835.450195 / std.dev. = 8914.790039 [2563 classes]

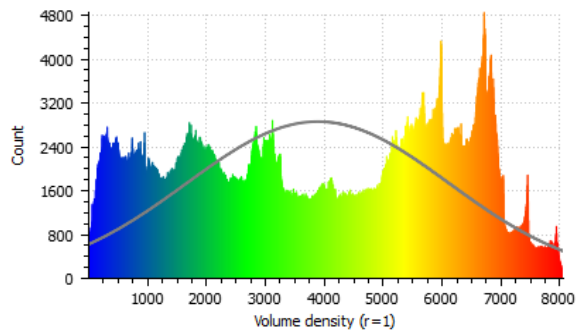


(a-1) Point density distribution chart of Dataset 1

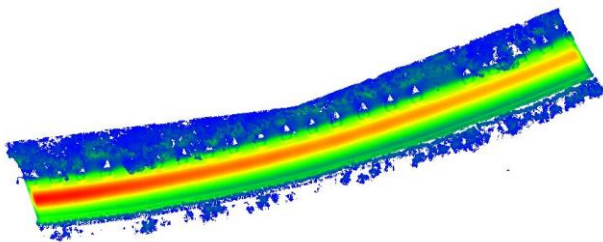


(b) Dataset 2

Gauss: mean = 3890.210693 / std.dev. = 2227.982666 [1983 classes]

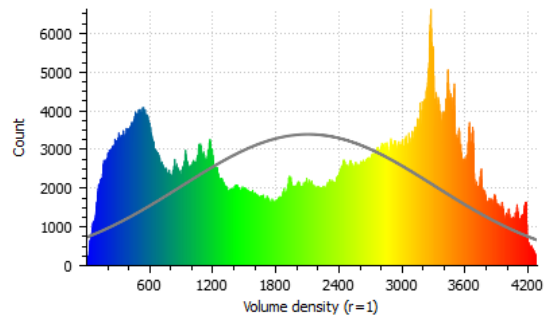


(b-1) Point density distribution chart of Dataset 2



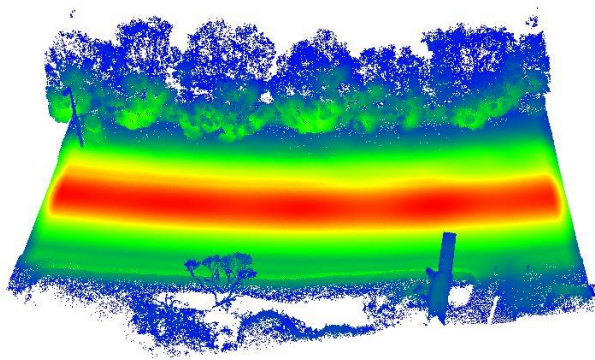
(c) Dataset 3

Gauss: mean = 2107.641113 / std.dev. = 1202.774658 [2387 classes]



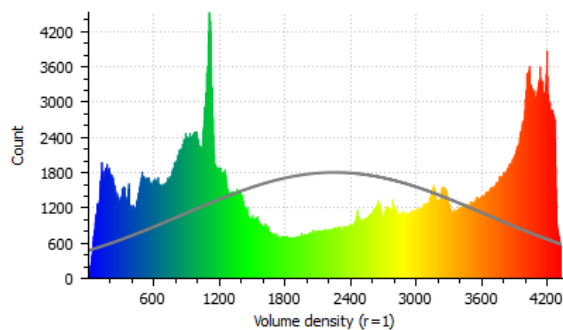
(c-1) Point density distribution chart of Dataset 3



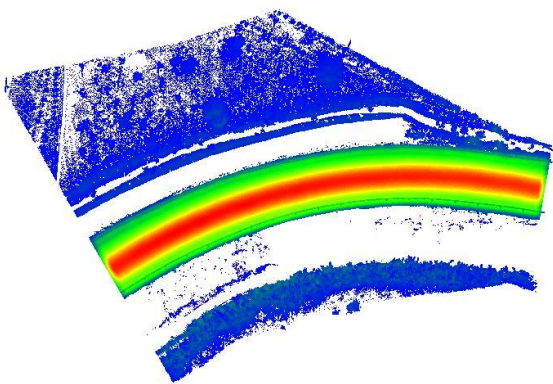


(d) Dataset 4

Gauss: mean = 2253.019043 / std.dev. = 1377.406372 [1437 classes]

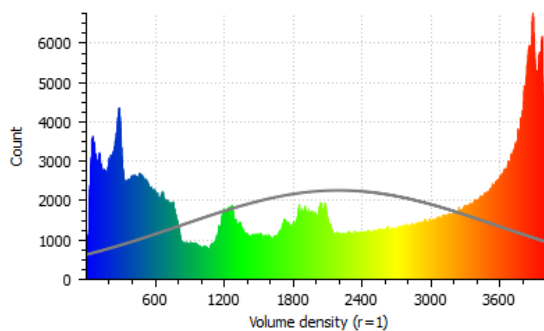


(d-1) Point density distribution chart of Dataset 4

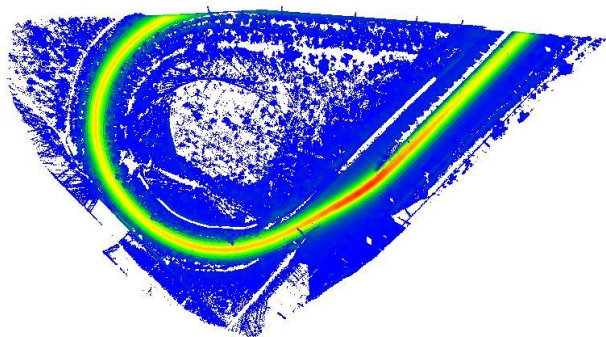


(e) Dataset 5

Gauss: mean = 2196.741699 / std.dev. = 1373.414673 [1914 classes]

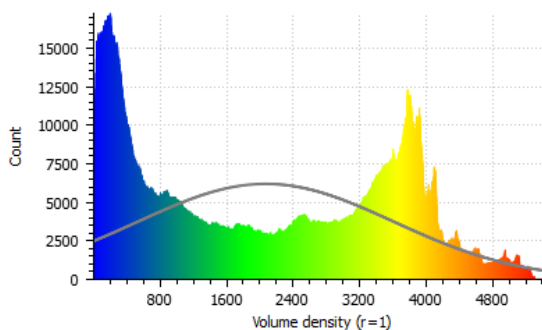


(e-1) Point density distribution chart of Dataset 5



(f) Dataset 6

Gauss: mean = 2071.728760 / std.dev. = 1534.203125 [4309 classes]



(f-1) Point density distribution chart of Dataset 6

Figure 4.2 Point density distributions of six test datasets.

### 4.1.2 Reference Data

High-resolution optical imagery captured by an UAV-borne camera was used as reference data for performance assessment of the driving line generation. These geo-referenced UAV imagery with WGS84 coordinate system was selected to generate the UAV orthoimagery, see Figure 4.3 (a). The manually created reference data was utilized to evaluate the overall performance of the proposed road marking extraction algorithms, see Figure 4.3 (b).

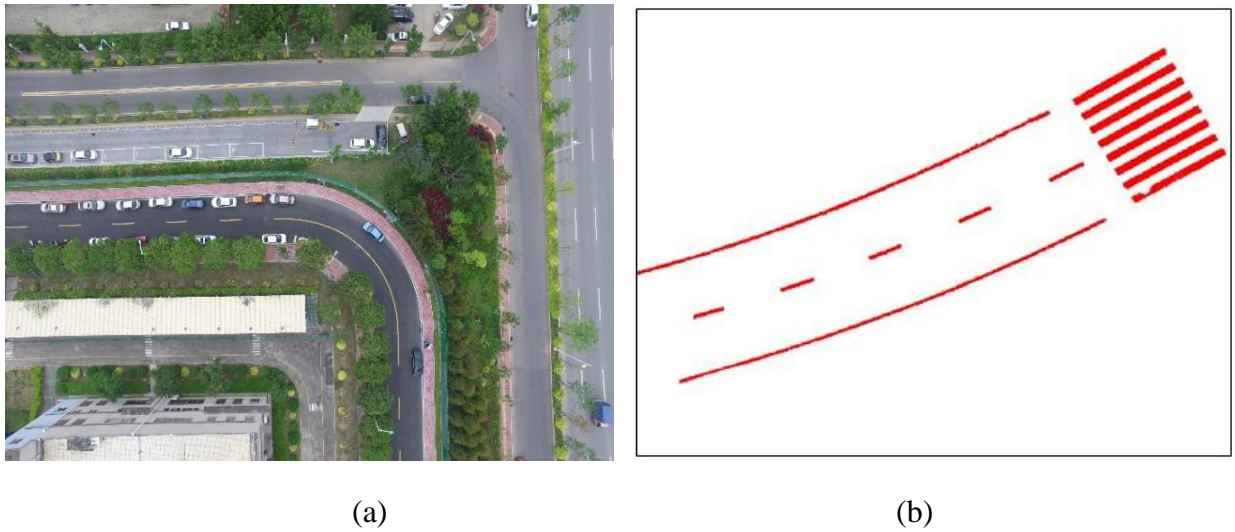


Figure 4.3 Reference data used in this study.

## 4.2 Experimental Results

### 4.2.1 Road Surface Extraction

Several parameters, values and thresholds used in this section are described in Table 4.1. As mentioned in Section 3.3, the extraction results by implementing the curb-based road surface extraction algorithms are determined by six parameters including the width of a block ( $B_g$ ), the width of a profile ( $P_g$ ), the point spacing of a specified pseudo scan-line ( $S_p$ ), the elevation difference of two neighbour points ( $\Delta E_i$ ), the elevation difference ( $H_i$ ), and the slope threshold ( $S_{slope}$ ) for road curb identification. As illustrated in Table 4.1,  $B_g$  and  $P_g$  are used for partitioning and slicing the raw MLS data;  $S_p$  and  $\Delta E_i$  are utilized in the process of scan-line

generation;  $H_i$  and  $S_{slope}$  are employed in the period of road curb detection. Therefore, these parameters have great effects on the efficiency and accuracy of the proposed curb-based road surface extraction algorithms. Based on the road design regulations and a prior knowledge, four parameters including  $E_T$ ,  $H_{min}$ ,  $H_{max}$  and  $S_T$  were pre-defined (see Table 4.1), each of which have a slight influence on the overall performance of the proposed algorithms.

Table 4.1 Parameters for road surface extraction algorithms.

Parameters	Definition	Pre-defined threshold
$B_g$	The width of a block	-
$P_g$	The width of a profile	-
$S_p$	The point spacing of a generated pseudo scan-line	-
$\Delta E_i$	The elevation jump of two adjacent points for determining the principal points.	$E_T = 0.05$ m
$H_i$	The elevation difference for detecting road curbs	Based on a prior knowledge, the minimum height difference and the maximum height difference of the curb are: $H_{min} = 0.05$ m , $H_{max} = 0.30$ m
$S_{slope}$	The slope criterion for detecting road curbs	Based on a prior knowledge, $S_T > \pi/3$

Parameter  $B_g$ , the width of a block, has an influence on the capability of the proposed road surface algorithms since it determines the size of a data block to be sectioned. Consequently, it controls the number of blocks can be acquired for detecting road curbs, and determines the number of curb points can be used to conduct a cubic spline interpolation method. Additionally, parameter  $P_g$  also plays a crucial role in the proposed algorithms, because the value of  $P_g$  determines the number of points to be counted at the stage of pseudo scan-line generation. Moreover, the point spacing of a generated pseudo scan-line can be determined by the



parameter  $S_p$ , which controls the precise position of the extracted road curb points. Therefore, experiments were implemented by using different sets of values for parameters  $B_g, P_g$ , and  $S_p$ .

According to a set of data experiments, the width of a block was set ranging from  $B_g = 0.5$  m to  $B_g = 2.0$  m in this thesis according to the trajectory data and curvatures of horizontal curves. That is, if the horizontal curve is a sharp curve, experiments keep  $B_g = 0.5$  m in order to obtain more points belonging to the road curb for curb detection. Otherwise, a larger value of  $B_g$  was selected to improve computational capability. In addition, the value of  $B_g$  can be controlled by the trajectory data, which directly reflects possible curves by determining the direction of GNSS positions of two consecutive trajectory points. Therefore, the six test datasets were partitioned into 26, 24, 61, 12, 32 and 69 data blocks, respectively. Each data block has a corresponding data profile accordingly. Based on a series of experimentation, the value of  $P_g$  was set to 0.25 m. Each profile was then gridded into a number of grids with an adaptive grid width  $S_p$  of 0.05 m to generate pseudo scan lines. Moreover, based on the final report of Code for Design of Urban Road Engineering, China in 2012, the related road design and construction regulations determine the curb height of urban road networks ranging from 0.05 m to 0.30 m. Figures 4.4 presents road surface extraction results of the six test datasets using the proposed curb-based road surface extraction algorithms. Table 4.2 indicates the number of non-road-surface points that can be removed after implementing the proposed algorithms, which demonstrates the proposed algorithms enhance computational efficiency greatly.

Table 4.2. The number of MLS points after road surface extraction.

Test datasets	Raw 3D points	Road surface points	Percentage of road surface points
1	6,568,656	3,717,442	56.6%
2	3,928,845	1,952,461	49.7%
3	5,693,607	3,275,666	57.5%
4	2,063,626	1,202,819	58.3%
5	3,661,745	2,575,698	70.3%
6	18,561,253	4,714,745	25.4%

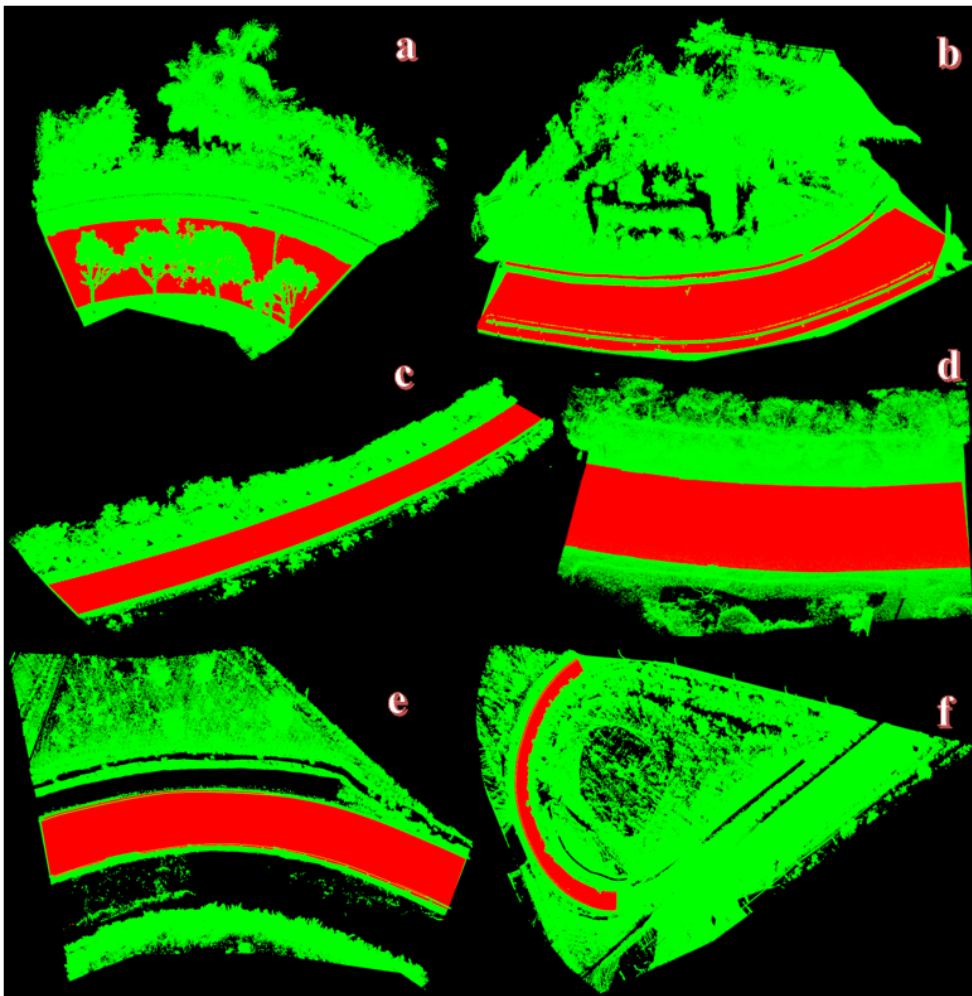
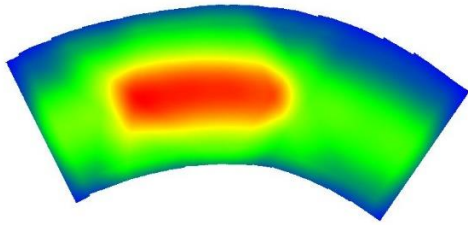


Figure 4.4 Road surface extraction results obtained using six test datasets.

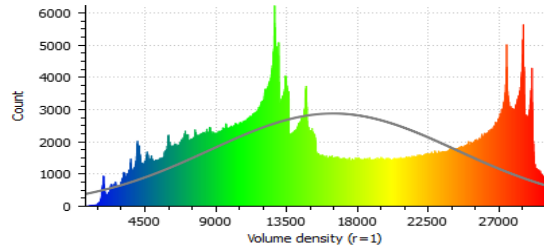
As shown in Figure 4.5, point density distributions of the extracted road surface points were implemented in the six test datasets. The average point density of six datasets are 16469.15,

5126.98, 2813.40, 3104.08, 2881.12, and 2951.90 points/m<sup>3</sup> respectively. It is worth noting that the average point density increases after removing off-pavement points for each dataset.

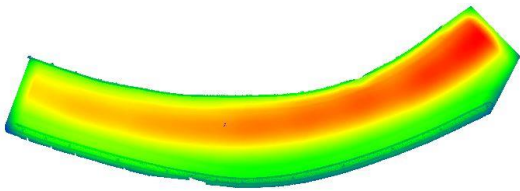


(a) Road surface of Dataset 1

Gauss: mean = 16469.148438 / std.dev. = 7823.298828 [1929 classes]

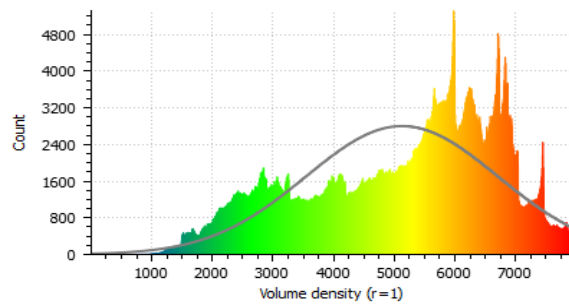


(a-1) Point density distribution chart of road surface 1

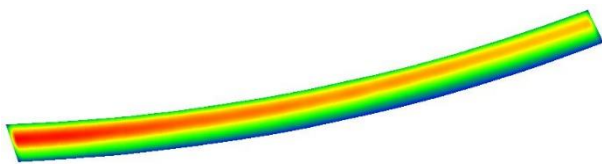


(b) Road surface of Dataset 2

Gauss: mean = 5126.982910 / std.dev. = 1584.883545 [1398 classes]



(b-1) Point density distribution chart of road surface 2

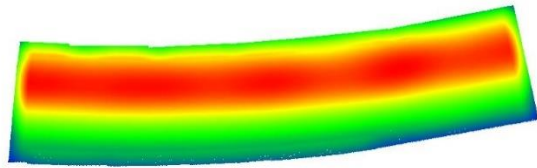


(c) Road surface of Dataset 3

Gauss: mean = 2813.395508 / std.dev. = 889.119873 [1810 classes]

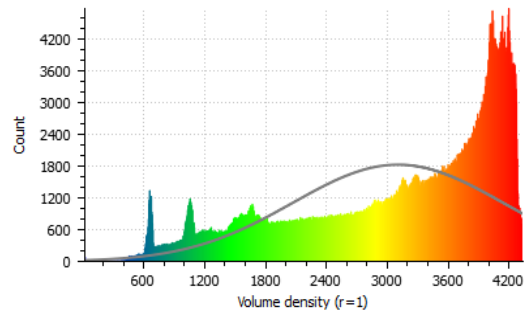


(c-1) Point density distribution chart of road surface 3

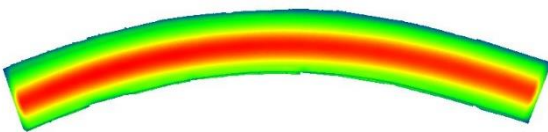


(d) Road surface of Dataset 4

Gauss: mean = 3104.084717 / std.dev. = 1034.135620 [1097 classes]

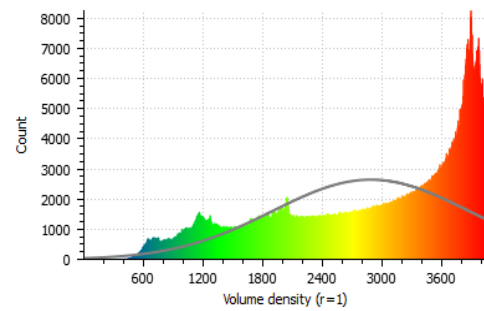


(d-1) Point density distribution chart of road surface 4

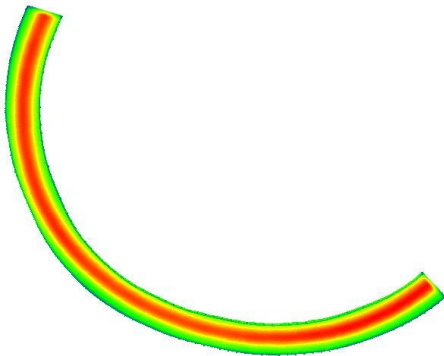


(e) Road surface of Dataset 5

Gauss: mean = 2881.111816 / std.dev. = 985.446289 [1605 classes]

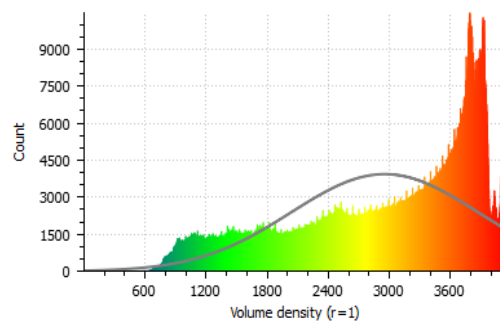


(e-1) Point density distribution chart of road surface 5



(f) Road surface of Dataset 6

Gauss: mean = 2951.901611 / std.dev. = 917.591797 [2172 classes]



(f-1) Point density distribution chart of road surface 6

Figure 4.5 Point density distributions of the extracted road surfaces.

#### 4.2.2 Geo-referenced Intensity Image Generation

Based on the extracted road surface points, the IDW interpolation algorithm was afterward employed to generate GRF intensity imagery with different resolutions. Table 4.3

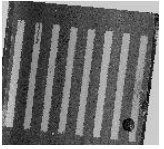
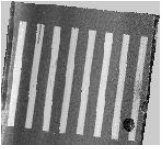
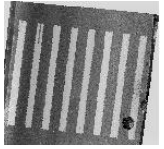
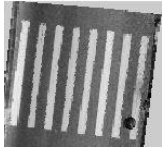
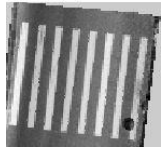
indicates fine image resolutions can increase the data volume and decrease computational efficiency for a MLS test dataset, accordingly.

Table 4.3 Resolution of Geo-referenced intensity image and its data size.

Resolution (cm)	2	4	6	8	10
Image size (MB)	19.2	3.22	1.42	0.83	0.53

A group of experiments keep the grid size ranging between 2 cm and 10 cm, while the generated GRF intensity imagery become blurred, as shown in Table 4.4. The smallest road markings (i.e., broken lines with width of 15 cm) can be preserved and presented in the generated intensity imagery when setting the image resolution to be 4 cm. Thus, the extracted road surface points were rastered into intensity imagery with the resolution of 4 cm by using the IDW interpolation method.

Table 4.4 Geo-referenced intensity images with different resolutions.

Resolution (cm)	2	4	6	8	10
Zebra Crossing (7.5 * 6.0 m <sup>2</sup> )					

Futhremore, Figure 4.6 presents the intensity imagery generated by the IDW interpolation with the image resolution of 4 cm. Additionally, the road markings indicate higher illumination than pavements with respect to intensity information.

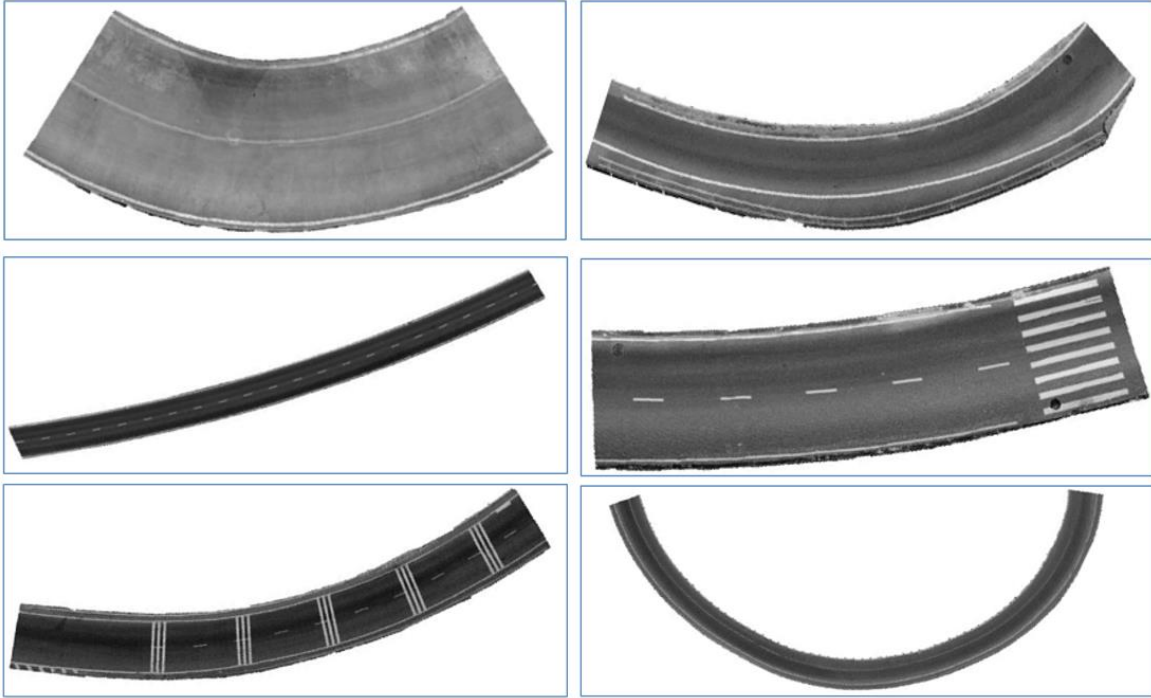


Figure 4.6 Geo-referenced intensity image generated by IDW interpolation.

### 4.2.3 Road Marking Extraction

Several parameters involved in the process of road marking extraction, including the numbers of bins ( $B_n$ ), the intensity values of road markings ( $I_i$ ), and the distances between vehicle trajectory to the road markings ( $D_i$ ), are listed in Table 4.5. Among these parameters,  $B_n$  is determined by the point density.  $I_i$  and  $D_i$  are used to identify and extract road markings from the generated intensity imagery. Since the study area in this thesis mainly concentrate on the horizontally curved road sections, each generated intensity imagery includes two or three types of road markings, as summarized in Table 4.6.

Table 4.5. Parameters for road marking extraction algorithms.

Parameters	Definition	Pre-defined threshold
$B_n$	The number of bins	Determined by the point density
$I_i$	The intensity values of road markings	To be determined
$D_i$	The distances between vehicle trajectory to the road markings	To be determined

Table 4.6. Road marking types in geo-referenced intensity images.

Intensity imagery name	Road marking types
Road_surface_1	Solid edge lines and centreline
Road_surface_2	Solid edge lines
Road_surface_3	Solid edge lines and broken lane line markings
Road_surface_4	Solid edge lines, broken lane line markings and zebra crossing markings
Road_surface_5	Solid edge lines and hatch markings
Road_surface_6	Solid edge lines

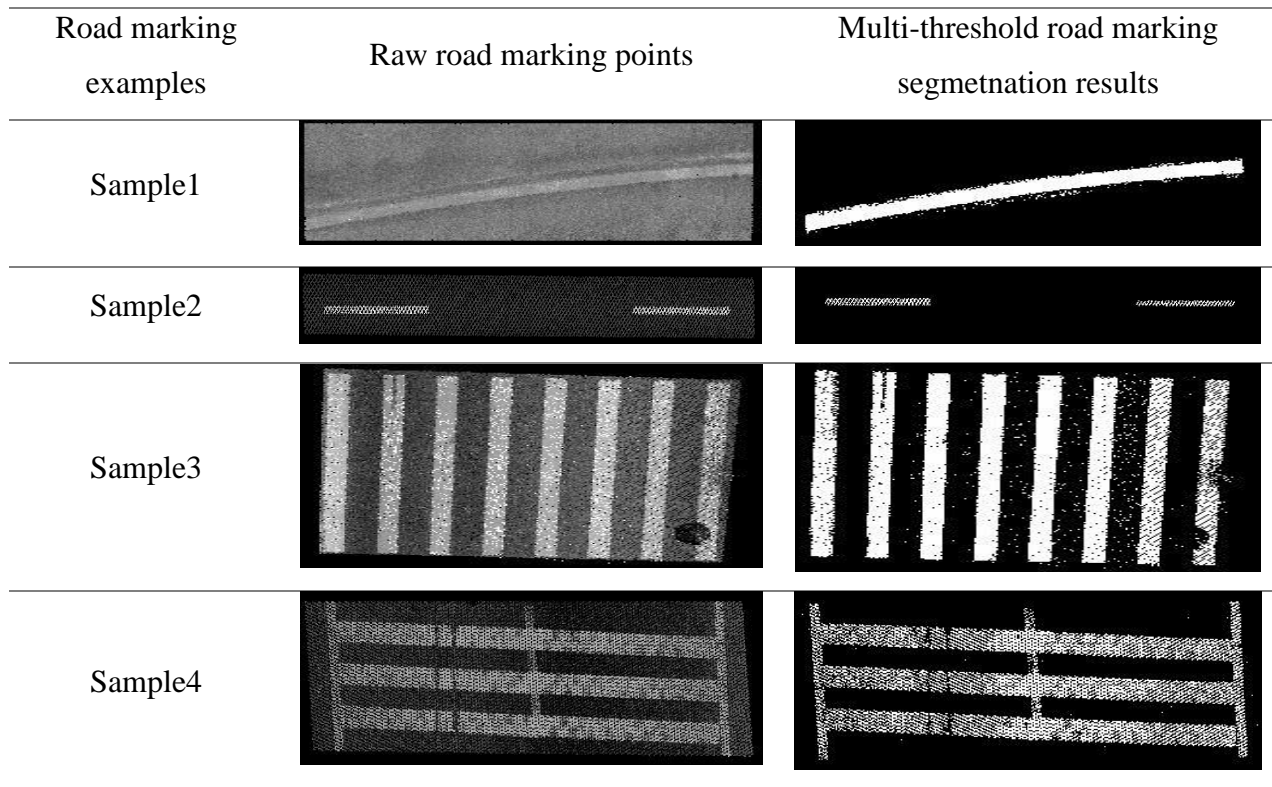


Figure 4.7 Four types of road markings and their extraction results.

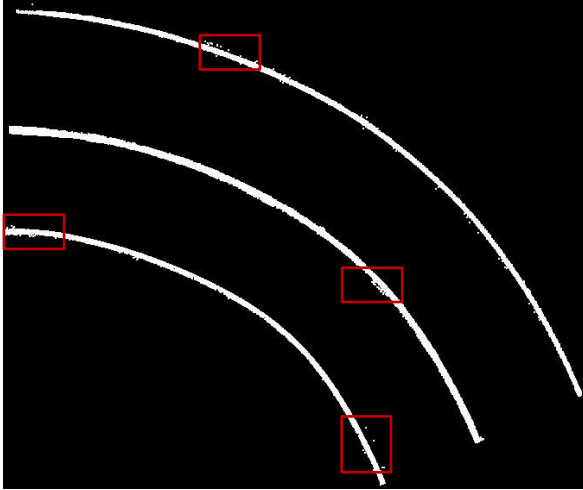
A series of experiments were carried out to verify the performance of the proposed multi-threshold road marking extraction algorithms while keeping the resolution of 4 cm for all

generated intensity imagery. Moreover, four types of road markings are presented in Figure 4.7. All results in the second column indicate that all road markings, including solid edge lines, broken centrelines, hatch markings and zebra crossing markings, can be correctly detected and completely extracted. Furthermore, these intensity imagery can generate their own  $B_n$  thresholds using Otsu's method, and the other two parameters  $I_i$  and  $D_i$  can be determined by visual interpretation and quantitative measurement based on the road materials and dimensions. As shown in Figure 4.7, visual inspection indicates most road markings can be detected and extracted correctly using the proposed multi-threshold extraction algorithms. However, discrete noises still can be identified, which has influence on the recall and precision of extracted road markings.

#### **4.2.4 Noise Removal**

K-nearest neighbourhoods should be identified by first in order to implement noise removal using the SOR filter. Based on the point densities of raw test datasets, the value of parameter  $k$  can be determined, where  $k$  denotes the number of points should be searched around a certain point. In this study, a series of experiments keeping  $k = 20$  were conducted according to the point density. As shown in Figures 4.8 (a) – (f) the extracted road markings of the six test datasets are presented, while their corresponding noise removal results are shown in Figures 4.8 (a-1) – (f-1). Consequently, discrete noises (e.g., red rectangles in each figure) are completely eliminated. However, due to the inevitable damage of painted markings caused by moving heavy-duty trucks and weather conditions (e.g., salt-fog corrosion), there exist small gaps in the extracted road markings, as illustrated in blue rectangles in Figures 4.8 (c), (c-1), (d) and (d-1). Thus, these results demonstrate that discrete noises are successfully removed and the completeness of extracted road markings can be preserved after implementing the SOR filter.

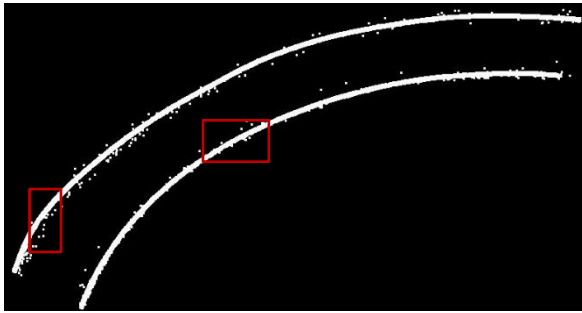




(a) Extracted road markings of Dataset 1



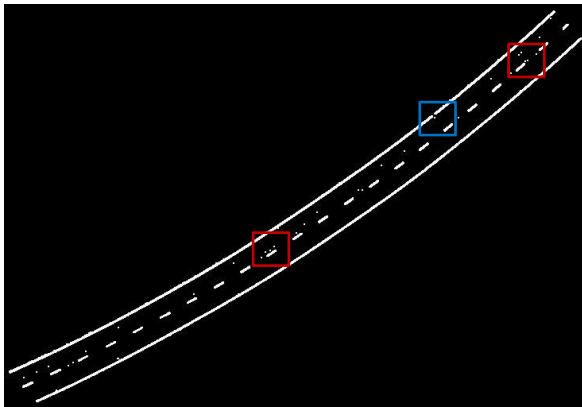
(a-1) Refined road markings of Dataset 1



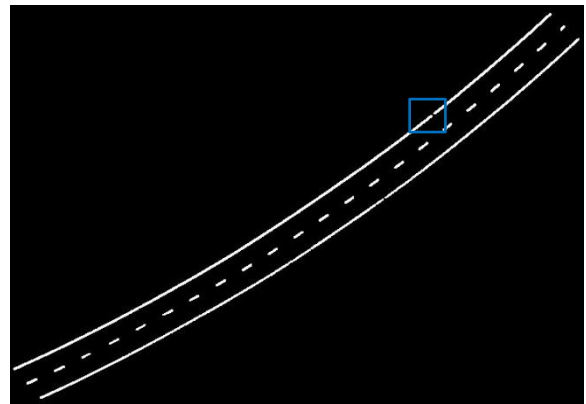
(b) Extracted road markings of Dataset 2



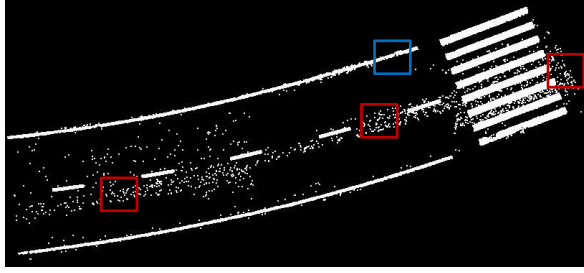
(b-1) Refined road markings of Dataset 2



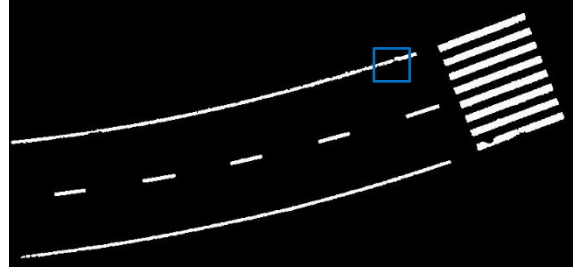
(c) Extracted road markings of Dataset 3



(c-1) Refined road markings of Dataset 3



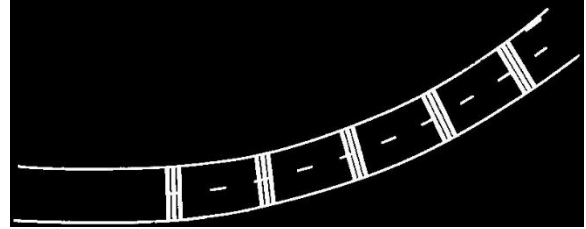
(d) Extracted road markings of Dataset 4



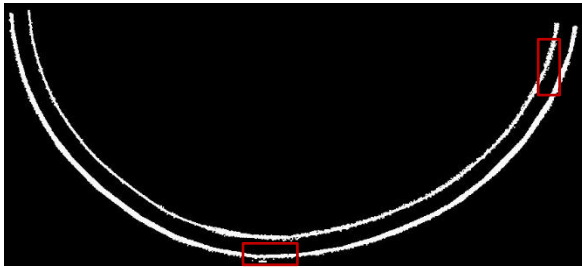
(d-1) Refined road markings of Dataset 4



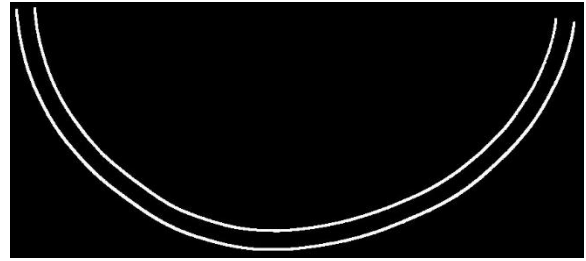
(e) Extracted road markings of Dataset 5



(e-1) Refined road markings of Dataset 5



(f) Extracted road markings of Dataset 6



(f-1) Refined road markings of Dataset 6

Figure 4.8 Results of noise-removed road markings.

After eliminating the noises, most of road markings are completely extracted from the raw datasets except two incomplete road markings (see blue rectangles in Figures 4.8 (c), (c-1), (d) and (d-1)). The road marking decay, the losses of road marking reflectance, the lack of sufficient laser points and the value of  $k$  that used to conduct the SOR filter can account for these errors.

#### 4.2.5 Road Marking Clustering

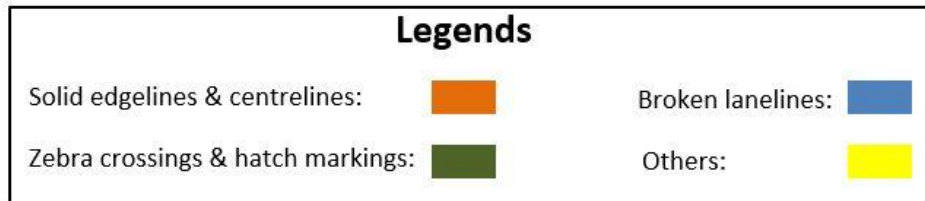
After extracting road markings and implementing noises removal, there are still no distinct topological relationships among the remaining MLS point clouds. Based on the Gaussian

point density distributions and the resolution of the generated noise-removed points, a series of experiments using parameters  $d_e$  and  $w_c$  were implemented for classification using the conditional Euclidean clustering algorithm. The details of these two parameters are indicated in Table 4.7.

Table 4.7 Parameters for the conditional Euclidean clustering method.

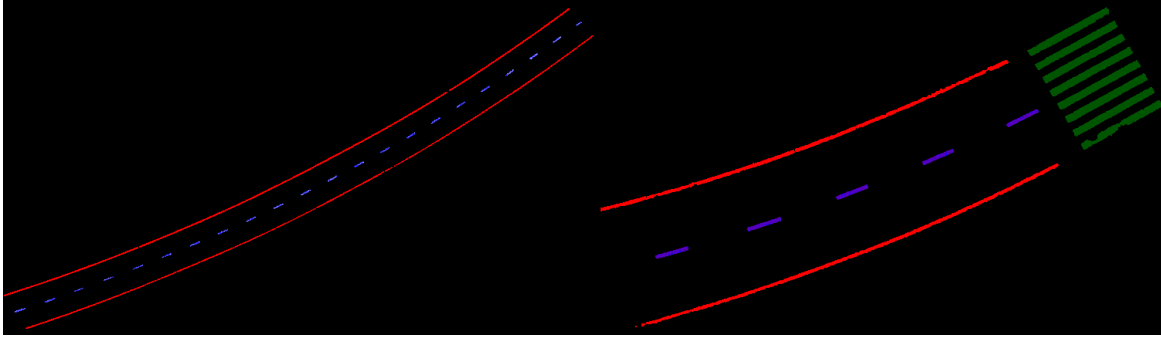
Parameters	Definition	Pre-defined threshold
$d_e$	The range of scanning distances	To be determined
$w_c$	The width of a road marking	Based on a prior knowledge

Figures 4.9 (a), (b), (c), (d), (e) and (f) present the road marking clustering results after implementing the conditional Euclidean cluster algorithm. As can be perceived, majority of road markings (e.g., centrelines, edge lines and zebra crossing road markings) can be successfully clustered by adjusting both thresholds of  $d_e$  and  $w_c$ . Moreover, disordered points in the noise-removed road marking datasets have topological relationships and the generated clusters are regarded as semantic objects.



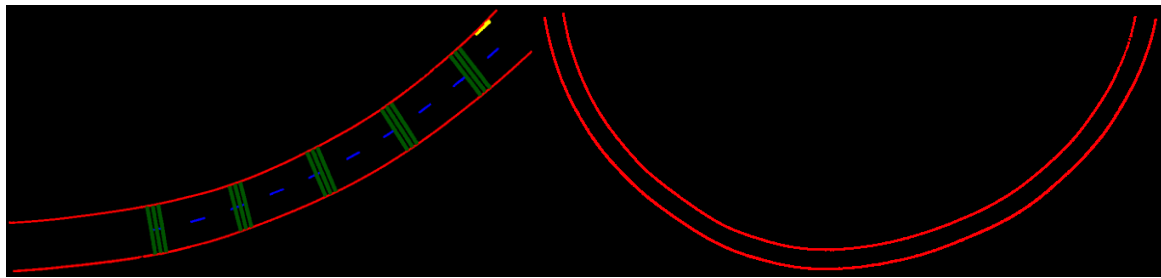
(a) Clustered road markings of Dataset 1

(b) Clustered road markings of Dataset 2



(c) Clustered road markings of Dataset 3

(d) Clustered road markings of Dataset 4



(e) Clustered road markings of Dataset 5

(f) Clustered road markings of Dataset 6

Figure 4.9 Road marking clustering results: (a), (b), (c), (d), (e) and (f) are road marking clustering and segmentation results for each dataset, respectively.

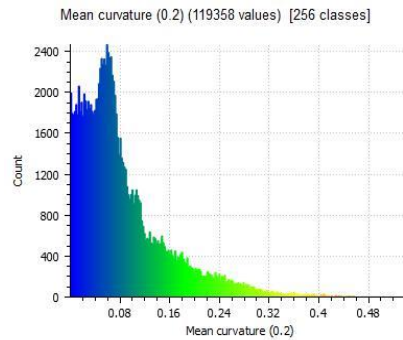
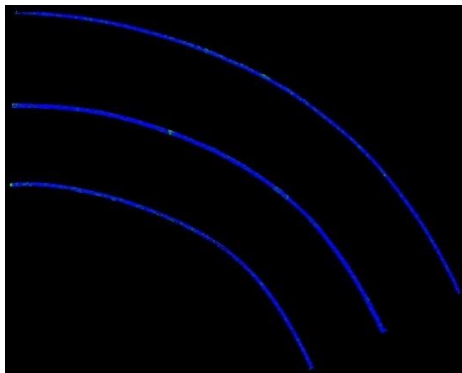
#### 4.2.6 Curve Fitting

Since disordered road marking points are clustered into different semantic objects, the topological relationships among clustered edge line or centreline points are capable of implementing curve fitting. The results obtained by the nonlinear least-squares curve fitting algorithm are determined by the two parameters: the degree of the polynomial  $k$  and the corresponding coefficients  $a_k$ . These two parameters are detailed in Table 4.8.

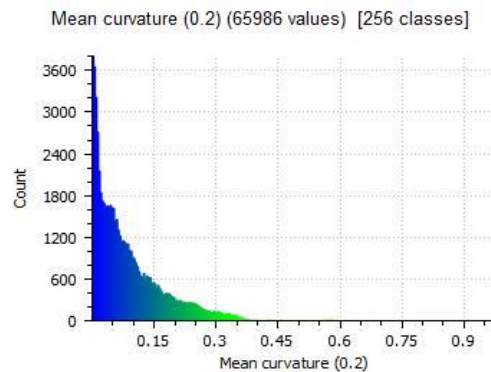
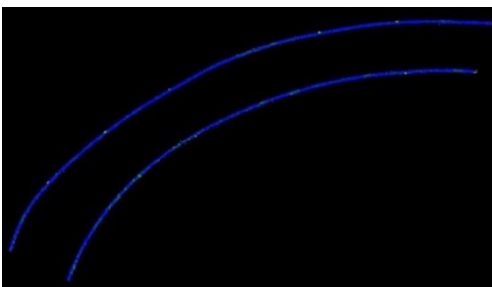
Table 4.8. Parameters for the nonlinear least-squares curve-fitting algorithm.

Parameters	Definition	Pre-defined threshold
$k$	The degree of the generated polynomial	To be determined
$a_k$	The coefficients of the generated $k$ -degree polynomial	To be determined

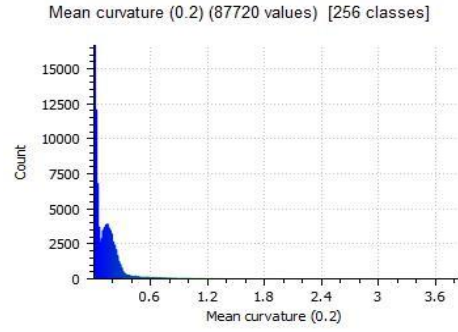
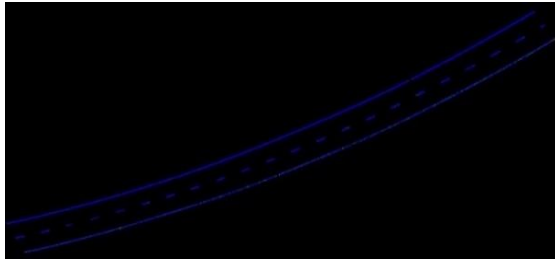
Based on the road design and construction standards and curvature analysis of the generated road edge lines, centrelines and lane lines, a collection of experiments were performed to examine the sensitivity and flexibility of parameters used at the stage of curve fitting. Figures 4.10 (a) – (f) show the noise-removed road marking extraction results of six test datasets, and Figures 4.10 (a-1) – (f-1) indicate their corresponding mean curvature distributions with kernel size of 0.2 m. Based on Figure 4.10, it can be concluded that the mean curvature of a horizontal curve is smaller than 0.15. Due to the existence of non-curved road markings (e.g., hatch markings) and the discontinuity of centrelines (see Figure 4.10 (c)), the mean curvature of each test dataset is overestimated in the final result. According to road design and construction standards, majority of horizontal curves are designed as circular curves. Therefore, these experiments keep  $k = 2$  (the second-degree polynomial) for all the datasets.



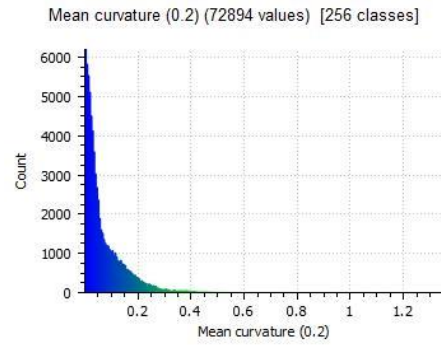
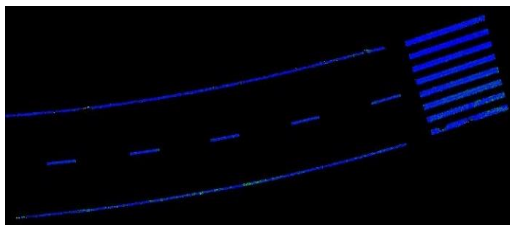
(a) Noise-removed road markings of Dataset 1 (a-1) Corresponding mean curvature distribution



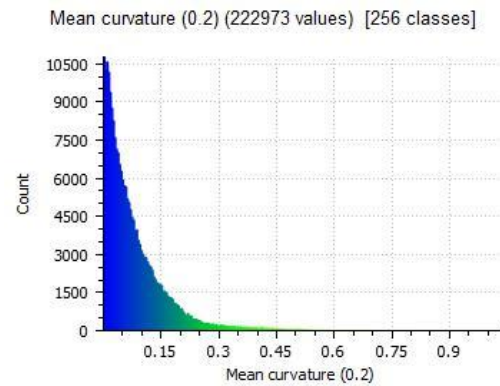
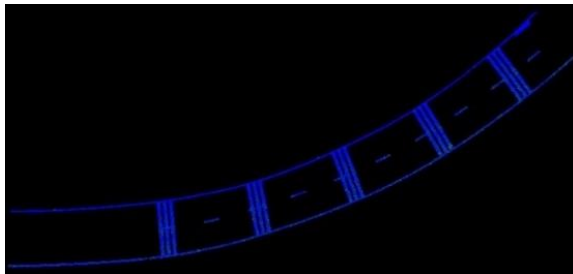
(b) Noise-removed road markings of Dataset 2 (b-1) Corresponding mean curvature distribution



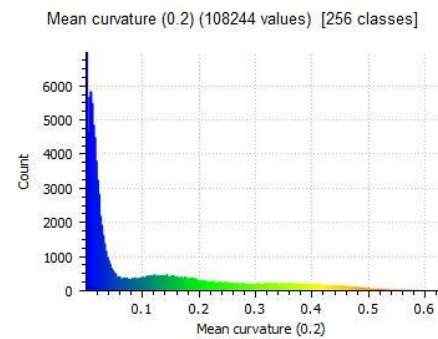
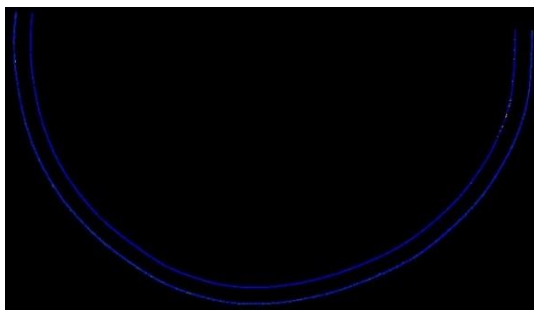
(c) Noise-removed road markings of Dataset 3 (c-1) Corresponding mean curvature distribution



(d) Noise-removed road markings of Dataset 4 (d-1) Corresponding mean curvature distribution



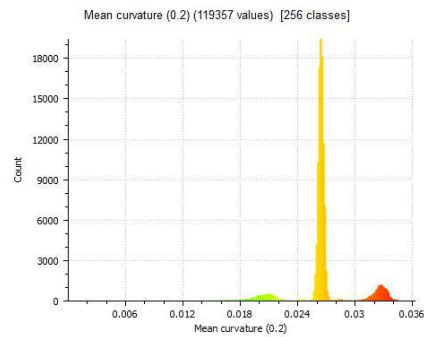
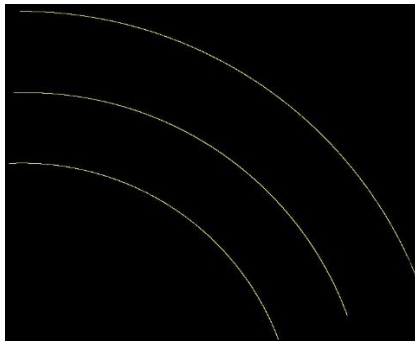
(e) Noise-removed road markings of Dataset 5 (e-1) Corresponding mean curvature distribution



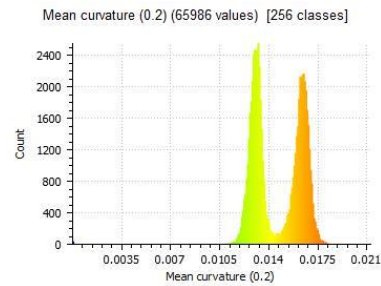
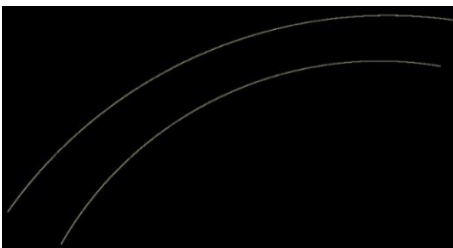
(f) Noise-removed road markings of Dataset 6 (f-1) Corresponding mean curvature distribution

Figure 4.10 Mean curvature distributions of road marking results.

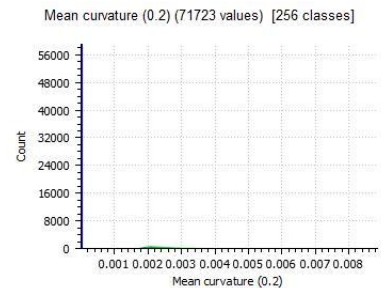
As a result, Figures 4.11 (a) – (f) present planar B-spline curves with coordinate information generated by implementing the nonlinear least-squares curve fitting method, and Figures 4.11 (a-1) – (f-1) show their corresponding mean curvature distributions with kernel size of 0.2 m. As can be seen, majority of best-fitting functions of horizontal curves (e.g., edge lines and lane lines) can be elaborately determined. Additionally, compared with Gaussian mean curvature values of the noise-removed road marking extraction results, this value of each dataset becomes smaller after implementing curve fitting. Furthermore, non-curved road markings (e.g., zebra crossings) can be successfully removed by using the nonlinear least-squares curve fitting algorithm in order to improve computational efficiency at the stage of driving line generation.



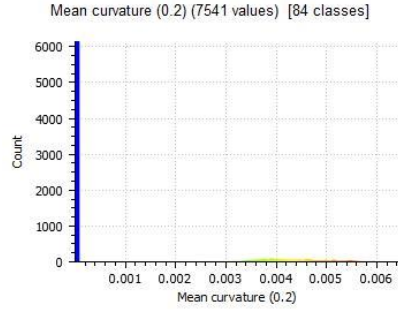
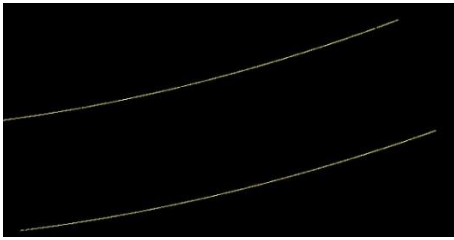
(a) Curve-fitting results of Dataset 1 (a-1) Mean curvature distribution of curve-fitting 1



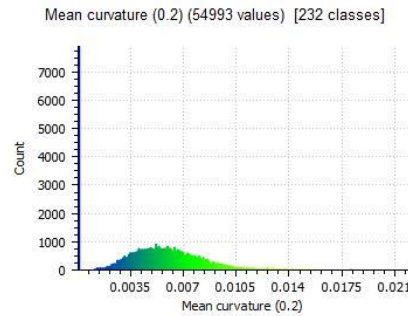
(b) Curve-fitting results of Dataset 2 (b-1) Mean curvature distribution of curve-fitting 2



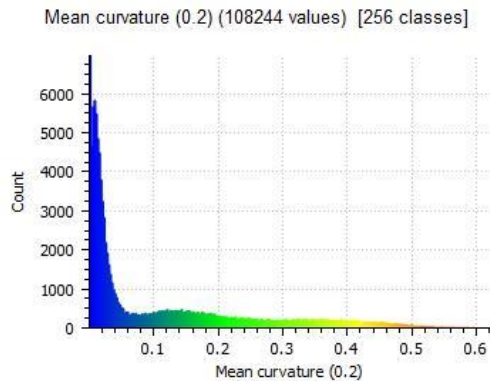
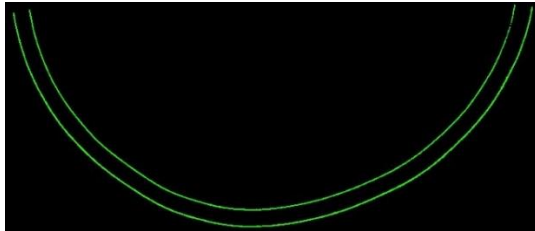
(c) Curve-fitting results of Dataset 3 (c-1) Mean curvature distribution of curve-fitting 3



(d) Curve-fitting results of Dataset 4 (d-1) Mean curvature distribution of curve-fitting 4



(e) Curve-fitting results of Dataset 5 (e-1) Mean curvature distribution of curve-fitting 5



(f) Curve-fitting results of Dataset 6 (f-1) Mean curvature distribution of curve-fitting 6

Figure 4.11 Mean curvature distributions of curve-fitting results.

### 4.2.7 Driving Line Generation

In this section, driving lines at horizontally curved road sections can be generated according to the calculated best-fitting functions of curved road markings. Based on a prior knowledge and the road design and construction restrictions, most of curved road markings, including solid edge lines, centrelines and broken lane markings, are parallel to each other in



the XOY-plane to guarantee safety for road users. Therefore, the results can be determined by analyzing their corresponding functions of the generated curve-fittings. Moreover, parameter  $d_s$  used in this section is shown in Table 4.9, which indicates the distances from edge lines or centrelines to the driving lines to be generated. Since majorities of the generated curve-fitting functions belong to circular arc curve and elliptic arc curve functions, related mathematical functions are therefore used to calculate the coordinate information for the final driving lines. Additionally, for the purpose of reducing the time complexity and improve the precision of this method, a Quick Sort algorithm is applied to reorganize the entire point clouds within the generated curve-fitting point clouds.

Table 4.9 Parameters used in driving line generation algorithms.

Parameter	Definition	Pre-definied threshold
$d_s$	The distances from the edge lines, lane lines or centrelines to the driving lines	Based on road design regulations

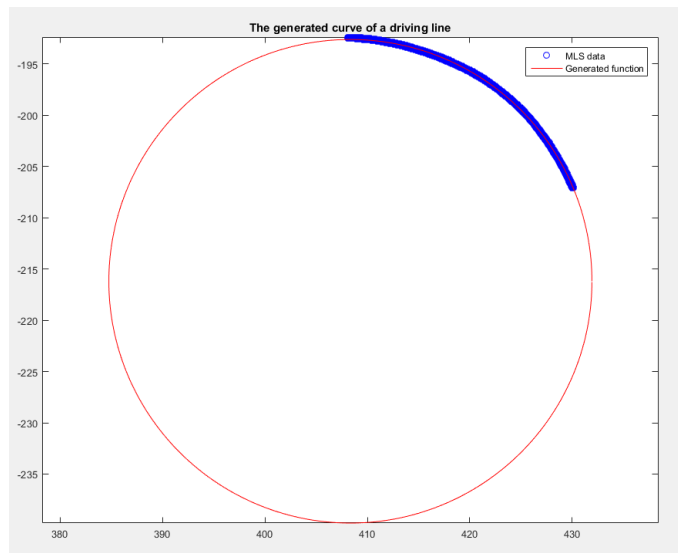


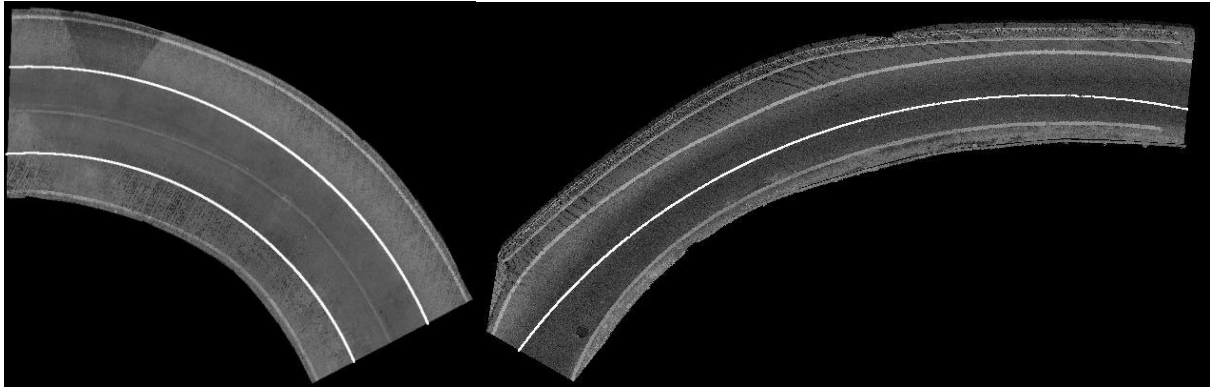
Figure 4.12 The generated circular curve of a driving line.

Accordingly, Figure 4.12 presents the generated best-fitting curve of a driving line for test Dataset 1. As can be perceived, all points pertaining to this driving line are located on a part of a circular curve, which demonstrates this circular curve is capable to model and calculate a driving line effectively. Thus, the corresponding mathematical function of this generated driving line in the XOY-plane can be determined as follows:

$$x^2 + y^2 - 816.68x - 432.40y - 213191.38 = 0 \quad (4.1)$$

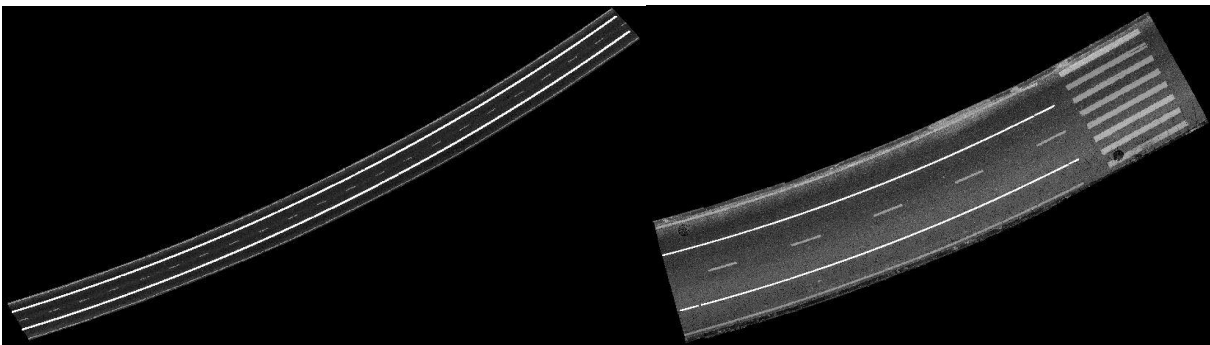
where  $x$  and  $y$  indicate the relative coordinates of a point in XOY-plane. Consequently, the coordinates of all 3D MLS points belonging to a driving line can be determined according to the Eq. (4.1).

Furthermore, the driving line generation results are presented in Figure 4.13. The final results demonstrate that all driving lines at horizontal curves can be generated successfully on the six test datasets by using the proposed algorithms. As can be seen, most of generated driving lines are located at central positions between road lane lines and edge lines (or centrelines), which provides the best-matching driving lines that meet the requirements of 3D high-definition roadmaps and guarantee traffic safety for autonomous vehicles. However, these algorithms are still influenced by disconnectivity of edge lines or centrelines. As shown in Figure 4.13 (d), two generated driving lines between road edge lines and centrelines interrupt due to the existence of zebra crossing marking and discontinuities of edge lines and centrelines.



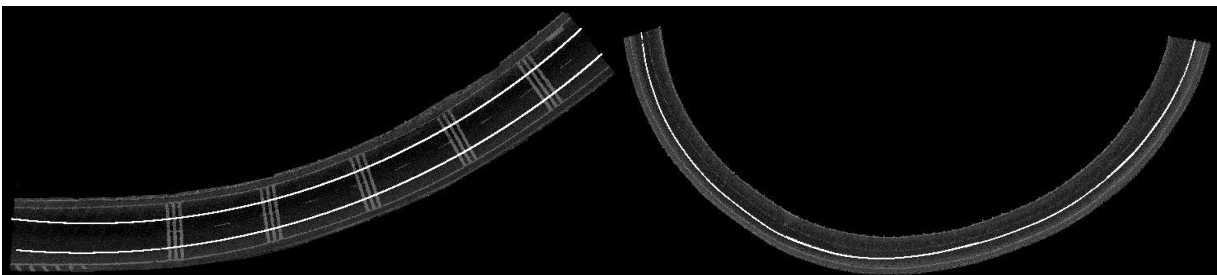
(a) Generated driving lines of Dataset 1

(b) Generated driving line of Dataset 2



(c) Generated driving lines of Dataset 3

(d) Generated driving lines of Dataset 4



(e) Generated driving lines of Dataset 5

(f) Generated driving line of Dataset 6

Figure 4.13 Driving line generation results.

Moreover, these generated driving lines not only provide accurate navigation solutions for autonomous vehicles at horizontally curved road sections but also offer detailed curve information related to urban road design and traffic safety. Therefore, according to the generated mathematical functions of these driving lines, the corresponding elements including radius, length, and degree of a curve, can be calculated in order to improve the urban road

alignments. As shown in Table 4.10, relevant elements of a generated circular curve are determined based on the generated mathematical function of a driving line. Compared with the road design and construction regulations defined by local governments (see Table 4.11), it is worth noting that all elements calculated from the generated driving line can meet the requirements for traffic safety at horizontal curves. For example, radius of the curve described in Table 4.10 approximates 462 ft (i.e., 140 m), which indicates the driving speed at this horizontal curve should be no more than 30 km/h to ensure the traffic safety for all road users. Accordingly, based on the final report of Xiamen Urban Road Safety Regulations submitted to the Xiamen Transportation Bureau in 2006, the speed limit of this road is 30 km/h, it is concluded that the generated driving line meet the requirements of urban road design standards.

Table 4.10 Elements of a generated driving line.

Symbol	Definition	Units	Values
PC	Start of horizontal curve	-	-
PT	End of horizontal curve	-	-
D	Degree of curvature	degrees per 100 ft of centreline	12.4
$\Delta$	Central angle of curve, PC to PT	degrees	10.49
R	Radius of curve	ft	462.06
L	Length of curve	ft	84.65
T	Tangent length	ft	42.42
M	Middle ordinate	ft	5.94
LC	Length of long chord, from PC to PT	ft	84.48
E	External distance	ft	5.83

Table 4.11 Code for Design of Urban Road Engineering, China (Version CJJ 37-2012, 2012).

Driving speed (km/h)	Minimum radius of a circular curve (m)	Minimum length of a circular curve (m)	Stopping sight distance (m)
30	85	25	30
40	150	35	40
50	200	40	60
60	300	50	70
80	400	70	110

#### 4.2.8 Overall Performance Assessment

Table 4.12 Computation efficiency of all proposed algorithms.

Test datasets	1	2	3	4	5	6
Size (MB)	213	127	184	67	118	601
The number of points	6,568,656	3,928,845	5,683,607	2,064,205	3,661,745	18,561,253
Road surface extraction (s)	41.25	36.03	40.62	13.32	34.58	82.62
Road marking extraction (s)	12.44	15.93	22.32	9.05	21.24	47.50
Noise removal (s)	1.62	0.76	1.54	1.49	4.02	3.30
Clustering (s)	14.84	11.16	6.03	19.52	27.43	31.79
Driving line generation (s)	0.03	0.04	0.02	0.01	0.03	0.05
Total time (s)	70.18	63.92	70.53	43.39	87.30	165.26

To summarize, Table 4.12 shows the computational efficiency of all proposed post-processing algorithms in this thesis. The operation time of each algorithm has been calculated for six test datasets. Additionally, the workstation used in this study is a Dell Alienware x51 desktop with an Intel Quad CORE i5-6400 CPU, and an 8 GB RAM. The consuming time indicates the performances and efficiencies of road surface extraction, road marking extraction, image denoising, road marking clustering and driving line generation methods are high. Furthermore, as

mentioned in Chapter 1, the main objective in this study is to develop driving line generation algorithms at horizontally curved road sections. Thus, both the image denoising algorithms and road marking clustering algorithms utilized directly the commercial PCL programming packages, and road surface extraction algorithms took advantage of Guan's (2014) research. Due to processing the entire point clouds block by block, the larger curvature the horizontal curve has, the more data blocks and more computing time will be. Moreover, all MLS points belonging to road markings should be searched in the process of the conditional Euclidean clustering algorithm which is time-consuming. Therefore, the overall performance of the proposed post-processing algorithms can be further improved by optimizing road surface extraction, road marking extraction and clustering at the stage of driving line generation.

### 4.3 Validation Results

#### 4.3.1 Accuracy Assessment of Road Marking Extraction

Figure 4.14 shows the extracted road markings after noise removal.

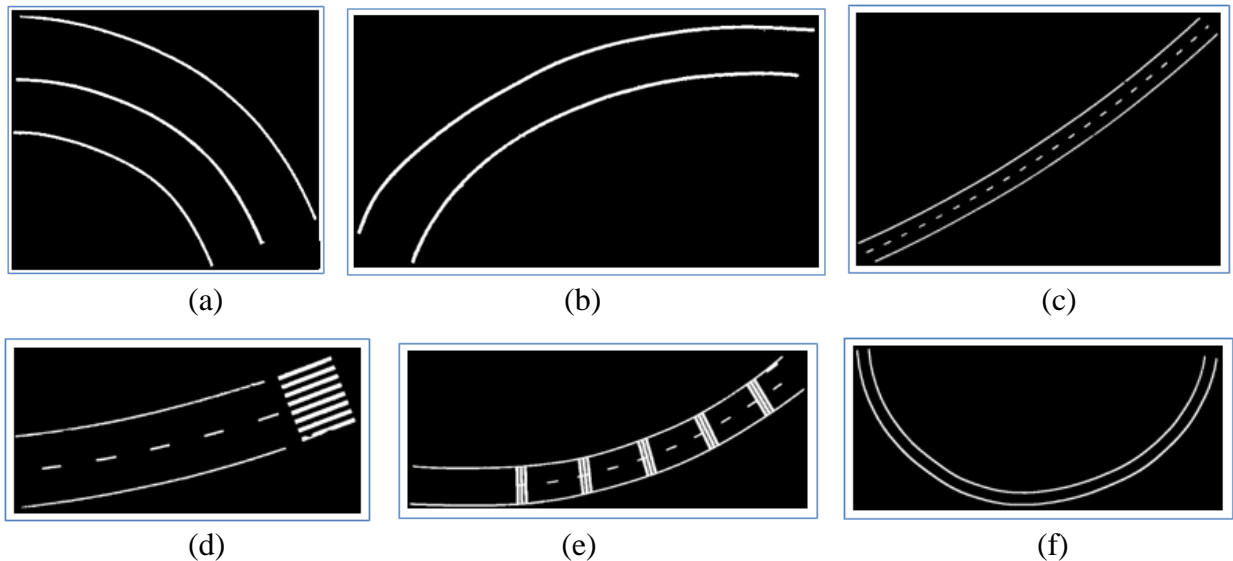
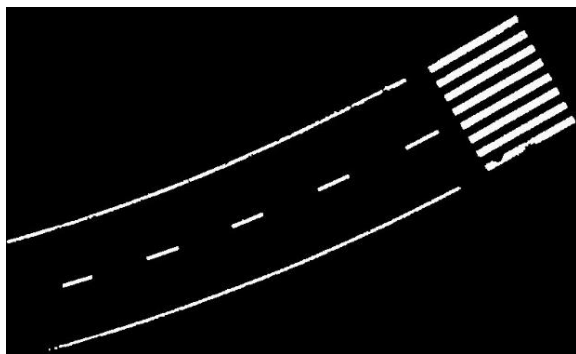


Figure 4.14 Extracted road marking after noise removal from each of the six test datasets: (a) – (f) show the final extraction results from Dataset I to Dataset VI.

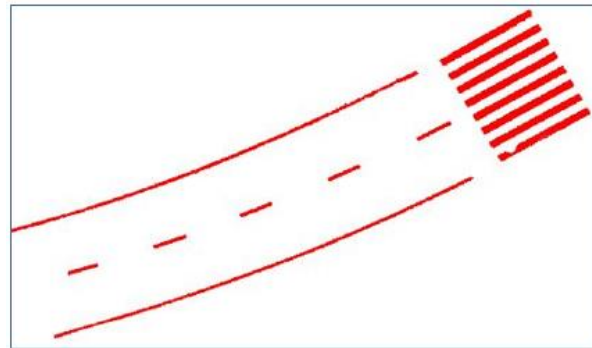
Table 4.13 Accuracy assesement of road marking extraction.

Performance (%) \ Dataset	1	2	3	4	5	6	Average
Recall	90.06	93.73	90.42	88.02	92.71	90.42	90.89
Precision	92.53	95.04	93.05	89.59	94.97	93.05	93.04
F1-score	91.28	94.38	91.72	88.80	93.83	91.72	91.95

As illustrated in Table 4.13, the quantitative assessments were conducted based on the recall, precision and F1-score. As a result, the proposed road marking extraction and noise removal algorithms are capable of obtaining 90.89% in recall, 93.04% in precision and 91.95% in F1-score, respectively. The value of precision is larger than that of recall for each sample, which demonstrates that certain road marking pixels were misclassified as road surfaces. Additionally, the size of manually labelled reference data are larger than the road markings due to the decay of them. Thus, the overall performance of the proposed road marking extraction algorithms is underestimated in the final results. Figure 4.15 (a) shows the extracted road markings after noise removal, and Figure 4.15 (b) indicates the manually labelled reference data to be used for accuracy assessment.



(a)



(b)

Figure 4.15 Extracted road markings and the reference data: (a) the proposed method; (b) the reference data by manually labelled.

### 4.3.2 Comparative Study of Road Marking Extraction

Furthermore, a comparative study was carried out concentrating on the extracted road marking results by using the proposed algorithms and other methods, i.e. Chen et al. (2009) and Yu et al. (2015). MLS point clouds were used directly in the process of road marking extraction in both Chen's and Yu's methods. Figures 4.16 to 4.18 present the road markings extracted using the three methods. Consequently, Chen's method mainly focuses on the lane marking extraction along the moving direction of the vehicle, resulting in limitations at the stage of complex and semantic road marking extraction (e.g., arrows, words and curved road markings). Meanwhile, based on deep learning and PCA methods, Yu's approach can be applied in the extraction of any types of road markings but it has limitations in the process of curved road marking extraction and also it requires rich prior knowledge.

The overall performance of the proposed method and other three methods are evaluated based on the quantitative assessment (i.e., recall, precision and F1-score). As shown in Table 4.14, Zhang's (2009) method can achieve an average of 76.91% in recall, 91.27% in precision and 83.42% in F1-score, respectively; Yu's (2015) method can achieve an average of 81.15% in recall, 91.17% in precision and 85.81% in F1-score, respectively; while the proposed method in this thesis can achieve an average of 90.26% in recall, 92.36% in precision and 91.30% in F1-score, respectively. Table 4.14 indicates that the proposed method can achieve a better performance than both Chen's and Yu's methods in terms of both recall and precision. Moreover, it demonstrates the revised multi-thresholds extraction method in this thesis can effectively extract curved road markings (e.g., centrelines, edge lines and lane lines) at horizontally curved road sections.



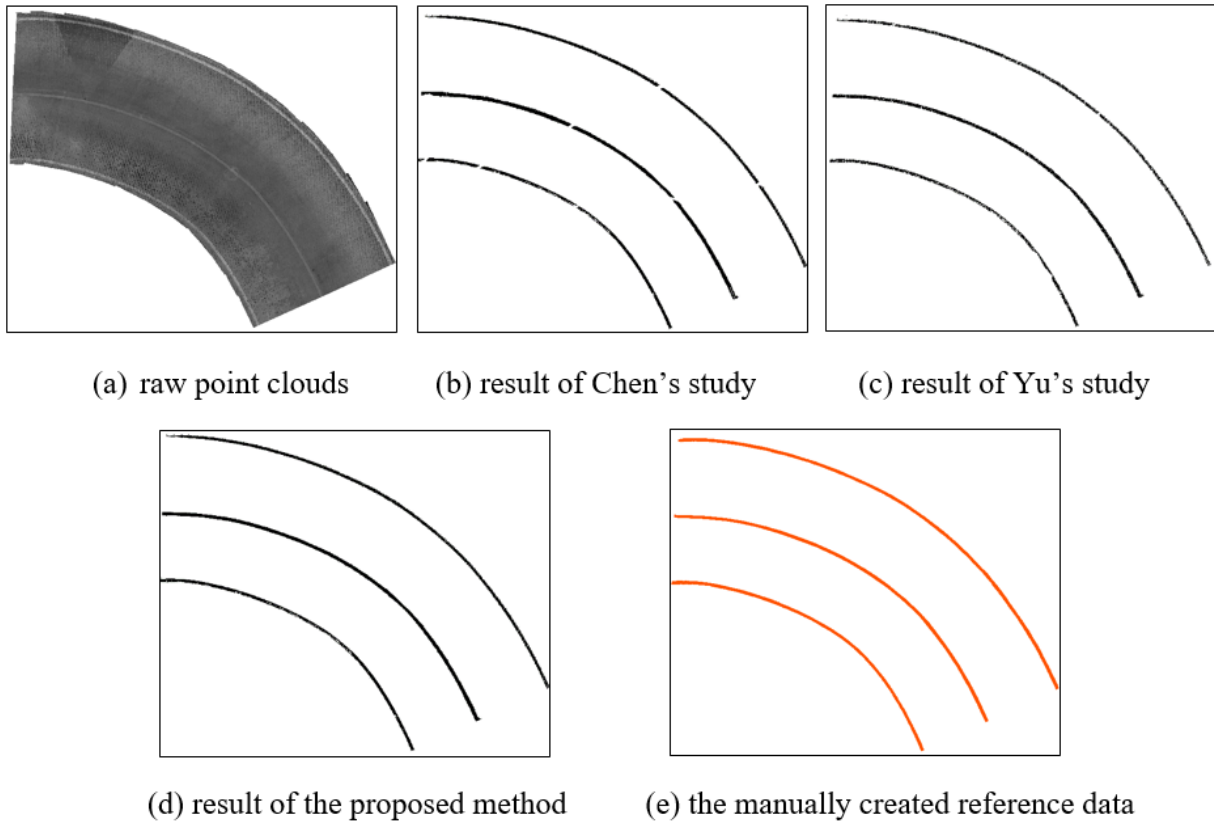
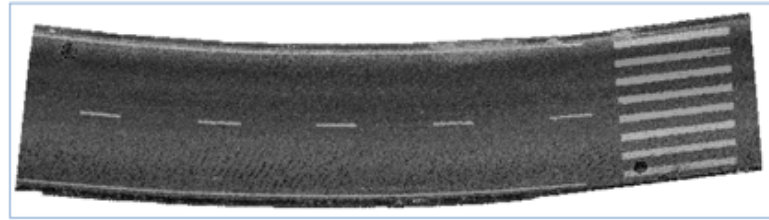


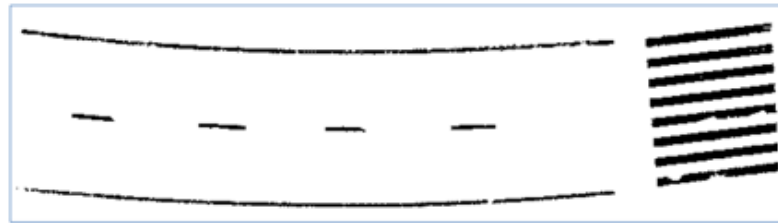
Figure 4.16 Road marking extraction results using Dataset I: (a) raw pavement MLS points; (b) result of Chen's study; (c) result of Yu's study; (d) result of the proposed method; and (e) the manually labelled reference data.

Table 4.14 Comparison of the three methods in quantitative evaluation.

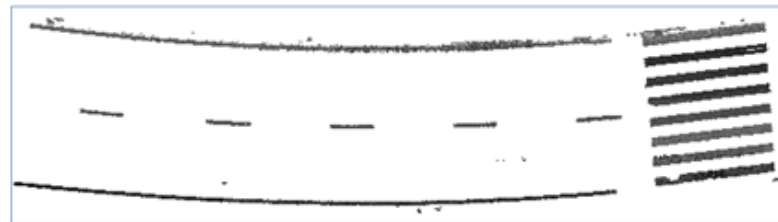
Test Datasets	I			IV			V		
	Chen et al., 2009	Yu et al., 2015	In this thesis	Chen et al., 2009	Yu et al., 2015	In this thesis	Chen et al., 2009	Yu et al., 2015	In this thesis
Recall (%)	72.95	81.83	90.06	74.95	76.27	88.02	82.84	85.34	92.71
Precision (%)	90.89	90.47	92.53	92.02	91.88	89.59	90.95	91.17	94.97
F1-score (%)	80.94	85.93	91.28	82.61	83.35	88.80	86.71	88.16	93.83



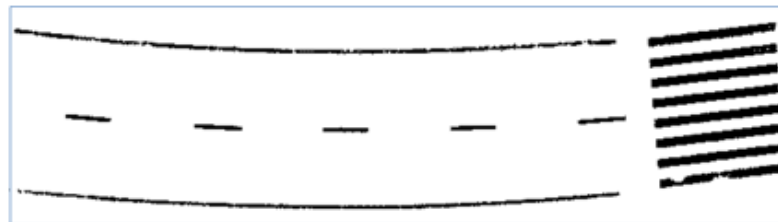
(a) raw point clouds



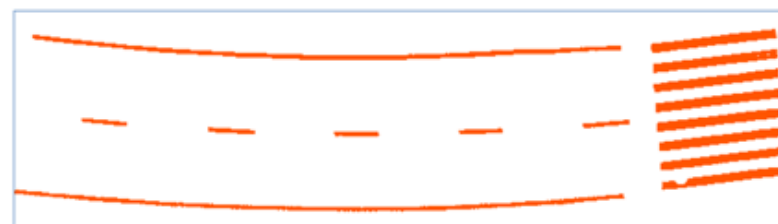
(b) result of Chen's method



(c) result of Yu's method

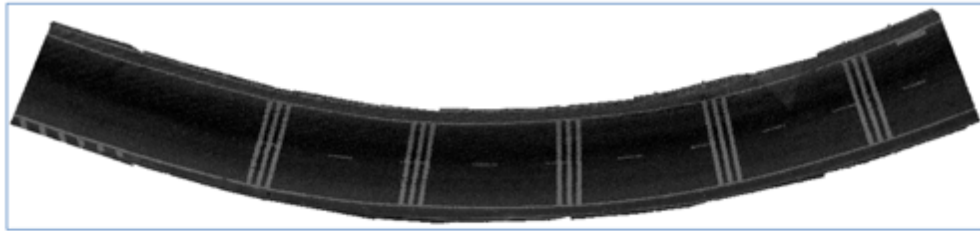


(d) result of the proposed method

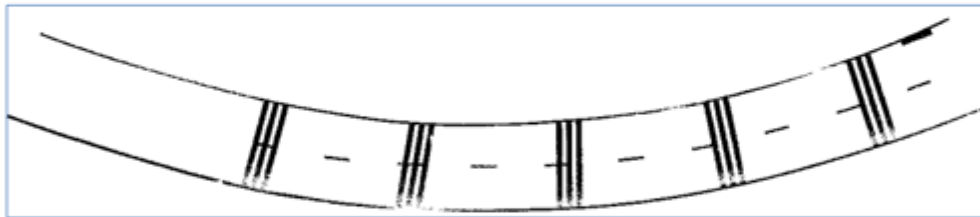


(e) the manually created reference data

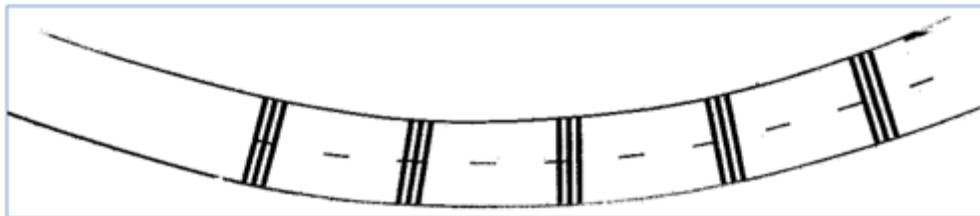
Figure 4.17 Road marking extraction results using Dataset IV: (a) raw pavement MLS points; (b) result of Chen's study; (c) result of Yu's study; (d) result of the proposed method; and (e) the manually labelled reference data.



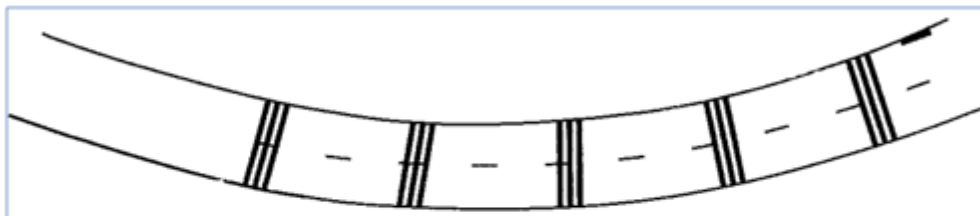
(a) raw point clouds



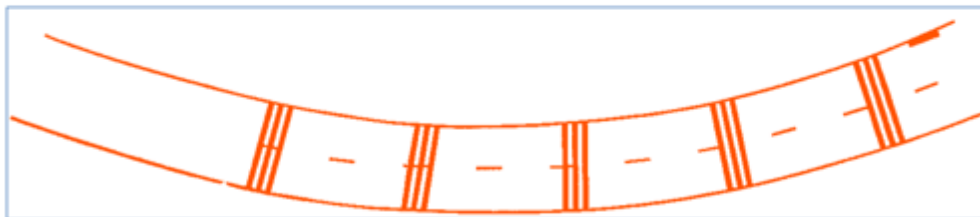
(b) result of Chen's method



(c) result of Yu's method



(d) result of the proposed method



(e) the manually created reference data

Figure 4.18 Road marking extraction results using Dataset V: (a) raw pavement MLS points; (b) result of Chen's study; (c) result of Yu's study; (d) result of the proposed method; and (e) the manually labelled reference data.

### 4.3.3 Accuracy Assessment of Driving Line Generation

The generated driving lines were overlapped with the orthoimagery in ArcGIS Desktop 10.2.2 to evaluate the performance of driving line generation algorithms using both visual inspection and quantitative assessment.

As illustrated in Table 4.15, the quantitative assessment was conducted based on recall and miscoding. Accordingly, four reference buffers with width of 5 cm, 10 cm, 15 cm, and 20 cm were established to evaluate the performance of proposed driving line generation algorithms. As a consequence, the proposed algorithms are capable of achieving an average of 72.90 % in recall within 5 cm-level reference buffer, 91.80% in recall within 10 cm-level reference buffer, and 100% in recall within 15 cm-level reference buffer for two generated driving lines. The values of miscoding decrease with the increased width of reference buffers, which demonstrates that the majority of generated driving lines are located within the precision allowable reference buffers. Experimentally, the proposed algorithms can provide a 15 cm-level localization accuracy in order to guarantee the quality requirements of 3D high-definition roadmaps and safety of autonomous driving.

Table 4.15 Accuracy assessment of driving line generation.

Driving lines Buffers	1		2	
	Recall (%)	Miscoding (%)	Recall (%)	Miscoding (%)
5 cm	74.82	24.48	70.98	28.23
10 cm	92.33	7.24	91.27	8.32
15 cm	100	0	100	0
20 cm	100	0	100	0

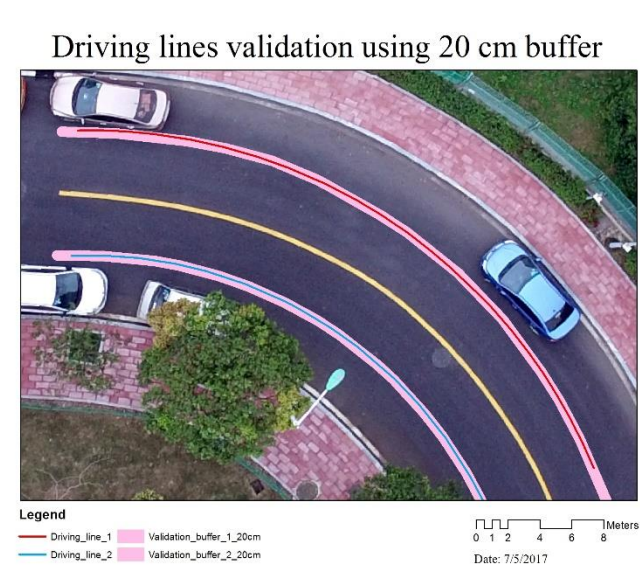
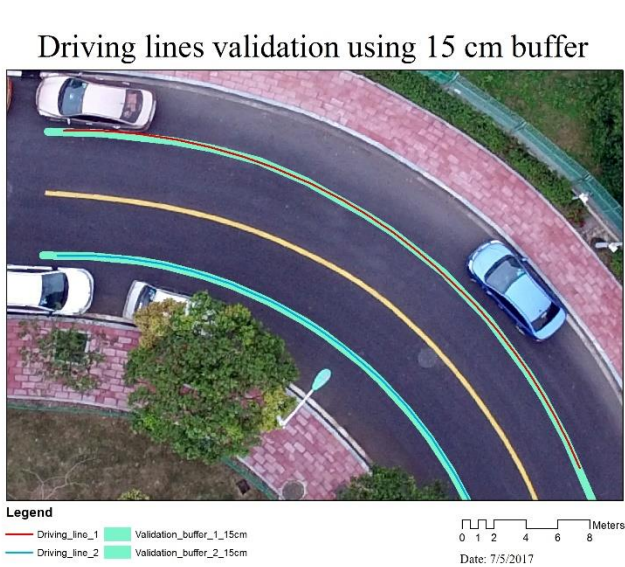
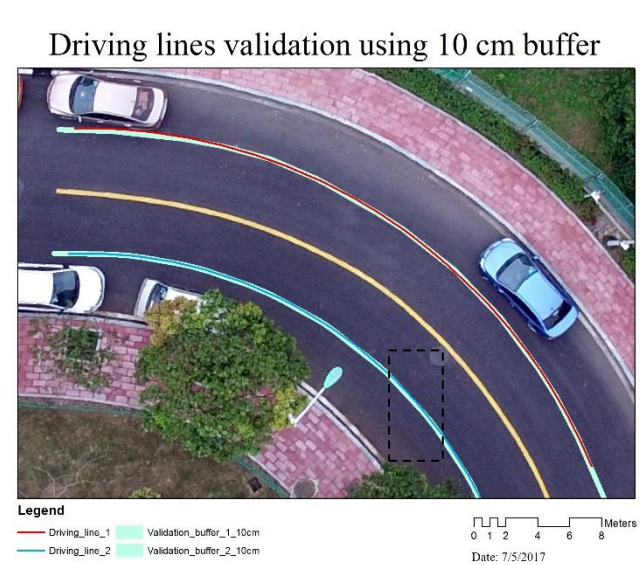
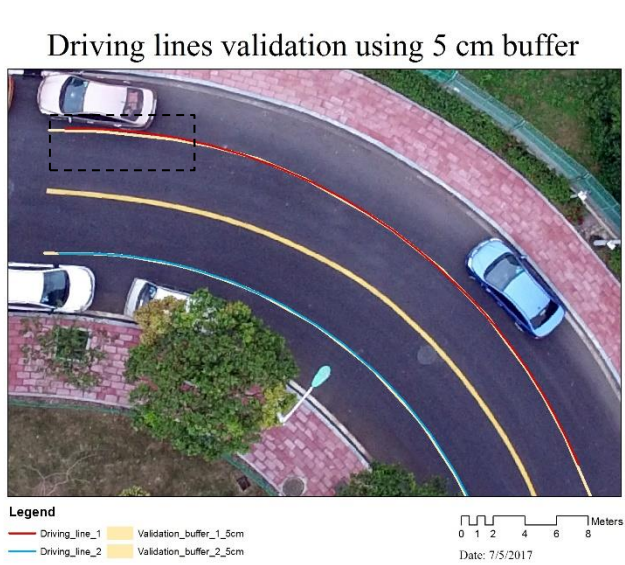


Figure 4.19 Driving line generation results within reference buffers.

As shown in Figure 4.19, the final results of generated driving lines are presented within 5 cm, 10 cm, 15 cm, and 20 cm width of reference buffers. It is identified that black rectangles in Figure 4.19 indicate miscoding parts while setting the width of reference buffers to be 5 cm and 10 cm. Moreover, it is worth noting that the generated driving lines are completely located within the reference buffers with width of 15 cm and 20 cm.

#### **4.4 Chapter Summary**

This chapter mainly presents the experimental results obtained using the proposed methods. According to the accuracy assessment and comparative study of road marking extraction, it indicates that the proposed road marking extraction algorithms can achieve high-quality results with 90.89% in recall, 93.04% in precision and 91.95% in F1-score, respectively. Moreover, based on the accuracy assessment of generated driving lines, it can be concluded that the proposed algorithms are capable of generating driving lines with 15 cm-level positioning accuracy at horizontally curved road sections. However, for those road surfaces with pavement dilapidation and curved road markings with disconnectivity, the proposed algorithms cannot generate driving lines successfully. Additionally, high curvature of a horizontal curve road section also accounts for a accuracy reduction on the final generation results.

Furthermore, a computational efficiency of all proposed algorithms has also been evaluated. It is worth noting that the proposed methods at the stage of driving line generation are highly effective and time-saving. Nevertheless, the overall performance should be further improved by optimizing algorithms of road surface extraction and road marking clustering.

## **Chapter 5 Conclusions and Recommendations**

### **5.1 Conclusions**

The autonomous vehicles have been developed and promoted by many worldwide automotive manufacturers and technology corporations, and fully-autonomous and self-contained vehicles are predicted to hit the automobile market within a decade. Additionally, it is still a thorny problem for autonomous vehicles to anticipate turns and intersections far beyond the reach of onboard sensors. Therefore, a 3D high-definition roadmap plays a conspicuous role to assist autonomous vehicles deal with complex road patterns and complicated traffic environments, particularly for horizontally curved road sections with ambiguous traffic conditions and limited sight distances for traffic participants. However, establishing a precise 3D high-definition roadmap with accurate road lane geometry and detailed road network information is still a considerable challenge. Currently, the advanced MLS technique advances the development of large-scale data acquisition with high-precision and time-saving measurements. With the assistance of digital cameras and a GNSS positioning subsystem, MLS systems can utilize active laser imaging technique to collect point clouds both day and night, and obtain georeferenced, high-density and accurate data effectively. Thus, these point clouds acquired by MLS systems can be applied to extract rich road characteristics and generate driving lines for highly autonomous driving at horizontally curved road sections.

However, disordered 3D laser points obtained by MLS systems are in large-volume and high-density with unevenly distributed intensity information, and these points do not have distinct topological relationships. Currently, there are few studies and relevant commercial software, which focus on driving line generation by using MLS data. Therefore, this thesis emphasizes the

significance and practical applicability to develop driving line generation algorithms for the research and development of 3D high-definition roadmaps and autonomous vehicles.

Accordingly, high-efficiency and reliable driving line generation algorithms from MLS data are thus developed. With the assistance of vehicle trajectory data, road surface points are extracted by first from raw MLS data to enhance computational efficiency using the curb-based extraction algorithms. Subsequently, curved road markings (e.g., centrelines, lane lines and edge lines) are extracted from the generated intensity imagery based on a multi-threshold extraction method, and discrete noises are filtered out using the SOR filter. Next, these extracted road markings are segmented into semantic clusters according to the conditional Euclidean clustering algorithm. Then, the nonlinear least-squares curve fitting algorithm is employed to determine the best-fitting mathematical functions of curved road markings. Finally, the candidate points of driving lines can be calculated based on both road design and construction standards and the generated best-fitting functions of curved road markings.

In this study, six datasets are used to evaluate the feasibility and validity of the proposed methods. Based on the quantitative assessment and comparative study, the proposed road marking extraction algorithms are capable of achieving 90.89% in recall, 93.04% in precision and 91.95% in F1-score, respectively. Moreover, with the assistance of high-resolution and UAV orthoimagery, it is indicated that the generated driving lines are completely located in the 15 cm-level reference buffers using ArcGIS Desktop 10.2.2. According to the experimental results, it demonstrates that the proposed algorithms can successfully and effectively generate driving lines at horizontally curved road sections from six MLS datasets with 15 cm localization accuracy. Therefore, the proposed driving line generation algorithms have capability to develop 3D high-definition roadmaps and autonomous vehicles. Additionally, these experimental results indicate



the proposed methods are not influenced by various curvatures of MLS test datasets. Nevertheless, for those roads with disconnectivity of curved road markings, the proposed methods cannot provide a valid solution to generate driving lines.

The overall performance indicates that majority of proposed algorithms in the process of driving line generation are highly efficient and time-saving. This thesis concludes that the proposed methodology is capable of efficient generation of the driving lines at horizontally curved road sections from MLS data to provide highly accurate localization services. It also provides a reliable solution to overcome the huge challenges for worldwide automotive manufacturers, technology corporations and mapping companies, including BMW, Tesla, Google, HERE and TomTom, who are committed to the generation of 3D high-definition roadmaps and promotion of autonomous vehicles.

## **5.2 Contributions**

The methodology proposed in this thesis contributes to the research and development of 3D high-definition roadmaps and autonomous vehicles. Generally, the main objectives presented in Chapter 1 have been fulfilled. The primary contributions of this study can be summarized in the following perspectives:

- A nonlinear least-squares curve fitting algorithm has been proposed using MLS data to generate the best-fitting functions of curved road markings. As mentioned in Chapter 3, determining the best-fitting functions of these curved road markings facilitates to generate the driving lines at horizontally curved road sections. Furthermore, these algorithms can be employed to effectively generate driving lines regardless of curvatures of different horizontally curved road sections.

- A semi-automatic driving line generation method at horizontal curves from MLS point clouds has been presented. Curved road markings are regarded as parallel curves in this study. According to road design regulations, the proposed algorithms improve accuracy by generating the driving lines directly from 3D point clouds. Moreover, it also guarantees highly computational performance to process large-volume MLS point clouds.

### **5.3 Limitations and Recommendations for Further Studies**

Based on the experimental results presented in Chapter 4, there are some limitations in the proposed algorithms. In order to overcome these challenges and enhance the efficiency and reliability of these proposed methods, several recommendations are therefore propounded. The details have been discussed as follows:

- The generation of geo-referenced intensity images have increased the contrast between road markings and pavements remarkably. However, complex road characteristics (e.g., road materials and roughness) with unevenly distributed point clouds have involved in huge influences on the efficiency and accuracy of the proposed method. Therefore, more research should focus on system calibration and data correction of MLS data for high-performance road marking extraction algorithms.
- In order to process large-volume MLS point clouds effectively, the overall performance of the proposed algorithms is need to be further improved. As described in Chapter 4, the road surface extraction and the SOR algorithms completely rely on the previous studies. However, these methods have been demonstrated to be time-consuming for the six test datasets. Thus, optimized algorithms of road surface extraction and noise removal deserve more research.

- The disconnectivity of curved road markings including road centrelines, edge lines and lane lines, has great influence on the completeness of the generated driving lines. Hence, more related studies should be involved in terms of computer vision, mathematical statistics, and data modelling to simulate and determine the broken parts of these road markings.
- Majority of test datasets used in this study are two-side and two-lane roads with fences on both sides. Therefore, the proposed algorithms are only proved to be effective and solid in specified road scenes with horizontal curves. Complex road sections comprising intersections, sharp corners, and multiple-lane roads should be further tested in order to enlarge the application range of the proposed algorithms.

## References

- Anderson, J. M., Nidhi, K., Stanley, K. D., Sorensen, P., Samaras, C., & Oluwatola, O. A., 2014. Autonomous vehicle technology: A guide for policymakers. Rand Corporation.
- Bauer, S., Alkhorshid, Y., & Wanielik, G., 2016. Using High-Definition maps for precise urban vehicle localization. *IEEE Intelligent Transportation Systems*, pp. 492-497.
- Boudette, N., 2017. Building a Road Map for the Self-Driving Car. The New York Times. Retrieved from: <https://www.nytimes.com/2017/03/02/automobiles/wheels/self-driving-cars-gps-maps.html>
- Boyko, A., & Funkhouser, T., 2011. Extracting roads from dense point clouds in large scale urban environment. *ISPRS Journal of Photogrammetry and Remote Sensing*, vol. 66, no. 6, S2-S12.
- Brenner, C., 2009. Extraction of features from mobile laser scanning data for future driver assistance systems. *Advances in GIScience*, pp. 25-42.
- Cabo, C., Cortés, S. G., & Ordoñez, C., 2015. Mobile laser scanner data for automatic surface detection based on line arrangement. *Automation in Construction*, 58, 28-37.
- Casner, S. M., Hutchins, E. L., & Norman, D., 2016. The challenges of partially automated driving. *Communications of the ACM*, vol. 59, no. 5, pp. 70-77.
- Charlton, S. G., 2007. The role of attention in horizontal curves: A comparison of advance warning, delineation, and road marking treatments. *Accident Analysis & Prevention*, vol. 39, no. 5, pp. 873-885.
- Chen, X., Kohlmeyer, B., Stroila, M., Alwar, N., Wang, R., & Bach, J., 2009. Next generation map making: geo-referenced ground-level LIDAR point clouds for automatic retro-reflective road feature extraction. *The Association for Computing Machinery*, pp. 488-491.
- Choi, J. W., Curry, R., & Elkaim, G., 2008. Path planning based on bézier curve for autonomous ground vehicles. *The World Congress on Engineering and Computer Science 2008, Advances in Electrical and Electronics Engineering-IAENG Special Edition*, pp. 158-166.
- Di Mascio, P., Di Vito, M., Loprencipe, G., & Ragnoli, A., 2012. Procedure to determine the geometry of road alignment using GPS data. *Procedia-Social and Behavioral Sciences*, vol. 53, pp. 1202-1215.

- Dokic, J., Müller, B., & Meyer, G., 2015. European roadmap smart systems for automated driving. *European Technology Platform on Smart Systems Integration*.
- Easa, S. M., Dong, H., & Li, J., 2007. Use of satellite imagery for establishing road horizontal alignments. *Journal of Surveying Engineering*, vol. 133, no. 1, pp. 29-35.
- Fagnant, D. J., & Kockelman, K., 2015. Preparing a nation for autonomous vehicles: opportunities, barriers and policy recommendations. *Transportation Research Part A: Policy and Practice*, vol. 77, pp. 167-181.
- Fahad, S., 2015. *The Roadmap for Autonomous (Self-Driving) Vehicles in Ontario, Canada*. White Paper of Ontario Good Roads Association. Ontario Good Roads Association.
- Gikas, V., & Stratakos, J., 2012. A novel geodetic engineering method for accurate and automated road/railway centerline geometry extraction based on the bearing diagram and fractal behavior. *IEEE Transactions on Intelligent Transportation Systems*, vol. 13, no. 1, pp. 115-126.
- Glennie, C., & Lichti, D. D., 2010. Static calibration and analysis of the Velodyne HDL-64E S2 for high accuracy mobile scanning. *Remote Sensing*, vol. 2, no. 6, pp. 1610-1624.
- Gräfe, G., 2008. Kinematic 3D laser scanning for road or railway construction surveys. *In Proceedings of the International Conference on Machine Control & Guidance*, pp. 24-26.
- Guan, H., 2013. *Automated Extraction of Road Information from Mobile Laser Scanning Data*. PhD Thesis. Department of Geography and Environmental Management, University of Waterloo.
- Guan, H., Li, J., Yu, Y., Wang, C., Chapman, M., & Yang, B., 2014. Using mobile laser scanning data for automated extraction of road markings. *ISPRS Journal of Photogrammetry and Remote Sensing*, vol. 87, pp. 93-107.
- Guan, H., Li, J., Yu, Y., Chapman, M., & Wang, C., 2015. Automated road information extraction from mobile laser scanning data. *IEEE Transactions on Intelligent Transportation Systems*, vol. 16, no. 1, pp. 194-205.
- Guerra, E., 2016. Planning for cars that drive themselves: Metropolitan Planning Organizations, regional transportation plans, and autonomous vehicles. *Journal of Planning Education and Research*, vol. 36, no. 2, pp. 210-224.
- Guizzo, E., 2011. How Google's self-driving car works. Retrieved from IEEE Spectrum Online

website: <http://www.123seminaronly.com/Seminar-Reports/2015-03/190666282-Google-Car>.

Guo, J., Tsai, M. J., & Han, J. Y., 2015. Automatic reconstruction of road surface features by using terrestrial mobile LiDAR. *Automation in Construction*, vol. 58, pp. 165-175.

Haala, N., Peter, M., Kremer, J., & Hunter, G., 2008. Mobile LiDAR mapping for 3D point cloud collection in urban areas—A performance test. *ISPRS Archives*, vol. 37, pp. 1119-1127.

HERE., 2016. HERE 360, Retrieved from: <http://360.here.com/2016/01/05/here-introduces-hd-live-map-to-show-the-path-to-highly-automated-driving/>.

Hervieu, A., & Soheilian, B., 2013. Semi-automatic road/pavement modeling using mobile laser scanning. *ISPRS Annals of the Photogrammetry, Remote Sensing and Spatial Information Sciences*, vol. 2.

Holgado-Barco, A., Gonzalez-Aguilera, D., Arias-Sanchez, P., & Martinez-Sanchez, J., 2014. An automated approach to vertical road characterisation using mobile LiDAR systems: Longitudinal profiles and cross-sections. *ISPRS Journal of Photogrammetry and Remote Sensing*, vol. 96, pp. 28-37.

Ibrahim, S., & Lichti, D., 2012. Curb-based street floor extraction from mobile terrestrial LiDAR point cloud. *ISPRS Archives*, vol. 5, pp. 39-45.

Jaakkola, A., Hyypä, J., Hyypä, H., & Kukko, A., 2008. Retrieval algorithms for road surface modelling using laser-based mobile mapping. *Sensors*, vol. 8, no. 9, pp. 5238-5249.

Karamanou, A., Papazissi, K., Paradissis, D., & Psarianos, B., 2009. Precise estimation of road horizontal and vertical geometric features using mobile mapping techniques. *Boletim de Ciências Geodésicas*, vol. 15, no. 5.

Khan, G., Bill, A., Chitturi, M., & Noyce, D., 2012. Horizontal curves, signs, and safety. *Transportation Research Record: Journal of the Transportation Research Board*, vol. 2279, pp. 124-131.

Kheyrollahi, A., & Breckon, T. P., 2012. Automatic real-time road marking recognition using a feature driven approach. *Machine Vision and Applications*, vol. 23, no. 1, pp. 123-133.

Kumar, P., McElhinney, C. P., Lewis, P., & McCarthy, T., 2014. Automated road markings extraction from mobile laser scanning data. *International Journal of Applied Earth Observation and Geoinformation*, vol. 32, pp. 125-137.

- Lakakis, K., Savvaiddis, P., & Wunderlich, T., 2013. Evaluation of a low-cost mobile mapping and inspection system for road safety classification. *American Journal of Geographic Information System*, vol. 2, no. 1, pp. 6-14.
- LAS Specification Version 1.4 – R13., 2011. The American Society for Photogrammetry & Remote Sensing, Retrieved from: <http://www.asprs.org>.
- Li, Z., Chitturi, M., Bill, A., & Noyce, D., 2012. Automated identification and extraction of horizontal curve information from geographic information system roadway maps. *Transportation Research Record: Journal of the Transportation Research Board*, vol. 2291, pp. 80-92.
- Litman, T., 2014. Autonomous vehicle implementation predictions. *Victoria Transport Policy Institute*, pp. 28-52.
- Lozano-Perez, T., 2012. *Autonomous robot vehicles*. Springer Science & Business Media.
- Manandhar, D., & Shibasaki, R., 2002. Auto-extraction of urban features from vehicle-borne laser data. *ISPRS Archives*, vol. 34, no. 4, pp. 650-655.
- Marquardt, D. W. (1963). An algorithm for least-squares estimation of nonlinear parameters. *Journal of the Society for Industrial and Applied Mathematics*, vol. 11, no. 2, pp. 431-441.
- Mathibela, B., Newman, P., & Posner, I., 2015. Reading the road: road marking classification and interpretation. *IEEE Transactions on Intelligent Transportation Systems*, vol. 16, no. 4, pp. 2072-2081.
- McCormac., C., Sarasua W., Davis W., 2012. *SURVEYING*, 6th Edition, John Wiley & Sons, Toronto, ISBN 978-0-470-49661-9, pp. 379.
- McDonald, N., 2004. Look and learn: capitalising on individual responsibility in speed management. In: *Proceedings of the 2004 Australian Institute of Traffic Planning and Management National Conference, Australian Institute of Traffic Planning and Management*, pp. 71–83.
- McElhinney, C. P., Kumar, P., Cahalane, C., & McCarthy, T., 2010. Initial results from European Road Safety Inspection (EURSI) mobile mapping project. In *ISPRS Commission V Technical Symposium*, pp. 440-445.
- Miller, G., 2014. Autonomous Cars Will Require a Totally New Kind of Map. WIRED, Retrieved from: <https://www.wired.com/2014/12/nokia-here-autonomous-car-maps>.
- Ogawa, T., & Takagi, K., 2006. Lane recognition using on-vehicle lidar. In *Intelligent Vehicles*

- Symposium*, pp. 540-545.
- Olsen, M. J., 2013. Guidelines for the use of mobile LIDAR in transportation applications. *Transportation Research Board*, vol. 748.
- Ontario Road Safety Annual Reports, 2016. *Preliminary 2016 Ontario Road Safety Annual Report Selected Statistics*. Retrieved from:  
<http://www.mto.gov.on.ca/english/publications/ontario-road-safety-annual-report.shtml>
- Otsu, N., 1979. A threshold selection method from grey-level histograms. *IEEE Transactions on Systems, Man, and Cybernetics*, vol. 9, no. 1, pp. 62-66.
- PCL, 2016. Conditional Euclidean Clustering. Retrieved from PCL: Retrieved from:  
[http://pointclouds.org/documentation/tutorials/conditional\\_euclidean\\_clustering.php#conditional-euclidean-clustering](http://pointclouds.org/documentation/tutorials/conditional_euclidean_clustering.php#conditional-euclidean-clustering)
- PCL, 2016. Removing Outliers Using a StatisticalOutlierRemoval Filter. Retrieved from:  
[http://pointclouds.org/documentation/tutorials/statistical\\_outlier.php#statistical-outlierremoval](http://pointclouds.org/documentation/tutorials/statistical_outlier.php#statistical-outlierremoval)
- Peden, M., 2004. *World Report on Road Traffic Injury Prevention*.
- PRC Minister of Construction, 2012. *Code for design of urban road engineering*, CJJ37-2012. China Architecture & Building Press.
- Pu, S., Rutzinger, M., Vosselman, G., & Elberink, S. O., 2011. Recognizing basic structures from mobile laser scanning data for road inventory studies. *ISPRS Journal of Photogrammetry and Remote Sensing*, vol. 66, no. 6, pp. 28-39.
- Puente, I., González-Jorge, H., Martínez-Sánchez, J., & Arias, P., 2013. Review of mobile mapping and surveying technologies. *Measurement*, vol. 46, no. 7, pp. 2127-2145.
- Pukelsheim, F., 1994. The three sigma rule. *The American Statistician*, vol. 48, no. 2, pp. 88-91.
- RIEGL., 2017. RIEGL VQ-450, Retrieved from:  
<http://www.riegl.com/nc/products/mobile-scanning/produktdetail/product/scanner/31>.
- Riveiro, B., González-Jorge, H., Martínez-Sánchez, J., Díaz-Vilariño, L., & Arias, P., 2015. Automatic detection of zebra crossings from mobile LiDAR data. *Optics & Laser Technology*, vol. 70, 63-70.
- Rusu, R. B., & Cousins, S., 2011. 3D is here: Point cloud library (PCL). *2011 IEEE International Conference on Robotics and Automation*, pp. 1-4.
- Schwarz, B., 2010. LIDAR: Mapping the world in 3D. *Nature Photonics*, vol. 4, no. 7, pp. 429-



430.

Seif, H. G., & Hu, X., 2016. Autonomous Driving in the iCity—HD Maps as a Key Challenge of the Automotive Industry. *Engineering*, vol. 2, no. 2, pp. 159-162.

Shaker, A., Yan, W. Y., & Easa, S., 2010. Using stereo satellite imagery for topographic and transportation applications: An accuracy assessment. *GIScience & Remote Sensing*, vol. 47, no. 3, pp. 321-337.

Sisson, P., 2017. Driverless cars: Who's doing what, and how it impacts urban transportation. Retrieved from: <https://www.curbed.com/2017/7/7/15935126/google-uber-driverless-car-waymo-autonomous>.

Smadja, L., Ninot, J., & Gavrilovic, T., 2010. Road extraction and environment interpretation from LiDAR sensors. *ISPRS Archives*, vol. 38, pp. 281-286.

The United States Department of Transportation, 2004. *Enhanced Digital Mapping Project Final Report*. Retrieved from: [https://ntl.bts.gov/lib/jpodocs/repts\\_te/14161.html](https://ntl.bts.gov/lib/jpodocs/repts_te/14161.html).

Torbic, D. J., Harwood, D. W., Gilmore, D. K., Pfefer, R., Neuman, T. R., Slack, K. L., & Hardy, K. K., 2004. A guide for reducing collisions on horizontal curves. *National Cooperative Highway Research Program Report*, vol. 500, no. 7.

Toth, C. K., 2009. R&D of mobile LIDAR mapping and future trends. *In Proceeding of ASPRS 2009 Annual Conference*, pp. 23-45.

Urmson, C., 2008. Self-driving cars and the urban challenge. *IEEE Intelligent Systems*, vol. 23, no. 2.

Veit, T., Tarel, J. P., Nicolle, P., & Charbonnier, P., 2008. Evaluation of road marking feature extraction. *The IEEE Intelligent Transportation Systems Conference 2008*, pp. 174-181.

Vosselman, G., 2009. Advanced point cloud processing. *In Photogrammetric Week*. Vol. 9, pp. 137-146.

Vosselman, G., & Maas, H. G., 2010. *Airborne and Terrestrial Laser Scanning*. Whittles Publishing.

Wang, H., Cai, Z., Luo, H., Wang, C., Li, P., Yang, W., & Li, J., 2012. Automatic road extraction from mobile laser scanning data. *2012 IEEE International Conference on Computer Vision in Remote Sensing*, pp. 136-139.

Wang, H., Luo, H., Wen, C., Cheng, J., Li, P., Chen, Y., & Li, J., 2015. Road boundaries

- detection based on local normal saliency from mobile laser scanning data. *IEEE Geoscience and Remote Sensing Letters*, vol. 12, no. 10, pp. 2085-2089.
- Yang, B., Fang, L., Li, Q., & Li, J., 2012. Automated extraction of road markings from mobile LiDAR point clouds. *Photogrammetric Engineering & Remote Sensing*, vol. 78, no. 4, pp. 331-338.
- Yang, B., Fang, L., & Li, J., 2013. Semi-automated extraction and delineation of 3D roads of street scene from mobile laser scanning point clouds. *ISPRS Journal of Photogrammetry and Remote Sensing*, vol. 79, pp. 80-93.
- Yang, B., Dong, Z., Liu, Y., Liang, F., & Wang, Y., 2017. Computing multiple aggregation levels and contextual features for road facilities recognition using mobile laser scanning data. *ISPRS Journal of Photogrammetry and Remote Sensing*, vol. 126, pp. 180-194.
- Yoon, J., & Crane, C. D., 2009. Evaluation of terrain using LADAR data in urban environment for autonomous vehicles and its application in the DARPA urban challenge. *ICROS & SICE International Joint Conference*, pp. 641-646.
- Yu, S. J., Sukumar, S. R., Koschan, A. F., Page, D. L., & Abidi, M. A., 2007. 3D reconstruction of road surfaces using an integrated multi-sensory approach. *Optics and lasers in engineering*, vol. 45, no. 7, pp. 808-818.
- Yu, Y., Li, J., Guan, H., Jia, F., & Wang, C., 2015. Learning hierarchical features for automated extraction of road markings from 3-D mobile LiDAR point clouds. *IEEE Journal of Selected Topics in Applied Earth Observations and Remote Sensing*, vol. 8, no. 2, pp. 709-726.
- Yuan, X., Zhao, C. X., & Zhang, H. F., 2010. Road detection and corner extraction using high definition Lidar. *Information Technology Journal*, vol. 9, no. 5, pp. 1022-1030.
- Zhao, H., & Shibasaki, R., 2003. Reconstructing a textured CAD model of an urban environment using vehicle-borne laser range scanners and line cameras. *Machine Vision and Applications*, vol. 14, no. 1, pp. 35-41.
- Zhang, H., 2016. *Rapid Inspection of Pavement Markings Using Mobile Laser Scanning Point Clouds*. MSc Thesis, Department of Geography and Environmental Management, University of Waterloo.